LASER MICRO/NANO MACHINING BASED ON SPATIAL, TEMPORAL AND SPECTRAL CONTROL OF LIGHT-MATTER INTERACTION

by

XIAOMING YU

B.S., Nankai University, 2008
M.S., Shanghai Institute of Optics and Fine Mechanics, 2012

AN ABSTRACT OF A DISSERTATION

submitted in partial fulfillment of the requirements for the degree

DOCTOR OF PHILOSOPHY

Department of Industrial and Manufacturing Systems Engineering
College of Engineering

KANSAS STATE UNIVERSITY
Manhattan, Kansas

2016

Abstract

Lasers have been widely used as a manufacturing tool for material processing, such as drilling, cutting, welding and surface texturing. Compared to traditional manufacturing methods, laser-based material processing is high precision, can treat a wide range of materials, and has no tool wear. However, demanding manufacturing processes emerging from the needs of nano and 3D fabrication require the development of laser processing strategies that can address critical issues such as machining resolution, processing speed and product quality. This dissertation concerns the development of novel laser processing strategies based on spatial, temporal and spectral control of light-matter interaction.

In the spatial domain, beam shaping is employed in ultrafast laser micro-processing. Zero-order Bessel beam, generated by an axicon, is used for selective removal of the back contact layer of thin film solar cells. Bessel beam's propagation-invariance property gives rise to an extension of focal range by orders of magnitude compared to Gaussian beam, greatly increasing process tolerance to surface unevenness and positioning error. Together with the axicon, a spatial light modulator is subsequently used to modify the phase of laser beam and generate superpositions of high-order Bessel beam with high energy efficiency. With the superposed beam, processing speed can be increased significantly, and collateral damage resulting from the ring structures in the zero-order Bessel beam can be greatly suppressed.

In the temporal domain, it is demonstrated that ionization in dielectric materials can be controlled with a pair of ultraviolet and infrared pulses. With the assistance of the long-wavelength infrared pulse, nano-scale features are achieved using only a small fraction of threshold energy for the short-wavelength pulse. Computer simulation based on the rate equation model is conducted and found to be in good agreement with experimental results. This study paves the way for future

adoption of short-wavelength laser sources, for example in the extreme ultraviolet range, for direct laser nano-fabrication with below-threshold pulse energy.

In the spectral domain, a short-wavelength infrared laser is used to generate modification in the bulk of silicon wafers, in an attempt to develop 3D fabrication capabilities in semiconductors. Issues such as spherical aberration correction and examination procedure are addressed. Permanent modification is generated inside silicon by tightly focusing and continuously scanning the laser beam inside the samples, without introducing surface damage. The effect of laser pulse energy and polarization is also investigated.

These results demonstrate the potential of controlling laser processing in multiple dimensions for manufacturing purposes, and point to a future when laser can be used as naturally and efficiently as mechanical tools used today, but is targeted at more challenging problems.

LASER MICRO/NANO MACHINING BASED ON SPATIAL, TEMPORAL AND SPECTRAL CONTROL OF LIGHT-MATTER INTERACTION

by

XIAOMING YU

B.S., Nankai University, 2008
M.S., Shanghai Institute of Optics and Fine Mechanics, 2012

A DISSERTATION

submitted in partial fulfillment of the requirements for the degree

DOCTOR OF PHILOSOPHY

Department of Industrial and Manufacturing Systems Engineering
College of Engineering

KANSAS STATE UNIVERSITY
Manhattan, Kansas

2016

Approved by:

Major Professor
Dr. Shuting Lei

Copyright

Abstract

Lasers have been widely used as a manufacturing tool for material processing, such as drilling, cutting, welding and surface texturing. Compared to traditional manufacturing methods, laser-based material processing is high precision, can treat a wide range of materials, and has no tool wear. However, demanding manufacturing processes emerging from the needs of nano and 3D fabrication require the development of laser processing strategies that can address critical issues such as machining resolution, processing speed and product quality. This dissertation concerns the development of novel laser processing strategies based on spatial, temporal and spectral control of light-matter interaction.

In the spatial domain, beam shaping is employed in ultrafast laser micro-processing. Zero-order Bessel beam, generated by an axicon, is used for selective removal of the back contact layer of thin film solar cells. Bessel beam's propagation-invariance property gives rise to an extension of focal range by orders of magnitude compared to Gaussian beam, greatly increasing process tolerance to surface unevenness and positioning error. Together with the axicon, a spatial light modulator is subsequently used to modify the phase of laser beam and generate superpositions of high-order Bessel beam with high energy efficiency. With the superposed beam, processing speed can be increased significantly, and collateral damage resulting from the ring structures in the zero-order Bessel beam can be greatly suppressed.

In the temporal domain, it is demonstrated that ionization in dielectric materials can be controlled with a pair of ultraviolet and infrared pulses. With the assistance of the long-wavelength infrared pulse, nano-scale features are achieved using only a small fraction of threshold energy for the short-wavelength pulse. Computer simulation based on the rate equation model is conducted and found to be in good agreement with experimental results. This study paves the way for future

adoption of short-wavelength laser sources, for example in the extreme ultraviolet range, for direct laser nano-fabrication with below-threshold pulse energy.

In the spectral domain, a short-wavelength infrared laser is used to generate modification in the bulk of silicon wafers, in an attempt to develop 3D fabrication capabilities in semiconductors. Issues such as spherical aberration correction and examination procedure are addressed. Permanent modification is generated inside silicon by tightly focusing and continuously scanning the laser beam inside the samples, without introducing surface damage. The effect of laser pulse energy and polarization is also investigated.

These results demonstrate the potential of controlling laser processing in multiple dimensions for manufacturing purposes, and point to a future when laser can be used as naturally and efficiently as mechanical tools used today, but is targeted at more challenging problems.

Table of Contents

List of Figures

List of Tables

Acknowledgements

Doing research is about objectivity. We look at facts and evidence, and try to avoid personal emotions and feelings when we are working. Nevertheless, it is the people we are working with that influence and inspire us about how we do research, how we see the world, and what to pursue for life. Reflecting on my life up to now, I feel that I am deeply in debt to all the people who have given me guidance, encouraged me to do my best, and helped me overcome my weaknesses. Over the years of PhD study, I feel very fortunate in that I have met so many great people, without whom it would be impossible to finish any part of dissertation.

I would like to give my sincere gratitude to my advisor, Dr. Shuting Lei. He is a person of integrity, wisdom and persistence. Learning these from him, even a little bit, would be invaluable asset for my life. I thank him for guiding my research and encouraging me to pursue my own interests. It suffices to say that being his student has changed my whole life.

I would also like to thank Dr. Zenghu Chang, whose scientific rigor and relentless pursuit of new knowledge inspired me to become a researcher. I especially thank him for scheduling weekly discussion with me, during which he helped me sort out problems and trained me how to do so on my own.

I am also indebted to my supervisory committee, Dr. John Wu, Dr. Shing I. Chang, Dr. Gurpreet Singh, Dr. Daniel Higgins and Dr. Zenghu Chang. All of them gave me advice on my research and helped me revise the dissertation. Special thanks to Dr. Higgins, for his assistance in AFM imaging. I thank the department head, Dr. Bradley Kramer, for overseeing the PhD program, and thank the IMSE department as a whole for providing me support. I also thank all the faculty in the department, especially Dr. Meng Zhang, Dr. Dong Lin and Dr. ZJ Pei for their helpful advice.

Majority of the research was conducted in the James R. MacDonald Laboratory, Department of Physics at KSU. I would like to thank all the professors and staff who gave me selfless assistance with my research and took the responsibility of maintaining the equipment. Among them are Dr. Itzik Ben-Itzhak, Dr. Lew Cocke, Dr. Vinod Kumarappan, Dr. Charles Fehrenbach, Al Rankin, Mike Well, Vince Needham and others. I especially thank Dr. Carlos Trallero, for sharing his brilliant ideas and revising paper manuscripts.

I would also like to thank all of the collaborators from KSU and other institutes: Dr. Paul Corkum from University of Ottawa/National Research Council of Canada, Dr. David Grojo from LP3 CNRS/Aix-Marseille University, Dr. Jeff Ma from Saint Louis University, Dr. Jun Li from the Department of Chemistry, and Dr. Jianxin Deng from Shandong University.

This dissertation would be impossible to finish without assistance from postdocs and fellow students from and outside of our group. I would like to thank Dr. Baozhen Zhao, Dr. Qiumei Bian, Dr. Xiaoming Ren, Dr. Sabih Khan, Dr. Wei Cao, Dr. Guillaume Laurent, Dr. Rajesh Kumar Kushawaha, Dr. Xiaoxu Song, Xinya Wang, Adam Summers, Jan Tross, Aram Vajdi, Derrek Wilson, Pratap Timilsina, Stefan Zigo, Kedong Zhang, Dr. Yunsong Lian, Dr. Yan Cheng, Huynh Lam, Hao Xu, Yiqun Yang and Margaux Chanal.

I thank Vicky Geyer, Doris Galvan, Myra Peoples and other administrators for their endless help.

Finally, I thank my parents, my wife and my friends for their support and encouragement.

Chapter 1 - Introduction

1. Background

Manufacturing is about making stuff, and the progress of our society relies on how good we are at it. For millennia we have evolved from polishing a stone to building a spacecraft that travels beyond the solar system. Essential to manufacturing is the variety of tools we use, each of which is designed and optimized for a specific purpose. For example, the shape and material of a drill bit is chosen according to the processing type (e.g., indenting, trepannig, enlarging) and target material (e.g., metal, wood, glass).

Lasers are a new type of manufacturing tool, and have already been widely used for material processing, such as drilling, cutting, welding and surface texturing. Compared to traditional manufacturing methods, laser-based material processing is high precision, can treat a wide range of materials, and has no tool wear.

The first laser processing test was reported in 1967 [1], merely 7 years after the first laser was put into operation. From a physical point of view, laser processing represents a new type of material processing: fermion-fermion contact between a mechanical tool and target material is replaced by boson-fermion interaction. This difference is illustrated in Figure 1.1, where mechanical drilling is compared with laser drilling. Both the mechanical tool and target material are represented as clusters of atoms. It is readily seen that there are several issues associated with mechanical processing. First, pressure generated in the interaction region can deform the lattice structure, leaving residual stress that needs to be removed by post-processing. Second, material can transfer between the tool and the target, resulting in tool wear and debris. These drawbacks can be avoided using laser processing, where material removal is achieved by ejecting energized atoms directly into environment, resulting in improved precision and intact lattice structure.

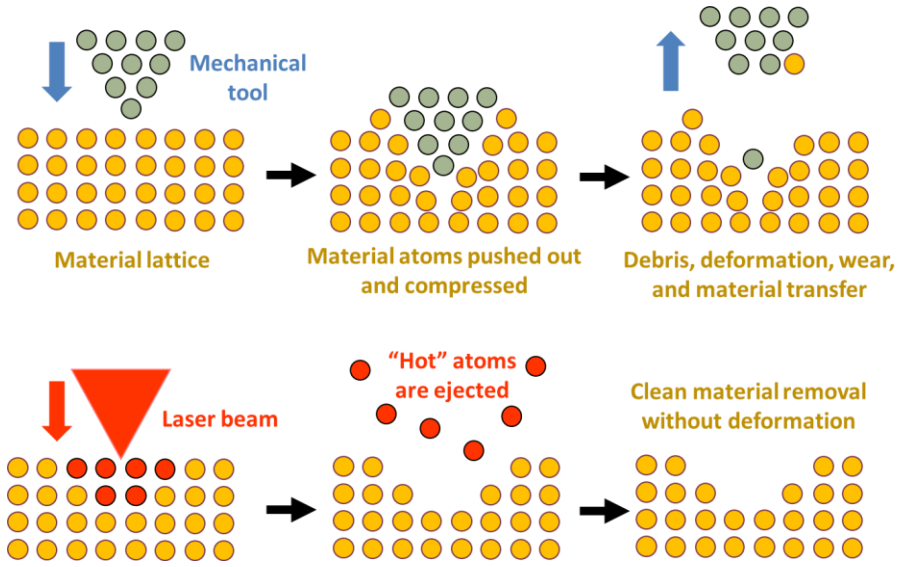

Figure 1.1 A comparison illustrating the key differences between mechanical and laser processing.

Not every type of laser is suitable for high-precision machining, largely due to the enormous amount of heat generated during laser-material interaction. The heat propagates beyond the laser focal region, reduces machining resolution, and generates collateral thermal damage. One way to suppress this thermal effect is using ultrafast lasers with pulse duration in the femtosecond (fs) and picosecond (ps) region (1 fs = 1×10^{-15} s, 1 ps = 1×10^{-12} s). For these lasers, the pulse duration is so short that during energy deposition heat is contained only in the focal volume. Therefore, fine structures on the micro- and nano-meter scale can be achieved with relative ease.

In addition, the intensity of focused femtosecond laser pulses is strong enough to trigger nonlinear absorption processes in wide-bandgap materials, which are otherwise transparent in the linear absorption region. When focused inside transparent materials, such laser pulses generate localized plasma at the focal volume, resulting in structural modification inside materials without damaging material surface. This three-dimensional (3D) machining capability makes femtosecond laser a powerful tool for direct fabrication of 3D photonic and microfluidic structures [2].

Despite their promising potential and growing popularity in research labs, ultrafast lasers have not been adopted as a manufacturing workhorse. Several reasons contribute to this issue. An apparent one is cost. The price of a commercial solid state ultrafast laser system can range from several hundred thousand to several million dollars. However, this is a minor issue because the investment for an ultrafast laser can be justified by looking at the dramatic improvement in product quality and hence increase in revenue. Maintenance might be another concern. The complexity of ultrafast lasers requires regular tune-up, typically on a daily basis. This is also a minor issue, because the stability continues to increase, and compact, single-stage, hands-free laser systems targeted at industrial use have been commercially available.

The main reason that ultrafast lasers are not widely accepted as an essential manufacturing tool is, in the author's opinion, the lack of fundamental understanding of laser-matter interaction under ultrafast timescale and ultrasmall spatial scale. This is an ever-expanding frontier, with many possibilities waiting to be explored. For example, the emerging fields of nano and 3D manufacturing call for the development of new manufacturing tools, and the adoption of lasers as such tools depends on a fundamental understanding of the underlying physical processes in this regime.

2. Research objective

This dissertation tries to answer (only to a limited extent) this question: How do we use laser to its fullest potential as a manufacturing tool? This question is approached from various angles: (1) In the spatial domain, a study on Bessel beam micromachining is aimed at solving the problem of inconsistent processing quality due to inaccurate positioning of laser focus. In a later study, superpositions of high order Bessel beams are generated and applied in material processing, demonstrating the advantages of designing various types of propagation-invariant laser fields. (2)

In the temporal domain, to improve machining resolution and reduce ultraviolet pulse energy, a scheme of two-color ultrafast laser processing is developed. This study paves the way for future adoption of short-wavelength laser sources, such as in the extreme ultraviolet range, for direct nano-fabrication with below-threshold pulse energy. (3) In the spectral domain, as a first step towards 3D fabrication in semiconductors, short-wavelength infrared laser is used to generate modification in the bulk of silicon wafers.

It is in the author's best hope that this dissertation can demonstrate the great potential of controlling laser processing in multiple dimensions for manufacturing purposes, and point to a future when laser can be used as naturally and efficiently as mechanical tools used today, but for more challenging problems.

3. Literature review

3.1 Material processing with Bessel beam

Mentioned in the beginning of the dissertation, the design of various types of drill bits is a perfect example of how tool geometry influences material processing. Spatial beam shaping is the counterpart of tool design in laser material processing, and has already been adopted for industrial use.

Laser beam shaping is the redistribution of irradiance and phase of a laser beam [3]. By this definition, focusing laser with a simple convex lens can be considered as shaping. And indeed, "passive optics", like circular and cylindrical lenses, are among the most commonly used elements. Diffractive optical elements (DOE) are still considered as passive optics, even though complex wavefront can be generated. "Active optics", on the other hand, provide more flexibility in beam design and can be programmed to change beam shape in time. Among those new optics, spatial light modulators (SLM) are increasingly adopted in research labs. Part of this dissertation focuses

on the design and application of a particular type of laser beam shape - Bessel beam. SLM is used in this research to generate nonzero-order Bessel beam.

Bessel beam is a type of propagation-invariant laser field, which maintains its spatial profile along the propagation direction. Bessel beam is often referred to as “diffraction-free” or “non-diffracting” beam. The reader is referred to Turunen and Friberg [4] for a comprehensive review on propagation-invariant field and Bessel beam. In the following paragraphs, previous work related to this dissertation is reviewed, with emphasis on material processing with Bessel beam.

While the concept of propagation-invariant field and early realization of Bessel beam can be traced back to 1940-1960 [4], the use of Bessel beams for material processing was first reported in 2001, when Marcinkevičius *et al*. [5] use Bessel beam to generate long tracks of damage inside glass without the need to translate the sample along the beam propagation direction, as would be required for Gaussian beams. Kohno and Matsuoka [6] use Bessel beam to process silicon and stainless steel foil, and demonstrate that the diameter of drilled holes is not sensitive to work distance, due to the long focal range of Bessel beam. Courvoisier *et al*. [7] use Bessel beam to generate nano-scale feature. Later Bhuyan *et al*. apply a similar approach and are able to directly generate high-aspect-ratio, nano-scale channels in glass [8]. High-order Bessel beams have also been used in material processing. Arnold *et al*. [9,10] generate an 8-th order Bessel vortex beam by encoding phase mask on a spatial light modulator. By focusing this beam inside BK-7 glass, they generate 3D cylindrical structure with single pulse exposure. Xie *et al*. [11] investigate the propagation property for high power vortex beam, and fabricate 3D structure with a 3th-order beam. Grojo *et al*. [12] study the energy deposition of Bessel beam inside silicon, concluding that

intensity clamping due to strong nonlinear effects imposes a limit on how much energy can be deposited.

3.2 Femtosecond laser machining at the nanometer scale

The ability of femtosecond lasers in fabricating nanometer-scale features has been demonstrated in 1995 [13] shortly after the first investigation of ultrafast laser breakdown of condensed matter [14]. As mentioned in the previous section, the minimal thermal effect in femtosecond laser ablation ensures that damage occurs in a confined volume determined by the focal spot size. Due to the existence of multiphoton absorption and damage threshold in wide bandgap materials, sub-micrometer damage can be achieved by lowering laser fluence so that only the tip of the focus exceeds the damage threshold. With this approach, 40 nm-diameter holes have been fabricated on glass [15]. This method, however, heavily relies upon the precise control of laser fluence, and small energy fluctuation can lead to repeatability issues, and therefore is not feasible for industrial application.

As an alternative method, reducing focal spot size to nanometer scale will inherently result in nano-scale feature. Diffraction imposes a limit to the smallest focal spot size, which is on the order of λ/NA, where λ is the laser wavelength and NA is the numerical aperture of focusing optics. By using high NA microscope objectives, researchers have achieved structures with the size of ~130 nm on fused silica and 200 nm on PMMA [16,17], and nano-voids inside dielectrics [18]. The use of high NA optics has two major drawbacks. First, non-oil immersion objectives have an NA smaller than unity. Second, high NA objectives have small working distance, which is not favored in machining application because ablated material can deposit on the objective surface and affect beam delivery and even damage focusing optics. The other direction is to reduce laser

wavelength. Feature size of 80-600 nm has been achieved with X-ray and ultraviolet lasers [19-23].

The above-mentioned techniques focus on generating nano-scale features with single pulse irradiation. Nanostructures can also be achieved with repeated pulse irradiation, such as laser induced periodic surface structures (LIPSS) [24,25], nano-grating inside glass [26,27], and spikes on silicon [28]. Besides, taking advantages of chemical reaction such as photopolymerization in organic materials, researchers are able to achieve 40 nm feature size by combining activating and deactivating beams simultaneously [29-32].

3.3 Temporally-controlled double-/multi-pulse processing

Another aspect of this research is the temporal control of carrier dynamics with double pulse experiments. In this section research of double-/multi-pulse material processing is reviewed, with focus on enhanced ablation, reduced damage threshold, and damage shape modification.

Choi *et al*. observe an increase in ablation volume with two pulses at ~10 ps delay compared to the sum of ablation volume with individual beams [33]. This increase is attributed to a better energy coupling to the sample (crystalline silicon) with delayed pulses. It is suggested that, when the delay is shorter (1-5 ps), the reflection loss for the second pulse is higher due to the liquid film or hot surface plasma formed by the first pulse. At longer delays, the transmission is lower due to the ejected material. Chowdhury *et al*. perform a similar experiment on fused silica samples. In contrast to Choi *et al*.'s results with silicon, it is shown that ablation enhancement occurs when the two pulses overlap at zero delay, and that enhancement decreases rapidly after 1-ps delay [34]. This rapid decrease is attributed to the fact that plasma generated by the first pulse acts as a shield and reduces energy absorption of the material from the second pulse. Singha *et al*. perform double-pulse fluorescence measurements with silicon, copper and CaF_2, and observe a phase transition

from solid to liquid in a few ps [35]. They also observe that ablation volume of single pulses is similar to that of double pulses with delays ranging from 0 to 105 ps with the same total energy, which is similar to simulation and experimental results reported by other groups [36,37]. Recent results show that different morphologies are obtained with double pulses with 0.2 and 106 ps delays on silicon, and it is suggested that long delay (106 ps) results in better energy coupling [38].

Another aspect in double pulse machining is the reduction of damage threshold. Li *et al*. perform an experiment using two 25-fs, 800-nm pulses on fused silica and barium aluminum borosilicate (BBS), and observe a decrease of damage thresholds for both materials [39]. The explanation of the threshold decrease is that the first pulse provides "seeding" electrons which absorb energy from the second pulse by the avalanche process. They also observe a fast decay (200 fs) of free electron population, and therefore a decay term is added into the rate equation model. However, the origin of this term is unclear at that time. Later Petite *et al*. argue that this term may come from self-trapped excitons (STEs) [40]. A similar trapping time of 150 fs is observed. Reduction in damage thresholds is also observed with 10-ps 1064-nm lasers in Si samples [41]. A recent study shows that with the combination of XUV and IR pulse, damage can occur even if the fluences of the two pulses are well below damage thresholds in PMMA [42].

Other machining experiments involving the use of double pulses include: multi-wavelength [41,43-45], temporal shaping [46], and superposition of femtosecond and nanosecond lasers [47,48]. The purpose of these studies is to enhance ablation. For example, Lin *et al*. perform an experiment using the superposition of femtosecond and nanosecond laser pulses [47]. Ablation enhancement up to 13.4 times in ablation depth and 50.7 times in material removal volume is observed on fused silica. This enhancement is attributed to material transition to a metallic state after the femtosecond pulse. This metallic state enhances energy absorption from the nanosecond

pulse. Aside from machining purposes, this double pulse technique has also been used in the study of plasma shielding, generation of electromagnetic pulses, optical welding, control of surface ripples and plasma plume emission, etc [49-53]. Recent experiments with double pulses have shown increased aspect ratios and improved quality in drilling micro-channels in PMMA [54].

An extension to the above-mentioned double-pulse technique is the use of temporally modified pulse trains, which can be achieved by temporal beam shaping devices such as spatial light modulators (SLM) [55]. Such pulse trains have been used to modify damage shapes [56,57], improve damage quality [46], and achieve nano-scale features [58-61].

Even with single pulses, control of carrier dynamics is also possible by introducing time-dependent frequency (chirp) into the pulse. The idea is based on the fact that electrons have different response (such as ionization rates) to different frequency components in a chirped pulse. Reduction in damage threshold has been shown with this method [62-66].

3.4 3D manufacturing in the bulk of semiconductor

The ability to directly generate three-dimensional (3D) structures inside materials distinguishes laser-based materials processing from other planar lithographic methods, and has been extensively studied for large-bandgap materials [2]. Potential applications with this 3D technique include the fabrication of optical waveguides [67], microfluidic network [68,69], electronic circuits [70], etc., and the integration of these components to realize lab-on-a-chip [71]. Fabrication in 3D is realized by concentrating large amount of laser energy within a small volume inside materials, and is usually initiated through nonlinear processes such as multiphoton and avalanche ionization [72,73]. Due to their large bandgaps, dielectric materials can be processed with laser wavelengths as short as in the ultraviolet range [74]. Formation of voids [75] and nano-channels [76] inside dielectrics has been reported.

Semiconductors (such as silicon) form the basis of modern electronics. Current manufacturing processes, notably photolithography, are inherently planar methods, and 3D structures are achieved in a layer-by-layer fashion, which involves multiple steps and therefore increases defect rate and reduces yield. Laser-based 3D fabrication provides a one-step manufacturing solution and has the potential to reduce processing time and cost. The reader can refer to Ref. [77] for a short review on internal modification of silicon. Early work includes writing waveguide below an oxide layer in silicon [78]. Recent advances include internal modification for wafer dicing [77], double-femtosecond-laser-pulse induced modification [79], machining on the back surface of silicon [80], and attempt to fabricate micro-channels inside silicon [12].

4. Interrelationship between spatial, temporal and spectral aspects

While presented separately in this dissertation, the three aspects of controlling laser material processing are interrelated. After all, laser impinging on material is a single event, which requires careful control of the various aspects in relation to each other.

The spatial and temporal domains are closely related. For example, hot electrons generated in a small volume by a tightly focused laser beam will naturally diffuse in time to the surrounding area. This effect may lead to reduced processing resolution. Another example is pulsed Bessel beam, which shows a pulse duration-dependent spatial profile [81], and has been discussed in recent publications [82,83].

The time-bandwidth product, on the other hand, imposes a fundamental limit on the control precision between the temporal and spectral domain. To obtain better temporal control of electron dynamics, one tends to use shorter laser pulses. As a trade-off, the spectral control precision is decreased, due to increased spectral width. A balance is required when designing laser processing methods when both temporal and spectral precision is desired.

5. Outline of this dissertation

Chapter 1 constitutes background information, the research objective, a literature review of the topics closely related to the current work, and a short section discussing the interrelationship between three aspects covered in the dissertation.

Chapters 2 and 3 present the work on femtosecond Bessel beam micromachining.

Chapters 4 to 6 present the work on femtosecond double-pulse micro- and nano-machining.

Chapter 7 presents the work on 3D fabrication inside silicon using nanosecond, infrared laser.

Chapter 8 is the summary and outlook.

References

[1] A. B. J. Sullivan and P. T. Houldcroft, "Gas-jet laser cutting," *Br. Weld. J.* 443 (1967).

[2] R. R. Gattass and E. Mazur, "Femtosecond laser micromachining in transparent materials," *Nat. Photonics* **2**, 219 (2008).

[3] F. M. Dickey, Ed., *Laser Beam Shaping: Theory and Techniques* (2014).

[4] J. Turunen and A. T. Friberg, "Chapter 1 – Propagation-Invariant Optical Fields," in *Prog. Opt.* **54** (2010).

[5] A. Marcinkevičius and S. Juodkazis, "Application of Bessel beams for microfabrication of dielectrics by femtosecond laser," *Jpn. J. Appl. Phys.* **40**, 1197 (2001).

[6] M. Kohno and Y. Matsuoka, "Microfabrication and Drilling Using Diffraction-Free Pulsed Laser Beam Generated with Axicon Lens," *JSME Int. J. Ser. B* **47**, 497 (2004).

[7] F. Courvoisier, M. K. Bhuyan, P. A. Lacourt, M. Jacquot, L. Furfaro, and J. M. Dudley, "Material nanoprocessing with nondiffracting femtosecond Bessel beams," *2010 12th Int. Conf. Transparent Opt. Networks, Ict. 2010* **34**, 3163 (2010).

[8] M. K. Bhuyan, F. Courvoisier, P. A. Lacourt, M. Jacquot, R. Salut, L. Furfaro, and J. M. Dudley, "High aspect ratio nanochannel machining using single shot femtosecond Bessel beams," *Appl. Phys. Lett.* **97**, 081102 (2010).

[9] O. Jedrkiewicz, "Experimental investigation of high aspect ratio tubular microstructuring of glass by means of picosecond Bessel vortices," *Appl. Phys. A* **120**, 385 (2015).

[10] C. L. Arnold, S. Akturk, a Mysyrowicz, V. Jukna, a Couairon, T. Itina, R. Stoian, C. Xie, J. M. Dudley, *et al*., "Nonlinear Bessel vortex beams for applications," *J. Phys. B At. Mol. Opt. Phys.* **48**, 094006 (2015).

[11] C. Xie, V. Jukna, C. Milián, R. Giust, I. Ouadghiri-Idrissi, T. Itina, J. M. Dudley, A. Couairon, and F. Courvoisier, "Tubular filamentation for laser material processing," *Sci. Rep.* **5**, 8914 (2015).

[12] D. Grojo, A. Mouskeftaras, P. Delaporte, and S. Lei, "Limitations to laser machining of silicon using femtosecond micro-Bessel beams in the infrared," *J. Appl. Phys.* **117**, 153105 (2015).

[13] P. . Pronko, S. . Dutta, J. Squier, J. . Rudd, D. Du, and G. Mourou, "Machining of sub-micron holes using a femtosecond laser at 800 nm," *Opt. Commun.* **114**, 106 (1995).

[14] D. Du, X. Liu, G. Korn, J. Squier, and G. Mourou, "Laser-induced breakdown by impact ionization in SiO2 with pulse widths from 7 ns to 150 fs," *Appl. Phys. Lett.* **64**, 3071 (1994).

[15] A. P. Joglekar, H.-H. Liu, E. Meyhöfer, G. Mourou, and A. J. Hunt, "Optics at critical intensity: applications to nanomorphing.," *Proc. Natl. Acad. Sci. U. S. A.* **101**, 5856 (2004).

[16] S. I. Kudryashov, G. Mourou, A. Joglekar, J. F. Herbstman, and A. J. Hunt, "Nanochannels fabricated by high-intensity femtosecond laser pulses on dielectric surfaces," *Appl. Phys. Lett.* **91**, 141111 (2007).

[17] J. Fernández-Pradas, "Femtosecond laser ablation of polymethyl-methacrylate with high focusing control," *Appl. Surf. Sci.* **278**, 185 (2013).

[18] S. Juodkazis, K. Nishimura, S. Tanaka, H. Misawa, E. G. Gamaly, B. Luther-Davies, L. Hallo, P. Nicolai, and V. T. Tikhonchuk, "Laser-Induced Microexplosion Confined in the Bulk of a Sapphire Crystal: Evidence of Multimegabar Pressures," *Phys. Rev. Lett.* **96**, 166101 (2006).

[19] J. Békési, J. H. Klein-Wiele, and P. Simon, "Efficient submicron processing of metals with femtosecond UV pulses," *Appl. Phys. A* **76**, 355 (2003).

[20] G. Vaschenko, A. G. Etxarri, C. S. Menoni, J. J. Rocca, O. Hemberg, S. Bloom, W. Chao, E. H. Anderson, D. T. Attwood, *et al*., "Nanometer-scale ablation with a table-top soft x-ray laser," *Opt. Lett.* **31**, 3615 (2006).

[21] M. Dubov, I. Bennion, D. N. Nikogosyan, P. Bolger, and A. V Zayats, "Point-by-point inscription of 250 nm period structure in bulk fused silica by tightly focused femtosecond UV pulses," *J. Opt. A Pure Appl. Opt.* **10**, 025305 (2008).

[22] J.-H. Klein-Wiele and P. Simon, "Sub-wavelength pattern generation by laser direct writing via repeated irradiation," *Opt. Express* **21**, 626 (2013).

[23] J.-H. Klein-Wiele and P. Simon, "Fabrication of periodic nanostructures by phase-controlled multiple-beam interference," *Appl. Phys. Lett.* **83**, 4707 (2003).

[24] J. Bonse, J. Krüger, S. Höhm, and A. Rosenfeld, "Femtosecond laser-induced periodic surface structures," *J. Laser Appl.* **24**, 042006 (2012).

[25] K. Jakubczak, T. Mocek, J. Chalupsky, G. H. Lee, T. K. Kim, S. B. Park, C. H. Nam, V. Hajkova, M. Toufarova, *et al*., "Enhanced surface structuring by ultrafast XUV/NIR dual action," *New J. Phys.* **13**, 053049 (2011).

[26] Y. Shimotsuma, P. G. Kazansky, J. Qiu, and K. Hirao, "Self-Organized Nanogratings in Glass Irradiated by Ultrashort Light Pulses," *Phys. Rev. Lett.* **91**, 247405 (2003).

[27] V. R. Bhardwaj, E. Simova, P. P. Rajeev, C. Hnatovsky, R. S. Taylor, D. M. Rayner, and P. B. Corkum, "Optically Produced Arrays of Planar Nanostructures inside Fused Silica," *Phys. Rev. Lett.* **96**, 057404 (2006).

[28] T.-H. Her, R. J. Finlay, C. Wu, S. Deliwala, and E. Mazur, "Microstructuring of silicon with femtosecond laser pulses," *Appl. Phys. Lett.* **73**, 1673 (1998).

[29] T. L. Andrew, H.-Y. Tsai, and R. Menon, "Confining light to deep subwavelength dimensions to enable optical nanopatterning.," *Science* **324**, 917 (2009).

[30] L. Li, R. R. Gattass, E. Gershgoren, H. Hwang, and J. T. Fourkas, "Achieving lambda/20 resolution by one-color initiation and deactivation of polymerization.," *Science* **324**, 910 (2009).

[31] T. F. Scott, B. a Kowalski, A. C. Sullivan, C. N. Bowman, and R. R. McLeod, "Two-color single-photon photoinitiation and photoinhibition for subdiffraction photolithography.," *Science* **324**, 913 (2009).

[32] Z. Gan, Y. Cao, R. a Evans, and M. Gu, "Three-dimensional deep sub-diffraction optical beam lithography with 9 nm feature size.," *Nat. Commun.* **4**, 2061 (2013).

[33] T. Y. Choi, D. J. Hwang, and C. P. Grigoropoulos, "Femtosecond laser induced ablation of crystalline silicon upon double beam irradiation," *Appl. Surf. Sci.* **197**, 720 (2002).

[34] I. H. Chowdhury, X. Xu, and A. M. Weiner, "Ultrafast double-pulse ablation of fused silica," *Appl. Phys. Lett.* **86**, 151110 (2005).

[35] S. Singha, Z. Hu, and R. J. Gordon, "Ablation and plasma emission produced by dual femtosecond laser pulses," *J. Appl. Phys.* **104**, 113520 (2008).

[36] J. Roth, A. Krauß, J. Lotze, and H. Trebin, "Simulation of Laser Ablation in Aluminum: The Effectivity of Double Pulses," *Appl. Phy. A* **117**, 2207 (2014).

[37] J. Mildner, C. Sarpe, N. Götte, M. Wollenhaupt, and T. Baumert, "Emission signal enhancement of laser ablation of metals (aluminum and titanium) by time delayed

femtosecond double pulses from femtoseconds to nanoseconds," *Appl. Surf. Sci.* **302**, 291 (2014).

[38] Y. Qi, H. Qi, Q. Wang, Z. Chen, and Z. Hu, "The influence of double pulse delay and ambient pressure on femtosecond laser ablation of silicon," *Opt. Laser Technol.* **66**, 68 (2015).

[39] M. Li, S. Menon, J. P. Nibarger, and G. N. Gibson, "Ultrafast Electron Dynamics in Femtosecond Optical Breakdown of Dielectrics," *Phys. Rev. Lett.* **82**, 2394 (1999).

[40] G. Petite, S. Guizard, P. Martin, and F. Quéré, "Comment on 'Ultrafast Electron Dynamics in Femtosecond Optical Breakdown of Dielectrics,'" *Phys. Rev. Lett.* **83**, 5182 (1999).

[41] S. Zoppel, J. Zehetner, and G. A. Reider, "Two color laser ablation: Enhanced yield, improved machining," *Appl. Surf. Sci.* **253**, 7692 (2007).

[42] T. Mocek, J. Polan, P. Homer, K. Jakubczak, B. Rus, I. J. Kim, C. M. Kim, G. H. Lee, C. H. Nam, *et al*., "Surface modification of organic polymer by dual action of extreme ultraviolet/visible-near infrared ultrashort pulses," *J. Appl. Phys.* **105**, 026105 (2009).

[43] K. Obata, K. Sugioka, T. Akane, K. Midorikawa, N. Aoki, and K. Toyoda, "Efficient refractive-index modification of fused silica by a resonance-photoionization-like process using F_2 and KrF excimer lasers," *Opt. Lett.* **27**, 330 (2002).

[44] B. Tan, K. Venkatkrishnan, N. R. Sivakumar, and G. K. Gan, "Laser drilling of thick material using femtosecond pulse with a focus of dual-frequency beam," *Opt. Laser Technol.* **35**, 199 (2003).

[45] T. Jia, H. Chen, M. Huang, F. Zhao, X. Li, S. Xu, H. Sun, D. Feng, C. Li, *et al*., "Ultraviolet-infrared femtosecond laser-induced damage in fused silica and CaF_2 crystals," *Phys. Rev. B* **73**, 054105 (2006).

[46] R. Stoian, M. Boyle, A. Thoss, and A. Rosenfeld, "Dynamic temporal pulse shaping in advanced ultrafast laser material processing," *Appl. Phys. A* **269**, 265 (2003).

[47] C.-H. Lin, Z.-H. Rao, L. Jiang, W.-J. Tsai, P.-H. Wu, C.-W. Chien, S.-J. Chen, and H.-L. Tsai, "Investigations of femtosecond–nanosecond dual-beam laser ablation of dielectrics," *Opt. Lett.* **35**, 2490 (2010).

[48] F. Théberge and S. L. Chin, "Enhanced ablation of silica by the superposition of femtosecond and nanosecond laser pulses," *Appl. Phys. A* **80**, 1505 (2005).

[49] J. Penczak, R. Kupfer, I. Bar, and R. J. Gordon, "The Role of Plasma Shielding in Collinear Double-Pulse Femtosecond Laser-Induced Breakdown Spectroscopy," *Spectrochim. Acta Part B At. Spectrosc.* **97**, 34 (2014).

[50] S. Varma, J. Spicer, B. Brawley, and J. Miragliotta, "Plasma enhancement of femtosecond laser-induced electromagnetic pulses at metal and dielectric surfaces," *Opt. Eng.* **53**, 051515 (2014).

[51] S. Wu, D. Wu, J. Xu, H. Wang, T. Makimura, K. Sugioka, and K. Midorikawa, "Absorption mechanism of the second pulse in double-pulse femtosecond laser glass microwelding," *Opt. Express* **21**, 24049 (2013).

[52] L. Jiang, X. Shi, X. Li, Y. Yuan, C. Wang, and Y. Lu, "Subwavelength ripples adjustment based on electron dynamics control by using shaped ultrafast laser pulse trains," *Opt. Express* **20**, 21505 (2012).

[53] S. Amoruso, R. Bruzzese, and X. Wang, "Plume composition control in double pulse ultrafast laser ablation of metals," *Appl. Phys. Lett.* **95**, 251501 (2009).

[54] L. Jiang, J. Fang, Q. Cao, K. Zhang, and P. Wang, "Femtosecond laser high-efficiency drilling of high-aspect-ratio micro-holes based on free electron density adjustments," *Appl. Opt.* **53**, 7290 (2014).

[55] A. M. Weiner, "Femtosecond pulse shaping using spatial light modulators," *Rev. Sci. Instrum.* **71**, 1929 (2000).

[56] J. Hernandez-Rueda, J. Siegel, M. Galvan-Sosa, A. Ruiz de la Cruz, and J. Solis, "Surface structuring of fused silica with asymmetric femtosecond laser pulse bursts," *J. Opt. Soc. Am. B* **30**, 1352 (2013).

[57] J. Hernandez-Rueda, J. Siegel, D. Puerto, M. Galvan-Sosa, W. Gawelda, and J. Solis, "Ad-hoc design of temporally shaped fs laser pulses based on plasma dynamics for deep ablation in fused silica," *Appl. Phys. A* **112**, 185 (2012).

[58] L. Englert, B. Rethfeld, and L. Haag, M. Wollenhaupt, C. Sarpe-Tudoran, and T. Baumert, "Control of ionization processes in high band gap materials via tailored femtosecond pulses," *Opt. Express* **15**, 17855 (2007).

[59] L. Englert, M. Wollenhaupt, L. Haag, C. Sarpe-Tudoran, B. Rethfeld, and T. Baumert, "Material processing of dielectrics with temporally asymmetric shaped femtosecond laser pulses on the nanometer scale," *Appl. Phys. A* **92**, 749 (2008).

[60] L. Englert, M. Wollenhaupt, C. Sarpe, D. Otto, and T. Baumert, "Morphology of nanoscale structures on fused silica surfaces from interaction with temporally tailored femtosecond pulses," *J. Laser Appl.* **24**, 042002 (2012).

[61] T. Meinl, N. Götte, Y. Khan, T. Kusserow, C. Sarpe, J. Köhler, M. Wollenhaupt, A. Senftleben, T. Baumert, *et al*., "Temporally shaped femtosecond laser pulses as direct patterning method for dielectric materials in nanophotonic applications," *Proc. SPIE* **9126**, 91262B (2014).

[62] E. Louzon, Z. Henis, S. Pecker, Y. Ehrlich, D. Fisher, M. Fraenkel, and a. Zigler, "Reduction of damage threshold in dielectric materials induced by negatively chirped laser pulses," *Appl. Phys. Lett.* **87**, 241903 (2005).

[63] A. S. Arabanian and R. Massudi, "Study on effect of polarization and frequency chirp of incident pulse on femtosecond-laser-induced modification inside silica glass," *J. Opt. Soc. Am. B* **31**, 748 (2014).

[64] C. Milián, A. Jarnac, Y. Brelet, and V. Jukna, "Effect of input pulse chirp on nonlinear energy deposition and plasma excitation in water," *J. Opt. Soc. Am. B* **31**, 2829 (2014).

[65] E. Yazdani, R. Sadighi-Bonabi, H. Afarideh, Z. Riazi, and H. Hora, "Electron heating enhancement by frequency-chirped laser pulses," *J. Appl. Phys.* **116**, 103302 (2014).

[66] J. R. Gulley, J. Liao, and T. E. Lanier, "Plasma generation by ultrashort multi-chromatic pulses during nonlinear propagation," *Proc. SPIE* **8972**, 89720T (2014).

[67] K. M. Davis, K. Miura, N. Sugimoto, and K. Hirao, "Writing waveguides in glass with a femtosecond laser," *Opt. Lett.* **21**, 1729 (1996).

[68] K. Sugioka, Y. Hanada, and K. Midorikawa, "Three-dimensional femtosecond laser micromachining of photosensitive glass for biomicrochips," *Laser Photon. Rev.* **4**, 386 (2010).

[69] Y. Liao, J. Song, E. Li, Y. Luo, Y. Shen, D. Chen, Y. Cheng, Z. Xu, K. Sugioka, *et al.*, "Rapid prototyping of three-dimensional microfluidic mixers in glass by femtosecond laser direct writing.," *Lab Chip* **12**, 746 (2012).

[70] J. Xu, Y. Liao, H. Zeng, Z. Zhou, H. Sun, J. Song, X. Wang, Y. Cheng, Z. Xu, *et al.*, "Selective metallization on insulator surfaces with femtosecond laser pulses," *Opt. Express* **15**, 12743 (2007).

[71] R. Osellame, H. J. W. M. Hoekstra, G. Cerullo, and M. Pollnau, "Femtosecond laser microstructuring: an enabling tool for optofluidic lab-on-chips," *Laser Photon. Rev.* **5**, 442 (2011).

[72] E. G. Gamaly and A. V Rode, "Physics of ultra-short laser interaction with matter: From phonon excitation to ultimate transformations," *Prog. Quantum Electron.* **37**, 215 (2013).

[73] P. Balling and J. Schou, "Femtosecond-laser ablation dynamics of dielectrics: basics and applications for thin films," *Reports Prog. Phys.* **76**, 036502 (2013).

[74] X. Yu, Q. Bian, B. Zhao, Z. Chang, P. B. Corkum, and S. Lei, "Near-infrared femtosecond laser machining initiated by ultraviolet multiphoton ionization," *Appl. Phys. Lett.* **102**, 101111 (2013).

[75] E. G. Gamaly, S. Juodkazis, K. Nishimura, H. Misawa, and B. Luther Davies, "Laser-matter interaction in the bulk of a transparent solid: Confined microexplosion and void formation," *Phys. Rev. B* **73**, 214101 (2006).

[76] Y. Liao, Y. Shen, L. Qiao, D. Chen, Y. Cheng, K. Sugioka, and K. Midorikawa, "Femtosecond laser nanostructuring in porous glass with sub-50 nm feature sizes," *Opt. Lett.* **38**, 187 (2013).

[77] P. C. Verburg, G. R. B. E. Römer, and A. J. Huis in 't Veld, "Two-photon–induced internal modification of silicon by erbium-doped fiber laser," *Opt. Express* **22**, 21958 (2014).

[78] A. H. Nejadmalayeri, P. R. Herman, J. Burghoff, M. Will, S. Nolte, and A. Tünnermann, "Inscription of optical waveguides in crystalline silicon by mid-infrared femtosecond laser pulses.," *Opt. Lett.* **30**, 964 (2005).

[79] M. Mori, Y. Shimotsuma, T. Sei, M. Sakakura, K. Miura, and H. Udono, "Tailoring thermoelectric properties of nanostructured crystal silicon fabricated by infrared femtosecond laser direct writing," *Phys. Status Solidi* **7**, 1 (2015).

[80] Y. Ito, H. Sakashita, R. Suzuki, M. Uewada, K. P. Luong, and R. Tanabe, "Modification and machining on back surface of a silicon substrate by femtosecond laser pulses at 1552 nm," *J. Laser Micro Nanoeng.* **9**, 98 (2014).

[81] R. Grunwald, U. Griebner, F. Tschirschwitz, E. T. Nibbering, T. Elsaesser, V. Kebbel, H. J. Hartmann, and W. Jüptner, "Generation of femtosecond Bessel beams with microaxicon arrays.," *Opt. Lett.* **25**, 981 (2000).

[82] C. J. Sheppard, "Bessel pulse beams and focus wave modes.," *J. Opt. Soc. Am. A* **18**, 2594 (2001).

[83] H. Valtna-Lukner, P. Bowlan, M. Lohmus, P. Piksarv, R. Trebino, and P. Saari, "Measuring the spatio-temporal field of diffracting ultrashort Bessel-type light bullets," *Opt. Express* **17**, 2 (2009).

Chapter 2 - Femtosecond Laser Scribing of Mo Thin Film on Flexible Substrate Using Axicon Focused Beam

This work was presented at the International Manufacturing Research Conference 2015 (NAMRC 43) at Charlotte, North Carolina, on June 11, 2015, and was later published in the paper "Femtosecond laser scribing of Mo thin film on flexible substrate using axicon focused beam", X. Yu, J. Ma, and S. Lei, Journal of Manufacturing Processes **20**, 349 (2015).

Abstract

Ablation experiments of molybdenum (Mo) thin film on flexible polyimide (PI) substrate are conducted using femtosecond laser pulses focused by an axicon lens. The purpose is to assess the capability of axicon lens in producing narrow grooves and how robustness the scribing process is. We first obtain the damage threshold of Mo and PI and then characterize the spatial beam profile produced by the axicon lens through both theoretical calculations and experimental measurements. Then scribing experiments are performed with different pulse energy, scanning speed, and the distance between the axicon tip and the sample's surface. Optical microscope and atomic force microscope are used to examine the microgrooves from the experiments. It is shown that high quality narrow scribes can be produced with axicon focused beam which can tolerate large height fluctuations of moving flexible substrate expected in an industrial setting.

1. Introduction

The multilayer $CuIn_xGa_xSe_{2y}S_y$ (CIGS) thin film solar cell technology has drawn considerable attention due to its unique advantages of low production cost and high photovoltaic energy conversion efficiency. CIGS has been recognized as the most efficient thin-film solar cell technology with conversion efficiency of 20.4% reached in 2013 in a research lab [23]. The

material cost of CIGS thin-film cells can be very inexpensive since it requires few raw materials. The manufacturing cost can be reduced with an efficient, scalable roll-to-roll process. The conventional scribing process for monolithically integrated CIGS modules in production lines typically involves three steps: laser patterning of the Mo back conductor (P1), followed by mechanical patterning of the absorption layer (P2) and finally laser patterning of the front conductor layer (P3) [1]. Currently there is a push for establishing all laser- scribing in thin-film solar panel production.

Q-switched DPSS (diode pumped solid state) lasers emitting at 1064 nm or 355 nm (third harmonic) has been commonly used in industry for P1 scribe [2]. The P2 and P3 processes are typically performed by a frequency-doubled DPSS laser emitting at 532 nm. The pulse duration is usually around several tens of nanoseconds. Despite the popularity of ns lasers in thin film solar cell production, thermal damage due to melting, recast and microcrack formation such as shown by Haas *et al*. [3] limits the scribe quality and line width to >20 μm. The problem is more severe for CIGS type cells on flexible metal/polymer substrate because of the extreme heat sensitivity of the materials [2]. Excessive melting of CIGS and deposition of molybdenum on scribe walls were found to reduce the photovoltaic efficiency considerably [4].

To overcome the shortcomings of ns lasers, ultrafast lasers with ps and fs pulses have been used to scribe CIGS solar cells. It was reported that all P1, P2 and P3 scribing can be performed by ps lasers with desired selectivity of different layers [5,6]. However, thermal effect was shown to be a problem even at this pulse duration (1–10 ps): periodic melting of the molybdenum (Mo) layer and damage to the substrate (especially polyimide) was observed in P1 scribing, electrical shunts were created near scribe edge, and non-uniform ablation leads to residuals in the groove [7–9]. Studies using ultrashort pulses of a few hundred femtoseconds have been conducted and

non-thermal ablation with narrow line width was reported for thin film scribes [10,11]. In addition, a few comparative investigations demonstrated unambiguously the advantages of fs pulses over ns and ps pulses in reduced thermal effects, minimal interdiffusion between multi-layers, improved electrical performance, and narrow line width [12–14]. Recent research in ultrafast laser scribing has extended to use of pulse shaping in both spatial and temporal domain. Square top-hat beam profile has shown advantages such as reduced damage at groove center, smooth scribe edge and insensitiveness to beam quality [15]. Bursts of low energy pulses were found to reduce melt areas in the scribe zone [16].

Despite the advantage femtosecond laser offers in scribing CIGS solar cells, it faces one serious limitation: small depth of field. For example, the Rayleigh length for a laser with wavelength of 1 μm focused to a 10 μm spot size (in diameter) is less than 0.1 mm, which means consistent narrow line width during scribing is impossible to achieve when the height variation for a large moving flexible substrate is expected to be up to 3 mm [17]. In view of the fact that common beam shaping from Gaussian to flattop distribution renders an even shorter depth of field based on the study by Tamhankar *et al*. [17], the purpose of this paper is to study fs laser scribing with axicon focused beam. Use of an axicon lens can generate an intense beam pattern which is referred to as a near-nondiffracting beam, i.e., a beam with much larger depth of focus in comparison to that generated by a conventional focusing lens. Although the goal is to achieve all three patterning processes (P1, P2, P3) with a single fs laser source, the focus of this study is on P1, i.e., scribing Mo thin film on a flexible polyimide (PI) substrate.

2. Experimental setup and procedure

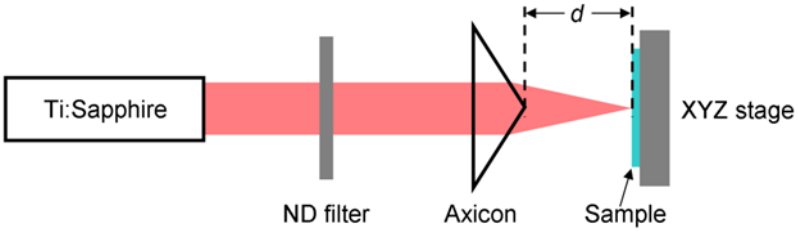

Figure 2.1 Experimental setup.

The experimental setup is shown in Figure 2.1. A Ti:Sapphire femtosecond laser system delivers pulses with full-width-at-half- maximum (FWHM) pulse duration of 60 fs, center wavelength of 800 nm, maximum pulse energy of 4.3 mJ, beam diameter ($1/e^2$) of 10 mm, and repetition rate of 1 kHz. The pulse energy is attenuated by a variable neutral density (ND) filter. The attenuated beam is focused by an axicon lens (Doric Lenses). This axicon lens is made from fused silica, and has a base angle of 25° and a tip angle of 130°. The thin-film sample used in this study consists of a back contact layer (molybdenum, Mo) and a PI substrate. The thicknesses of the Mo layer and the PI layer are ~220 nm and 25 μm, respectively. The Mo thin film was deposited on the PI substrate using electron beam evaporation. The sample is mounted on a motorized XYZ stage (Newport).

Parameter	Value
Pulse energy (μJ)	10, 15, 20, 25, 30, 35
Laser scanning speed (mm/s)	0.1, 0.2, …, 0.9, 1.0
Axicon tip to sample distance (mm)	Fixed at 9 mm

Table 2.1 Experimental condition with fixed distance and different pulse energy and scanning speed

Parameter	Value
Pulse energy (μJ)	Fixed at 15
Laser scanning speed (mm/s)	Fixed at 0.6
Axicon tip to sample distance (mm)	1, 2, 3, …, 18 mm

Table 2.2 Experimental condition with fixed pulse energy and scanning speed at different distances.

Laser scribing experiments are performed on the sample by scanning it across the focal spot. Scribing conditions include pulse energy, scanning speed, and the distance (d) between the axicon tip and the sample's surface. We first place the sample at a fixed distance of 9 mm from the axicon tip, scribe grooves with various combinations of pulse energy and scanning speed, and examine groove quality using optical and atomic force microscopes. Then we apply the optimal combination of energy and speed found above and scribe grooves at different axicon-sample distances. The corresponding experimental conditions are shown in Table 2.1 and Table 2.2, and the results are shown in Section 3.3 and 3.4, respectively. Before conducting the scribing experiments, laser damage threshold of Mo and PI are determined and axicon focused beam profile is characterized to assist in the selection of laser scribing conditions.

3. Results and discussion

3.1 Single pulse damage threshold

Damage threshold is a characteristic dependent on the wavelength, pulse width and type of material. It is ideally defined as the laser fluence at which irreversible damage occurs in the material by removing a monolayer of material. It is actually determined by visual examination, ablation depth measurement, plasma radiation monitoring etc. In this work the damage threshold

is estimated by recording the diameter (D) of the ablated craters using SEM and then using the following relationship between the square of the crater diameter and the logarithm of the laser fluence (F):

$$D^2 = 2w_0^2 \ln\left(\frac{F}{F_{th}}\right) \qquad (2.1)$$

where w_0 and F_{th} are fitting variables, representing focal spot $1/e^2$ radius and damage threshold, respectively. A plot of the square of damage diameter, D^2, against the logarithm of laser fluence is made to obtain both w_0 (from the slope of the line) and F_{th} (from the extrapolation of D^2 to zero value) as shown in Figure 2.2. The Mo and PI damage threshold at 60 fs were found to be 0.18 J/cm^2 and 0.75 J/cm^2, respectively. The Mo damage threshold slightly increases with increased pulse duration, which is consistent with the previous research of fs laser ablation of Cu and Al film and fs laser ablation of fused silica [19,20]. Since the damage threshold of PI is higher than that of Mo, it is possible to only remove the Mo layer while not damaging the PI substrate by choosing a laser fluence in between of these two thresholds. The optimal operating parameters (including pulse energy and scribing speed) are determined in the following scribing experiments.

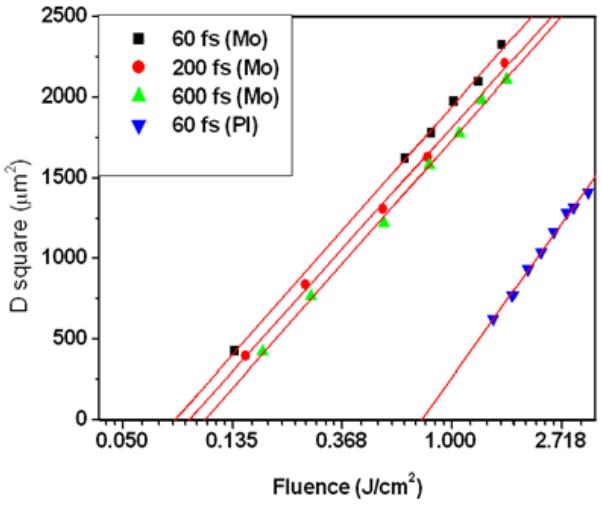

Figure 2.2 Single pulse damage threshold of Mo and PI at various pulse durations.

3.2 Characterization of beam profile produced by axicon lens

We first examine the beam profile after the axicon lens. Ideally, when an infinite plane wave is used as the input beam, an axicon lens with an infinite aperture) will generate an ideal Bessel beam, whose transverse intensity distribution, I(r), remains the same at arbitrary axial location, z, i.e., I(r,z) = I(r,0) [21]. In our experiment, the input beam has a Gaussian profile, resulting in a Bessel-Gauss beam after the axicon, and its intensity distribution is [22]

$$I(r,z) = I_0 \cdot \left(4\pi^2 B^2 \frac{z}{\lambda}\right) \cdot \exp\left[-\frac{2(Bz)^2}{w_0^2}\right] \cdot J_0^2(kBr) \qquad (2.2)$$

where I(r,z) is the intensity distribution after the axicon at transverse position (r) and axial position (z), I_0 is the input beam intensity at r = 0, λ is the wavelength of the laser, w_0 is the input beam $1/e_2$ radius, J_0 is the zero order Bessel function, k is the wave number ($2\pi/\lambda$), and B is the beam deviation angle calculated by

$$B = \arcsin(n \cdot \sin A) - A \qquad (2.3)$$

where n and A are refractive index (1.45) and base angle (25°) of the axicon, respectively. Some of these variables are illustrated in Figure 2.3(a). It should be noted that in the derivation of the above equation, the paraxial assumption, sinB ~ B, is used. For our axicon, B = 0.223 rad and sinB = 0.221, which suggests that the paraxial assumption is valid.

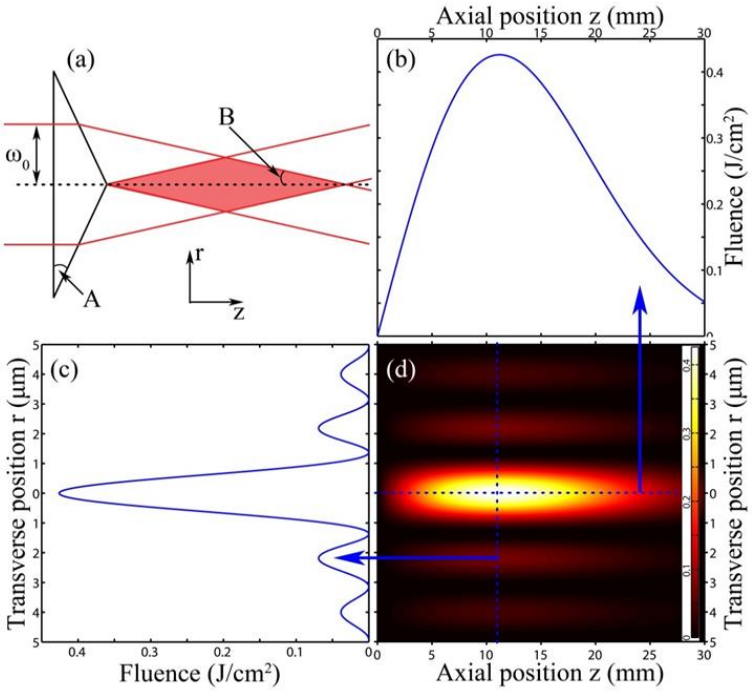

Figure 2.3 Schematic of the laser beam focused by an axicon with a base angle (A) of 25 deg. (b, c) Calculated fluence distribution along the axial and transverse direction, respectively. (d) 2-D plot of fluence distribution. Color bar represents fluence (J/cm^2). Pulse energy is 10μJ. Please note that in (d) the unit of the axial position z is mm.

In machining experiments with ultrashort pulses, laser fluence (F) instead of intensity (I) is the commonly used parameter, and these two are related by $F = I\tau$, where τ is the FWHM pulse duration. The calculated fluence distribution with 10 μJ pulse energy is shown in Figure 2.3(d). Figure 2.3(b) shows the fluence along the axial (z) axis at r = 0, whereas Figure 2.3(c) shows the transverse distribution at z = 11 mm, where the on-axis fluence reaches the maximum. From Figure 2.3(d) we can see that the central spot size (2.7 μm, measured between the first zeros) remains similar along the z-axis. Figure 2.4 shows a comparison between the calculated focus profile (Figure 2.3(a)) and the image of the focal spot seen from a CCD camera at ~3 mm from the tip of

the axicon lens. The measured center spot diameter is about 2.5 μm, which is similar to the calculated value.

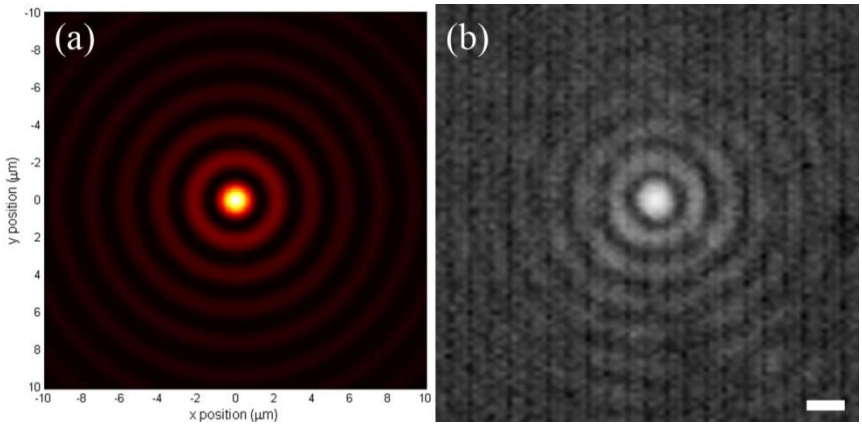

Figure 2.4 Comparison of (a) calculated and (b) measured focal spot profile at 3 mm from the axicon tip. The scale bar in (b) is 2 μm. Both (a) and (b) are on the same spatial scale.

3.3 Mo film scribing at fixed axicon-sample distance

As can be seen in Figure 2.3(b), the on-axis fluence reaches maximum when the axicon-sample distance is 11 mm. However, it is found from our preliminary results (not shown here) that the maximum ablation effect occurs when this distance is around 9 mm instead of the predicted 11 mm, perhaps this is because the spatial profile of our laser beam is not an ideal Gaussian shape. Therefore, in the following experiments in order to identify other parameters, such as the optimal pulse energy and scanning speed, we first place the sample at 9 mm from the axicon tip, and scribe grooves with different pulse energy and speeds.

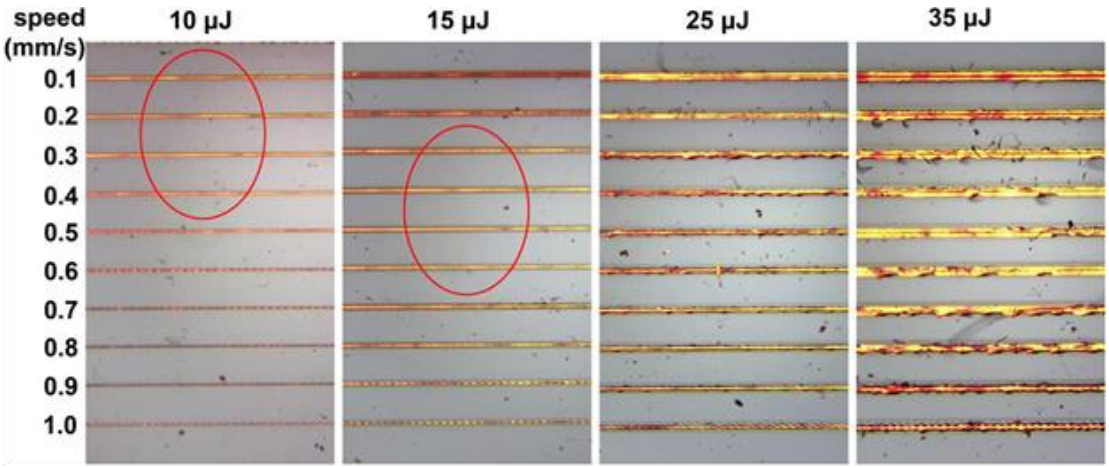

Figure 2.5 Optical images of microgrooves fabricated by different speeds and laser power. The sample is moving transversely at a distance of 9 mm from the axicon tip. Red circles indicate the grooves with good quality.

Figure 2.5 shows the optical images of narrow grooves written on the surface of Mo film with the axicon at different speeds and laser power and at a fixed axicon-sample distance of 9 mm. These images are taken with both front and back illumination. Unprocessed area (between two adjacent lines) shows a white color, whereas written grooves show a yellowish color, indicating that the Mo film is completely or partially removed. As will be confirmed with AFM images (shown below), grooves with completely removed Mo film will show a brighter color compared to those with partially removed coating. Based on these optical imagers, we characterize good-quality grooves as those with bright colors and uniform, narrow widths. From Figure 2.5 we can see that, at low pulse energy, the Mo film can only be removed at speeds of <0.5 mm/s. At higher speeds, the effective energy deposition is less and only a part of the Mo layer is removed. At high energy (e.g. 35 µJ), narrow black lines can be seen in the center of each groove at low speeds (0.1–0.3 mm/s), indicating that the substrate is also damaged (confirmed with AFM imaging, results not shown). The line width is larger and the line edge is rougher compared to low power cases. This is perhaps because the rings of the Bessel beam also cause damage. It appears that good quality

grooves (indicated by red circles in Figure 2.5) can be achieved with either low energy, low speed (10 μJ, 0.1–0.4 mm/s) or high energy, high speed (15 μJ, 0.3–0.6 mm/s). At high speed (~1 mm/s) there is an oscillation at the groove edges, perhaps due to a resonance in the motorized stages. More definitive observations can be made in the AFM images shown in Figure 2.6 for some selected combinations of laser power and scribing speeds.

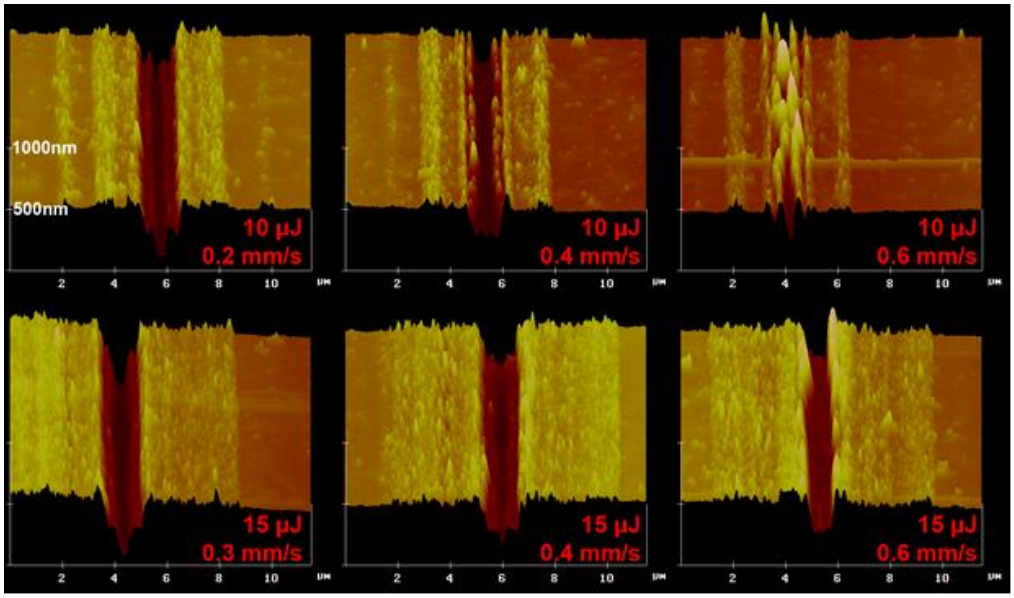

Figure 2.6 AFM images of microgrooves fabricated at different scanning speeds and pulse energy. The distance from the sample surface to the axicon tip is fixed at 9 mm.

These 3D AFM images of the microgrooves show clearly the groove profile as well as the surrounding areas. At the energy of 10 μJ, the Mo film is removed at the speed of 0.2 and 0.4 mm/s, but not at 0.6 mm/s, matching the optical images. Substrate is damaged at 0.2 mm/s as indicated by the deep narrow wedge extending downward from the groove bottom. Although the groove has a relatively flat bottom at 0.4 mm/s, the groove walls are lined with little bumps. As the power is increase slightly to 15 μJ, cleaner grooves are obtained. With the speed increasing from 0.3 to 0.6 mm/s, groove width decreases and damage to the substrate also diminishes. A nice groove is reached at 0.6 mm/s, characterized by flat bottom and straight walls. The groove width

is about 2 μm or less, which is expected because of the central spot size of the beam is about 2.5 μm. It is noted that a HAZ surrounds each groove on both sides and may span a few microns, which may be caused by the ring structures around the central spot. Further results (shown below) support such speculation.

It should also be noted that the optimal combination of pulse energy and scanning speed applies to our specific sample (Mo) and thickness (220 nm), and may differ for another material or thickness. However, as mentioned in Section 3.1 and will be demonstrated in the following section, the long focal range is a universal feature of a Bessel beam. Once the optimal combination is found in a similar way as presented in this section, order-of-magnitude improvement of focal range is expected.

3.4 Mo film scribing at different axicon-sample distances

With fixed pulse energy of 15 μJ and scanning speed of 0.6 mm/s, lines are written on the sample surface at different positions from the axicon tip (ranging from 1 to 18 mm for this condition), as shown in Figure 2.7. No damage is observed when the distance is 1 mm. From these images, we can see that when the distance is either small (2–4 mm) or large (16–18 mm), the Mo film is only partially removed (indicated by the <200 nm depth), and the groove shape shows a high variability along the groove direction. In the middle portion of the distance (6–13 mm), the whole Mo layer is removed (indicated by the grooves' depth of 200 nm and their flat bottoms). In some locations the PI substrate is also damaged (shown in Figure 2.8), and the width also shows variability. We attribute these to the fluctuation of pulse energy, non-uniformity of material and oscillation of the motorized stage. We can see that the groove depth and width remain similar within this distance range from 6 to 13 mm, resulting in an effective range of 7 mm, which is significantly larger than that for an ordinary lens or microscope objective for fabricating such

narrow grooves with width of 2 μm. As an example, for a microscope objective of NA = 0.5 and laser wavelength of 800 nm, the focal spot size is about 2 μm, and the Rayleigh range is $z_R = \pi\omega_0^2/\lambda$ = 4 μm, resulting in a confocal parameter of only 8 μm, which should be compared to the axicon effective range of 7 mm. Hence, by means of an axicon, the effective range for acceptable groove quality is about three orders of magnitude larger. The AFM images reveal that within this range, both the groove quality and width are consistent. This proves that axicon lens is a robust choice for consistent scribing quality when fluctuations in sample height are high.

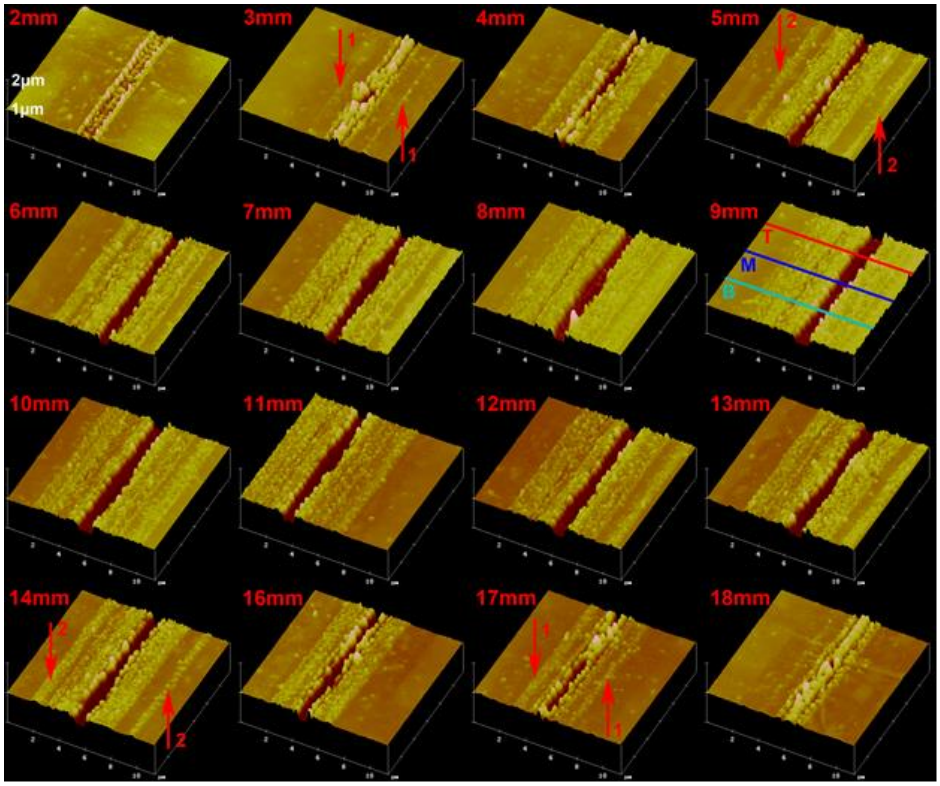

Figure 2.7 AFM images of microgrooves fabricated at different distances between the sample surface and the axicon tip at the scanning speed of 0.6 mm/s and pulse energy of 15 μJ. Arrows indicate two pair of lines (numbered 1 and 2) with bump structures. In the 9 mm figure, T (Top), M (Middle) and B (Bottom) are three positions where cross sections are extracted. Cross sections at similar positions are also extracted in the 12 mm and 14 mm figures. No surface modification is observed for 1 mm, and the image for 15 mm is similar to that for 14 mm. Thus these two images are not shown.

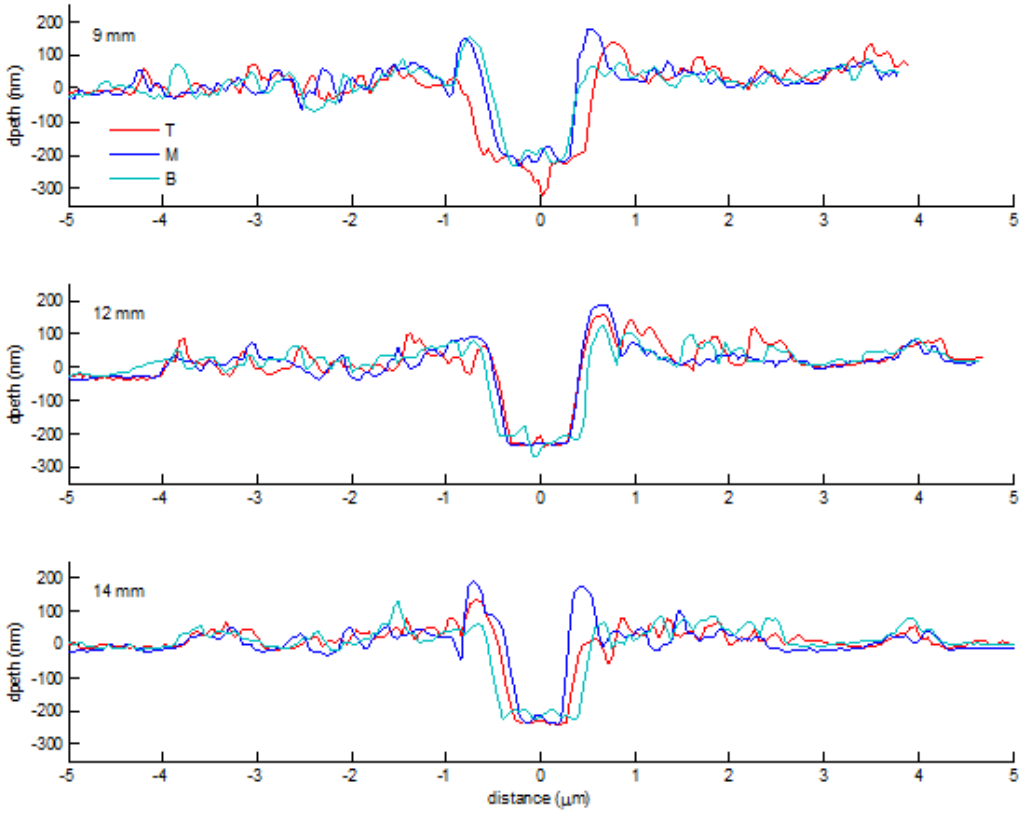

Figure 2.8 Cross sections extracted from Figure 2.7 along three positions indicated by T (Top), M (Middle) and B (Bottom) at d = 9 mm, 12 mm and 14 mm.

A notable feature in Figure 2.7 is the appearance of two pair of distinct lines with bump structures parallel to the central grooves, as can be clearly seen when the axicon-sample distance is 3 mm and 17 mm (indicated by Arrows 1), and 5 mm and 14 mm (indicated by Arrows 2). The locations of these two lines, ~2 μm and ~4 μm to the central groove, respectively, coincide with the positions of the first and second rings surrounding the central spot in the Bessel- Gauss beam, as can be seen from Figure 2.3(c). Therefore, we believe that these bump structures are caused by the ring structures in the beam. Moreover, the damage areas in each side of the central groove are also due to these ring structures. Cross sections are extracted from Figure 2.7 for the 9 mm, 12 mm and 14 mm figures, at three positions T (Top), M (Middle) and B (Bottom) in each figure, and are shown in Figure 2.8. At 9 mm, where the ablation effect is found to be maximal, PI substrate is

clearly damaged at some location (the red Top curve). Better quality grooves with more uniform widths and reduced substrate damage are observed at 12 mm. At 14 mm, while the substrate damage is small, there is a larger width variation compared to the 12 mm case. More quantitative analysis is needed in the future to characterize the quality of each groove in terms of width, depth, heat affected zone (HAZ), electric insulation, etc.

4. Conclusion

The large difference in the laser damage threshold between Mo and PI makes it possible for highly selective removal of Mo thin film on PI substrate. Use of a single axicon lens provides a simple and yet effective way of generating a Bessel like laser beam, which is characterized by a long focal length and small central spot size. The central spot of the Bessel beam has been proven to be a robust option for micromachining as shown in Mo film scribing, because it can provide fairly consistent groove quality while tolerating several millimeters of height fluctuations. Such results can be achieved with different combinations of laser power and scribing speeds. Future work involves quantitative characterization of groove quality, minimizing heat affected zone, and optimizing operating conditions.

Acknowledgment

Financial support of this work by the National Science Foundation under grant no. CMMI-1131627 is gratefully acknowledged.

References

[1] Powalla M, Cemernjak M, Eberhardt J, Kessler F, Kniese R, Mohring HD, et al. “Large-area CIGS modules: pilot line production and new developments,” Sol. Energ. Mat. Sol. 90, 3158 (2006).

[2] Bartlome R, Strahm B, Sinquin Y, Feltrin A, Ballif C. “Laser applications in thin-film photovoltaics,” *Appl. Phys. B* **100**, 427 (2010).

[3] Haas S, Schöpe G, Zahren C, Stiebig H. "Analysis of the laser ablation processes for thin-film silicon solar cells," *Appl. Phys. A* **92**, 755 (2008).

[4] Hermann J, Benfarah M, Bruneau S, Axente E, Coustillier G, Itina T, *et al*. "Comparative investigation of solar cell thin film processing using nanosecond and femtosecond lasers," *J. Phys. D* **39**, 453 (2006).

[5] Huber HP, Herrnberger F, Kery S, Zoppel S. "Selective structuring of thin-film solar cells by ultrafast laser ablation," *Proc SPIE* **6881**, 688117-1 (2008).

[6] Geˇcys P, Markauskas E, Dudutis J, Raˇciukaitis G. "Interaction of ultra-short laser pulses with CIGS and CZTSe thin films," *Appl. Phys. A* **114**, 231 (2014).

[7] Wehrmann A, Puttnins S, Hartmann L, Ehrhardt M, Lorenz P, Zimmer K. "Analysis of laser scribes at CIGS thin film solar cells by localized electrical and optical measurements," *Opt. Laser Technol.* **44**, 1753 (2012).

[8] Zhao X, Cao Y, Nian Q, Shin YC, Cheng G. "Precise selective scribing of thin-film solar cells by a picoseconds laser," *Appl. Phys. A* **116**, 671 (2014).

[9] Wang X, Ehrhardt M, Lorenz P, Scheit C, Ragnow S, Ni XW, *et al*. "The influence of the laser parameter on the electrical shunt resistance of scribed Cu(InGa)Se_2 solar cells by nested circular laser scribing technique," *Appl. Surf. Sci.* **302**, 194 (2014).

[10] Zoppel S, Huber H, Reider GA. "Selective ablation of thin Mo and TCO films with femtosecond laser pulses for structuring thin film solar cells," *Appl. Phys. A* **89**, 161 (2007).

[11] Webb A, Osborne M. "Investigation of laser scribing techniques to improve thin film solar cell manufacturability and performance," *Photovoltaic Specialists Conference (PVSC)*, 002480 (2009).

[12] Kim TW, Pahk HJ, Park HK, Hwang DJ, Grigoropoulos CP. Comparison of multilayer laser scribing of thin film solar cells with femto, pico and nanosecond pulse durations," *Proc SPIE* **7409**, 74090A-1 (2009).

[13] Hermann J, Benfarah M, Coustillier G, Bruneau S, Axente E, Guillemoles JF, *et al*. "Selective ablation of thin films with short and ultrashort laser pulses," *Appl. Surf. Sci.* **252**, 4814 (2006).

[14] Ruthe D, Zimmer K, Hoche T. "Etching of $CuInSe_2$ thin films-comparison of femtosecond and picosecond laser ablation," *Appl. Surf. Sci.* **247**, 447 (2005).

[15] Račiukaitis G, Stankevičius E, Gečys P, Gedvilas M, Bischoff C, Jäger E, *et al*. "Laser processing by using diffractive optical laser beam shaping technique," J. *Laser Micro/Nanoeng.* **6**, 37 (2011).

[16] Gečys P, Račiukaitis G, Miltenis E, Braun A, Ragnow S. "Scribing of thin-film solar cells with picoseconds laser pulses," *Phys. Proc.* **12**, 141 (2011).

[17] Tamhankar A, Bovatsek J, Guadano G, Patel R. "Advantages of using DPSS nanosecond laser with a Gaussian beam shape for scribing thin film photovoltaic panels," ICALEO, 1251 (2009).

[18] Liu JM. "Simple technique for measurements of pulsed Gaussian-beam spot sizes," *Opt. Lett.* **7**, 196 (1982).

[19] Le Harzic R, Breitling D, Weikert M, Sommer S, Fohl C, Valette S, *et al*. "Pulse width and energy influence on laser micromachining of metals in a range of 100 fs to 5 ps," *Appl. Surf. Sci.* **249**, 322 (2005).

[20] Perry MD, Stuart BC, Banks PS, Feit MD, Yanovsky V, Rubenchik AM. "Ultrashort-pulse laser machining of dielectric materials," *J. Appl. Phys.* **85**, 6803 (1999).

[21] Durnin J. "Exact solutions for nondiffracting beams. I. The scalar theory," *J. Opt. Soc. Am. A* **4**, 651 (1987).

[22] Arlt J, Dholakia K. "Generation of high-order Bessel beams by use of an axicon," *Opt. Commun.* **177**, 297 (2000).

[23] Hall M. "EMPA announces 20.4% efficient thin film CIGS-on-polymer cell," *PV Mag.* **1**, 21 (2014).

Chapter 3 - Materials Processing with Superposed Bessel Beams

This work was published in the paper "Materials processing with superposed Bessel beams", X. Yu, C. A. Trallero-Herrero, and S. Lei, Applied Surface Science **360**, 833 (2016).

Abstract

We report experimental results of femtosecond laser processing on the surface of glass and metal thin film using superposed Bessel beams. These beams are generated by a combination of a spatial light modulator (SLM) and an axicon with >50% efficiency, and they possess the long depth-of-focus (propagation-invariant) property as found in ordinary Bessel beams. Through micromachining experiments using femtosecond laser pulses, we show that multiple craters can be fabricated on glass with single-shot exposure, and the 1+(-1) superposed beam can reduce collateral damage caused by the rings in zero-order Bessel beams in the scribing of metal thin film.

1. Introduction

Spatial laser beam shaping provides the possibility of designing beam shapes that are optimized for specific applications [1]. Bessel beams, among these engineered beam shapes, have attracted attention lately due to their interesting properties such as long depth-of-focus (propagation invariance), "self-healing", and the possession of orbital angular momentum [2]. For materials processing, zero- and high-order Bessel beams have been used to drill high-aspect-ratio nanochannels [3,4], produce structures inside silicon and glass [5-9], fabricate circular and ring-shaped surface structures [10-12], scribe narrow grooves [13], and form three-dimensional patterns [14]. One can refer to Ref. 15 for a review on this subject. Other applications with beam shaping techniques include particle manipulation [16], optical microscopy [17], etc. However, materials processing with Bessel beams still lacks the flexibility demonstrated with Gaussian beams. For example, it is demonstrated that complex damage patterns can be fabricated simultaneously by

applying beam-shaping techniques to Gaussian beams [18], thus dramatically reducing processing time. It is desirable to have similar capabilities for Bessel beams. Another problem regarding the use of zero-order Bessel beams is the collateral damage resulting from concentric rings in these beams [6,19]. While such damage can be avoided by lowering input laser power (pulse energy) so that only the intensity of the central lobe exceeds damage threshold [13], these rings cause quality issues when high laser power is required, such as in scribing deep grooves [19].

There currently exist two approaches to the generation of Bessel beam patterns consisting of distinct bright spots. The first approach is an extension of Durnin's ring-slit-and-lens setup [20], where an azimuthal phase modulation with opposite handedness is applied to the ring slit [21]. The limitation is that, in order to obtain superposed modes with high quality, the width of the ring slit should be small (150 μm as reported in [21]). This narrow slit introduces a huge loss (> 90%, estimated by us) to the laser power. One could reduce this loss by transforming the input beam into a ring-shaped beam and focusing it through the ring slit. This, however, would greatly increase the intensity on the phase mask (spatial light modulator) and the risk of damaging it. Another limitation of this approach is that the resultant beam patterns constantly rotate as they propagate, due to the mismatched wave vectors. This rotation impairs the key advantage of Bessel beams in micromachining applications, which is the ability of maintaining the same beam shape over a long distance. In another setup based on a similar idea, two phase masks and two axicons are used to generate a superposition of two first-order Bessel beams [22]. This setup still suffers from high energy loss (76% as reported in [22]) and reduction in depth-of-focus due to pattern rotation. In the second approach, superpositions of Bessel modes are generated by passing Laguerre–Gaussian beams with opposite orders through an axicon [23]. This is a preferred method for micromachining since the resultant beam patterns do not rotate. However, in the previous study, the interfering

Laguerre–Gaussian beams are generated in an interferometer, and further demagnification is required to obtain the final, μm-sized patterns, both involving complex optical systems. Furthermore, the usefulness of these superposed Bessel beams for micromachining applications has not been reported.

In this paper, we use a spatial light modulator (SLM) to generate superpositions of Laguerre–Gaussian beams, which then go through an axicon with a large base angle to form superposed Bessel beam patterns with μm-sized spots. This simple setup, compared with previous work [21,23,24], has high (> 50%) energy efficiency, generates non-diffracting, non-rotating patterns over mm-level range, and shows the capability of forming new beam patterns other than superposed Bessel modes with opposite orders. We use this setup to conduct micromachining experiments with glass and metal thin films, and show that multiple craters can be fabricated on glass with single-shot exposure, and the 1+(-1) superposed beam can reduce collateral damage caused by the rings in the zero-order Bessel beams. Our work shows that the use of superposed Bessel beams, and of spatial beam shaping in general, can lead to improved performance in terms of processing speed, quality and robustness compared to commonly-used Gaussian beams.

2. Experimental

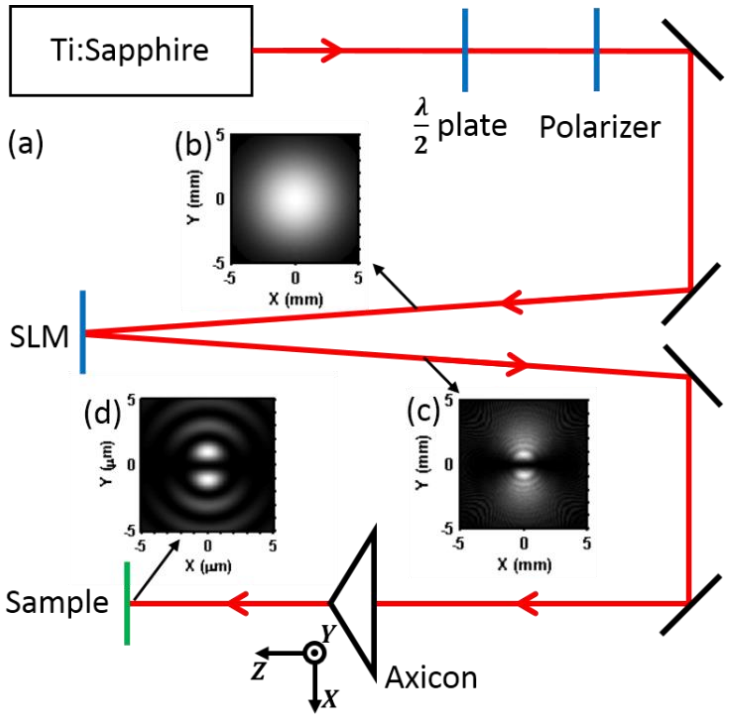

Figure 3.1 (a) Experimental setup. Insets are calculated beam shapes (b) in front of SLM, (c) 1.2 m after SLM, and (d) 9 mm after axicon, respectively, for the 1+(1) superposition.

The experimental setup is shown in Figure 3.1. We use a Ti:Sapphire femtosecond laser system as our laser source. This system delivers 45 fs (full-width-at-half-maximum, FWHM) laser pulses at a center wavelength of 790 nm and a repetition rate of 2 kHz. At the laser output, the beam has a Gaussian shape with $1/e^2$ diameter of 9.8 mm, and the maximum pulse energy is 2 mJ. A combination of a half-wave plate and a polarizer is used to control pulse energy. The polarizer is oriented along the X-axis, ensuring that the beam is *p*-polarized when shining on the SLM (Hamamatsu X10468-02). The angle between the beam into and out from the SLM is about 1°. The beam coming from the SLM is focused by an axicon (Doric Lenses) with 25° base angle and 25.4-mm diameter. The samples are mounted on a motorized XYZ-stage and move at either high speed (50 mm/s) for single-shot irradiation on borosilicate glass (BK-7) or low speed (1 mm/s) for

continuous scribing on molybdenum (Mo) thin film (200-nm thickness). Phase mask images are calculated with Matlab and then loaded onto the SLM. Generated beam patterns are observed with a CMOS camera (Mightex SME-B050-U) with a constant exposure time (25 ms) and a 30× objective lens mounted in front of the image sensor. During the observation the incoming beam is attenuated by a neutral density filter (ND=4.0) placed after the polarizer. Scanning electron (SEM) and atomic force microscopy (AFM) are used to observe the morphology of resultant damage.

3. Results and discussion

3.1 Fabrication of multiple craters on glass with single-shot exposure

The center portions of designed phase masks are shown in Figure 3.2(a0)-(a4) and the masks actually applied on the SLM are shown in Figure 3.2(b0)-(b4). The pixelation in (b0)-(b4) is due to the finite size of SLM pixels (20 μm × 20 μm). The full size of these masks is 16 mm × 12 mm. The first mask (a0) is simply a flat phase mask (replicating a flat mirror), and introduces no phase modulation to the input Gaussian beam. The beam after the axicon is a zero-order Bessel (Bessel-Gaussian) beam. The calculated beam pattern is shown in Figure 3.2(c0), and the experimentally measured pattern is shown in Figure 3.2(d0). This beam generates a single damage spot on borosilicate glass, as shown in Figure 3.2(e0).

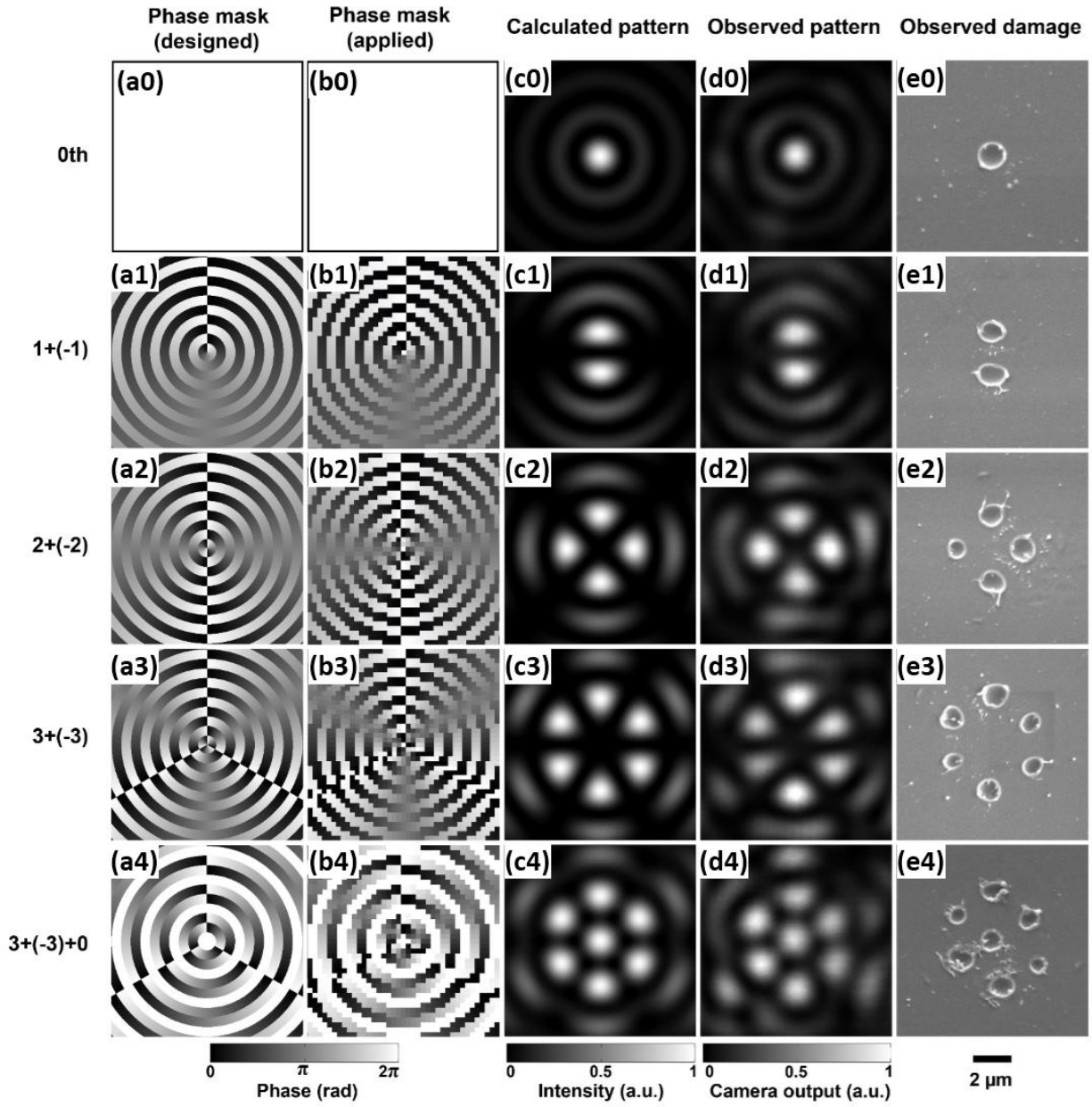

Figure 3.2 Center portions of (a0)-(a4) designed and (b0)-(b4) applied SLM phase masks, (c0)-(c4) calculated patterns and (d0)-(d4) observed patterns. The pixelation in (b0)-(b4) is due to the finite size of SLM pixels. All columns represent Bessel beams of increasing superposed orders denoted on the left of the figures. (e0)-(e4) SEM images of damage generated by the corresponding beam patterns on borosilicate glass. The size of phase masks shown in (a0)-(a4) and (b0)-(b4) is 800 μm×800 μm, and the width of each ring is 40 μm The size of full masks is 16 mm × 12 mm. The size of all the other images is 10 μm×10 μm. All the damage is obtained at about Z=9 mm and with single-pulse exposure. Pulse energies (measured in front of SLM) used to generate damage (e0)-(e4) are 100 μJ, 300 μJ, 500 μJ, 600 μJ and 900 μJ, respectively.

The next three masks (a1)-(a3) are used to generate superpositions of Bessel beams with opposite orders of 1 and -1, 2 and -2, and 3 and -3, respectively. The transmission function for these masks, $T_{l,-l}(r,\theta)$, is

$$T_{l,-l}(r,\theta) = \exp\left[i(-1)^{\left\lfloor \frac{r}{\Delta} \right\rfloor} l\theta\right], \quad (3.1)$$

where l (1, 2 or 3) is the superposed order, r and θ are the radial and azimuthal coordinate, respectively, Δ is the width of each ring, and $\lfloor x \rfloor$ denotes the integer part of the number x. The phase angle of T is then calculated at each pixel location, phase-wrapped between 0 and 2 π, and linearly mapped to an 8-bit bitmap image. This image is loaded onto the SLM. These masks are composed of concentric rings with continuous azimuthal modulation from 0 (black) to 2π (white). The radial coordinate r is used only to determine the handedness of the azimuthal modulation. Every two neighboring rings have opposite modulation directions (handedness), and the number of modulation cycles (l) along each ring is l=1 for (a-1), l=2 for (a-2) and l=3 for (a3). Similar phase masks have been used to generate high-order Laguerre-Gaussian beams [25] and superpositions of Bessel beams when combined with a lens [21]. In this study, these rings with opposite modulation are stacked together to ensure that the generated patterns do not rotate as they propagate (shown later). These masks generate superpositions of Laguerre-Gaussian beams (e.g., Figure 3.1(c)) after the SLM, and these Laguerre-Gaussian beams are focused by the axicon to generate superpositions of Bessel beams with opposite orders, an extension of the work reported previously [26,27].

The electric field in between the SLM and the axicon, and after the axicon, can be obtained by numerically solving the Fresnel diffraction equation using the fast Fourier transform (FFT) method [28]. Formally, the field between the SLM and the axicon is

$$E_1(x,y,z) = \frac{e^{ikz}}{i\lambda z} \iint T_{l,-l}(x',y') T_G(x',y') \exp\left\{\frac{ik}{2z}[(x-x')^2 + (y-y')^2]\right\} dx'dy', \quad (3.2)$$

and the field after the axicon is

$$E_2(x,y,z) = \frac{e^{ik(z-L)}}{i\lambda(z-L)} \iint E_1(x'',y'',L) T_A(x'',y'') \exp\left\{\frac{ik}{2(z-L)}[(x-x'')^2+(y-y'')^2]\right\} dx''dy''. \quad (3.3)$$

In Eqs. (3.2) and (3.3), (x,y,z) is the Cartesian coordinate with the origin at the center of the phase mask; (x',y') and (x'',y'') are the coordinates on the phase mask and the axicon plane, respectively; $T_{l,-l}(x',y')$ is the transmission function of the phase mask (Eq.(3.1)) in the Cartesian coordinate; $T_G(x',y') = \exp\left(-\frac{x'^2+y'^2}{w_0^2}\right)$ is the amplitude modification for Gaussian beams, where w_0 is the waist radius of the input beam; $k = 2\pi/\lambda$ is the wavenumber, where λ is the wavelength; L is the distance between the SLM and the axicon; and $T_A(x'',y'') = \exp(-\frac{i2\pi n \tan\gamma}{\lambda}\sqrt{x''^2+y''^2})$ is the transmission function of the axicon, where n and γ are the refractive index and base angle of the axicon, respectively.

While the intensity at each location can be obtained by numerically solving the Fresnel integrals (Eqs. (3.2) and (3.3)), a closed-form equation based on Ref. [27] can be used to approximate the intensity after the axicon:

$$I_{l,-l}(r,\theta,z) \propto z^{2l+1} \exp\left[\frac{-2(n-1)^2\gamma^2 z^2}{w_0'^2}\right] \times J_l^2[k(n-1)\gamma r] \cos^2\left[l\left(\theta+\frac{\pi}{2}\right)\right], \quad (3.4)$$

where r and z are the radial and axial coordinate, respectively; n and γ are the refractive index and base angle of the axicon, respectively; $w_0'^2$ is the radius of the beam on the axicon; J_l is the *l*-th order Bessel function of the first kind; and $k = 2\pi/\lambda$ is the wavenumber, where λ is the wavelength. The last term in Eq. (3.4), $\cos^2[l(\theta+\frac{\pi}{2})]$, is the azimuthal modulation resulting from the interference of superposed orders. One should note that the beam radius on the axicon (w_0') differs from the original waist radius (w_0) in our setup. This is because the beam profile on the axicon is no longer Gaussian (Figure 3.1(c)), but instead has complex structures. The radius w_0' is

therefore an "effective" radius characterizing the overall intensity distribution on the axicon. This parameter determines the z-position of peak intensity and the range of non-diffracting propagation. In our simulation, we find that w_0'=2.2 mm gives good agreement with the experimental results. From Eq. (3.4) we can estimate the contrast between the peak of central bright spots and the peak of the structures surrounding them. This contrast is $J_0^2(0)/J_0^2(3.8)$=6.2 for the zero-order Bessel beam (l=0), $J_1^2(1.8)/J_1^2(5.3)$=2.8 for l=1, $J_2^2(3.1)/J_2^2(6.7)$=2.4 for l=2, and $J_3^2(4.2)/J_3^2(8)$=2.2 for l=3. Due to this reduction of contrast with increasing l, input laser power should be chosen so that only the central lobes exceed material's damage threshold in order to avoid collateral damage from other parts of the patterns.

Figure 3.2(d1)-(d3) show the experimentally observed patterns, which in general match the calculations (Figure 3.2(c1)-(c3)). Small differences, such as the elongated shape and unequal brightness of the six spots in (d3), are attributed to slight wavefront distortion originating from the input beam and optical elements. In particular, it should be noted that the manufacturing of high-optical-quality axicons is still a challenge for most optics companies. Damage patterns (Figure 3.2(e1)-(e3)) are generated with single-pulse exposure. It should be noted that, while all the bright spots in Figure 3.2(d1)-(d3) have similar intensities – in fact they should have the same intensity distribution according to Eq. (3.4) – the phases of the electric fields in neighboring spots, however, are in π-phase shift, i.e, every two neighboring spots along the azimuthal direction have the opposite signs in the electric-field amplitude, due to the azimuthal modulation term in Eq. (3.4).

In Figure 3.2(a4), we insert a flat-phase ring between every pair of oppositely-modulated rings. This mask can be seen as a combination of (a0) and (a3), and generates a beam pattern similar to (d3) but with the addition of a central lobe. This new pattern can be considered as a

combination of the zero-order Bessel beam and the 3+(-3) superposition. The resultant damage is shown in Figure 3.2(e4), where an added damage spot at the center can be seen.

In obtaining Figure 3.2 (and following Figure 3.3 and Figure 3.4), the width of each ring (Δ in Eq. (3.1)) in the phase masks is 40 μm (corresponding to the size of 2 pixels on the SLM), and the beam path (L) from the SLM to the axicon is fixed at 2.5 m. First, regarding the ring width, we find that nearly identical beam shapes can be generated when Δ is between 20 μm (1 pixel) and 160 μm (8 pixels). The resultant patterns become distorted when Δ is larger than 180 μm (9 pixels). Surprisingly, despite the heavy pixelation of the 1-pixel-width phase masks, high-quality patterns can still be generated. We use 2-pixel-width masks in this study to reduce unknown effects arising from heavy pixelation. Second, regarding the beam path L, there is no noticeable difference in the generated patterns when L is changed between 1.5 and 4.5 m, which is the range we can conveniently achieve with the current setup. Our computer simulation confirms that similar beam patterns can be generated from L~0 (if using a transmission SLM immediately followed by an axicon) to L=110 m. While we do not observe significant change in the beam profile when L is between 1.5 and 4.5 m, one should check this and verify that it meets one's requirement when working at long L.

The energy efficiency of this "SLM + axicon" method is defined as the ratio of output pulse energy (measured in front of the axicon) to input pulse energy (measured after the polarizer). The energy after the axicon is not measured to avoid damaging the power meter sensor with the intense beam patterns. Since our axicon is made of fused silica with high transmission at the laser wavelength, the energy loss (estimated <10%) from the axicon is mainly due to reflection on the uncoated surfaces, and can be reduced with anti-reflective coatings. Therefore such loss is not included in this measurement. Furthermore, the focus of our paper is to show that the inclusion of

an SLM does not introduce large additional loses, and the axicon would be equivalent to a focusing lens in the "ring-aperture and convex lens" setup. Our results show that the efficiency for generating the zero-order beam (Figure 3.2(d0)) is 97%, and the efficiencies for other beam patterns (Figure 3.2(d1)–(d4)) are 60%, 55%, 54% and 52%, respectively. The energy loss is caused by diffraction on the SLM due to the complex phase masks. It should be noted that, even if the efficiencies for generating the superposed beams are almost the same, more input pulse energies, increasing from 100 μJ for Figure 3.2(e1) to 900 μJ for Figure 3.2(e4), are required to produce more damage spots. We use large pulse energies (especially for more complex patterns) to ensure that all of the damage spots can be observed. When working with large pulse energies, one should choose appropriate laser parameters (beam diameter, pulse duration, repetition rate, etc.) to avoid damaging SLMs due to excessive heating in the liquid-crystal. In this experiment, these parameters are chosen so that our SLM can output stable phase modulation for 10-hour continuous irradiation at the maximum load.

To estimate the peak intensities of the beam patterns relative to that of the zeroth-order beam, we take images of these patterns together with the zeroth-order pattern with the same input power. The power is checked after the polarizer, and then attenuated by an ND=4.0 filter. Our imaging system has been checked to be linear in the range of values of interest. We find that, relative to the zeroth-order beam, the peak intensities are 46% for the 1+(-1) pattern, 37% for 2+(-2), 27% for 3+(-3), and 15% for 3+(-3)+0. This reduction in peak intensities is the reason that more pulse energies are required to generate multiple craters shown in Figure 3.2.

3.2 The long depth-of-focus (propagation-invariant) property of generated beams

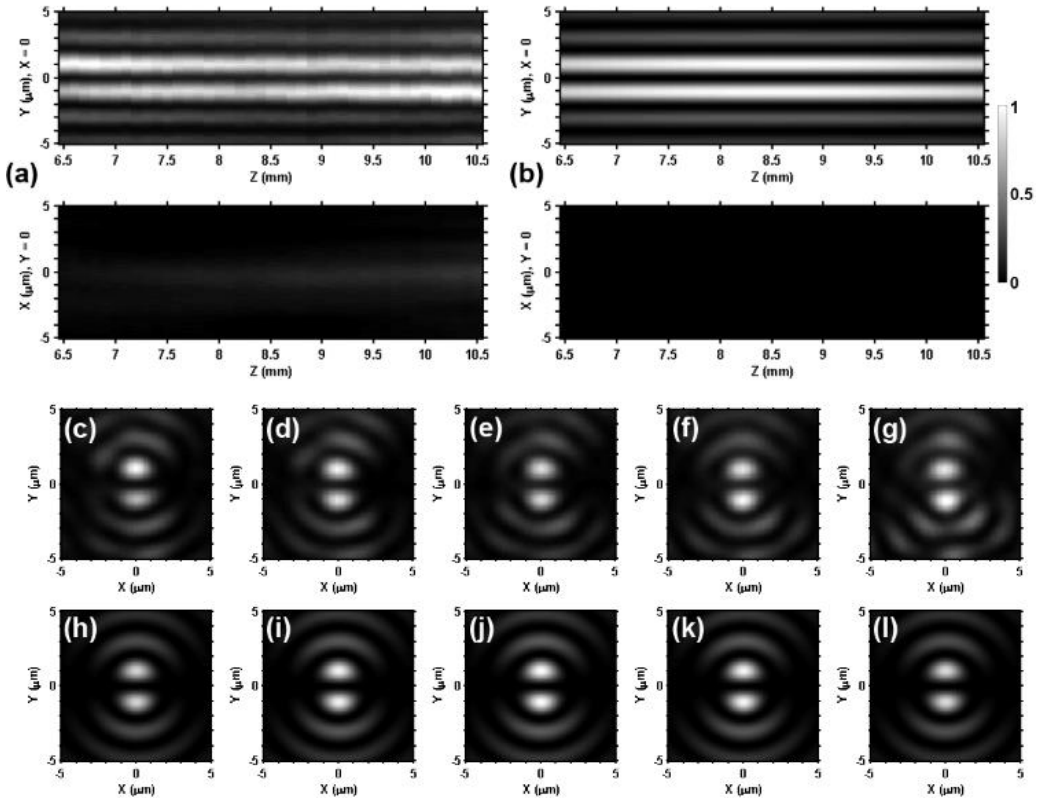

Figure 3.3 Propagation of the +1(-1) superposed Bessel beam. (a) Observed and (b) calculated beam profiles in YZ (X=0) and XZ (Y=0) planes. (c-g) Observed and (h-l) calculated beam shapes at Z=6.5, 7.5, 8.5, 9.5 and 10.5 mm, respectively.

The propagation-invariant property of these superposed Bessel beams is demonstrated in Figure 3.3, using the 1+(-1) superposition as an example. We take images of beam patterns from Z=6.5 mm to 10.5 mm (Z=0 is at the axicon tip), with 0.1-mm step size and 25-ms camera exposure time, and plot YZ and XZ profiles in Figure 3.3(a). Beam shapes at five locations (Z=6.5, 7.5, 8.5, 9.5 and 10.5 mm) are shown in Figure 3.3(c-g). For comparison, simulation results based on Eq. (4.2) are shown in Figure 3.3(b) and (h-l). In the YZ-plane, we can see that measured profiles show two strong lobes, spanning across the entire Z-range, in consistence with the simulation data. In the XZ-plane, weak intensity distribution is observed at the beam's trailing portion, while simulation shows nearly zero intensity in this entire region. From Figure 3.3(c-g), we observe

almost unchanged beam shapes from Z=7.5 to 9.5 mm, resulting in a 2-mm depth-of-focus. For comparison, a focused Gaussian beam with a waist diameter of 2 μm (similar to the size of one lobe in the superposed beam) has a confocal length of only 8 μm. At Z=6.5 mm and 10.5 mm, the intensity of one of the lobes becomes higher than the other, while simulation shows equal intensities at each Z location. This discrepancy, together with the weak intensity distribution in the XZ-plane, is attributed to the imperfect input beam and optical elements. The non-diffracting length of a zero-order Bessel beam can be estimated geometrically as $D = w_0/[(\mathrm{n}-1)\gamma]$ = 25.5 mm. For the 1+(-1) superposed beam, w_0' instead of w_0 should be used, and this gives $D' = w_0'/[(\mathrm{n}-1)\gamma]$ = 11.2 mm. Other superposed beams have similar, mm-order depth-of-focus (results not shown). It is worth pointing out that these superposed beam patterns do not rotate as they propagate, in contrast to previous results [21,22]. This "nonrotating" feature ensures that similar damage patterns can be generated within a long depth-of-focus, which is convenient for the fabrication of microstructures on uneven surfaces, such as moving rolls of solar thin film (which will be used later in this study).

3.3 Scribing of Mo thin film with the 1+(-1) superposed beam

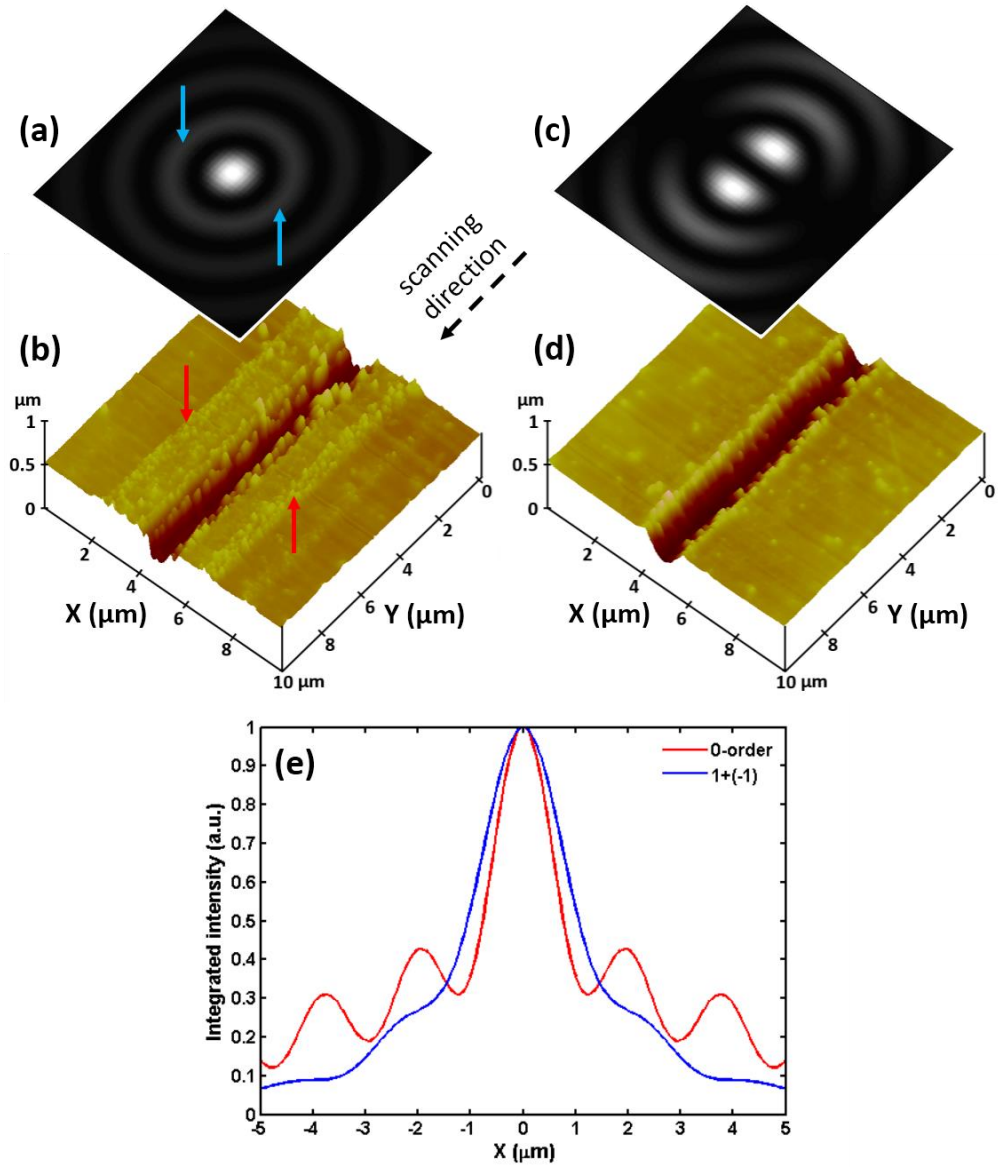

Figure 3.4 Comparison of groove scribing with (a, b) zero-order and (c, d) 1+(-1) superposed Bessel beams. (a) and (c) are calculated beam shapes, and (b) and (d) are AFM images of grooves scribed with corresponding beams. A pair of damage tracks is indicated with red arrows in (b), and is believed to be caused by sections of rings indicated by blue arrows in (a). In both cases, the scanning speed is 1 mm/s, and the samples are placed at Z=9 mm. Pulse energies (estimated peak fluences) are 10 μJ (0.42 J/cm^2) for (b) and 20 μJ (0.38 J/cm^2) for (d) (e) shows a comparison of intensities integrated along the scanning direction between two cases. The integrated intensities are normalized to their peak values.

It has been reported that, while zero-order Bessel beams offer substantial increase in depth-of-focus compared to Gaussian beams, the concentric rings in the zero-order beams can cause undesired damage [6,19]. Shown in Figure 3.4(b) is an AFM image of a narrow groove scribed on Mo thin film with a zero-order Bessel beam (illustrated in Figure 3.4(a)). The groove width is 1.3~1.4 μm and the depth is about 200 nm. A pair of damage tracks (indicated with red arrows in Figure 3.4(b)) parallel to the central groove can be seen. A single track on the right-hand side is also visible. It is further found that the distances between these tracks and the center of the groove coincide with the radii of the first and the second rings (2 and 4 μm, respectively) in our zero-order beam. Therefore, we conclude that these tracks are caused by sections of these rings, the sections (indicated by blue arrows in Figure 3.2(a)) that are located at about 90° angle to the scribing direction. This is because these sections overlap more on the sample than the other sections along the ring, and therefore can cause damage more easily. The missing track in the second pair is attributed to uneven intensity distribution of the second ring, as can be seen in Figure 3.2(d0).

These results suggest that, if the 1+(-1) superposed beam is used and aligned such that the scanning direction is parallel to the two lobes, such collateral damage can be reduced, since there is nearly zero intensity in those sections. To demonstrate this, we scribe a groove with similar width and depth using the 1+(-1) beam, and the result is shown in Figure 3.4(c) and (d). We observe a clean groove without any damage tracks, in consistence with the analysis above. Small bumps observed in Figure 3.4(d) are random debris and defects on the surface, and are not damage from the beam. Comparing Figure 3.4(b) and (d), we also observe reduced roughness at the groove walls when the superposed beam is used. This is perhaps due to the fact that, with the superposed beam, every location on the sample is scribed twice by the two lobes, and the second scribing can smooth the rough surface after the first scribing. The peak fluence for the zero-order beam is estimated

from our previous study [19] to be 0.42 J/cm^2, and that for the 1+(-1) beam is calculated to be 0.38 J/cm^2 using the results of relative intensities from Section 3.1.

The improved quality from the superposed beam can also be explained by calculating the intensity profiles integrated along the scanning (*Y*) direction, as shown in Figure 3.4(e). These integrated intensity profiles represent the total power delivered to the sample per unit distance along the *X*-direction, under the condition that shot-to-shot overlapping is high (> 75% in our case). One can see from Figure 3.4(e) that, when the same amount of power is delivered at the center, at locations away from the center ($|X| >1$ μm), the 1+(-1) beam introduces less power than the zero-order beam. More importantly, the curve for the superposed beam increases monotonically from either side of the *X*-axis, as opposed to the zero-order beam for which local maxima exist. This is the reason that a distinct groove can be generated with the superposed beam, whereas multiple damage tracks appear for the zero-order beam.

We also find that, with the 1+(-1) beam, the width of scribed grooves is 1.7~1.8 μm, larger than that (1.3~1.4 μm) with the zero-order beam. We attribute this to the slightly larger beam size for the 1+(-1) beam. Specifically, the groove width with the 1+(-1) beam is determined by the maximum width of one of the two central spots, measured perpendicularly to the writing direction. From Eq. (3.2) we can calculate that the full-width-at-half-maximum (FWHM) is 1.8 μm, whereas the FWHM for the zero-order is 1.3 μm. These numbers agree well with measured groove widths. To reduce the widths, one can focus the 1+(1) beam more tightly with a sharper axicon. For example, our calculation based on Eq. (3.2) shows that to get the same width as the zero-order beam (1.3 μm), the base angle should be increased to 30°.

In writing complex structures with the 1+(-1) pattern, another factor one should take into account is that the orientation of this pattern should be constantly adjusted so that the two central

lobes are always parallel to the writing direction. This can be achieved by rotating the phase mask on the SLM (and consequently changing the pattern's orientation) in synchronization with the XYZ-stages.

4. Conclusion

We use the "SLM + axicon" setup to generate superposed Bessel beams with opposite orders with high efficiency. Designing new beam patterns is possible by tweaking phase masks on the SLM. These beams can be used to fabricate micro-scale structures with the advantages of increased depth-of-focus, programmable patterns and reduced processing time. We also demonstrate that the 1+(-1) superposition can reduce collateral damage caused by ordinary zero-order Bessel beams.

Acknowledgements

Financial support from the National Science Foundation under Grant Number CMMI 1131627 is gratefully acknowledged. C. T-H and laser support is provided by the Chemical Sciences, Geosciences, and Biosciences Division, Office of Basic Energy Sciences, Office of Science, U.S. Department of Energy (DOE) under Grant No. DE-FG02-86ER13491.

References

[1] F. M. Dickey (Ed.), Laser Beam Shaping: Theory and Techniques, second ed., CRC Press, Florida, 2014.

[2] J. Turunen, A. T. Friberg, Chapter 1 - Propagation-invariant optical fields, Prog. Opt. 54 (2010) 1.

[3] M. K. Bhuyan, F. Courvoisier, P. A. Lacourt, M. Jacquot, R. Salut, L. Furfaro, J. M. Dudley, High aspect ratio nanochannel machining using single shot femtosecond Bessel beams, Appl. Phys. Lett. 97 (2010) 081102.

[4] M. K. Bhuyan, P. K. Velpula, J. P. Colombier, T. Olivier, N. Faure, R. Stoian, Single-shot high aspect ratio bulk nanostructuring of fused silica using chirp-controlled ultrafast laser Bessel beams, Appl. Phys. Lett. 104 (2014) 021107.

[5] D. Grojo, A. Mouskeftaras, P. Delaporte, S. Lei, Limitations to laser machining of silicon using femtosecond micro-Bessel beams in the infrared, J. Appl. Phys. 117 (2015) 153105.

[6] J. Amako, K. Yoshimura, D. Sawaki, T. Shimoda, Laser-based microprocesses using diffraction-free beams generated by diffractive axicons, Proc. SPIE 5713 (2005) 497.

[7] M. Mikutis, T. Kudrius, G. Šlekys, D. Paipulas, S. Juodkazis, High 90% efficiency Bragg gratings formed in fused silica by femtosecond Gauss-Bessel laser beams, Opt. Mater. Express 3 (2013) 1862.

[8] L. Zhao, F. Wang, L. Jiang, Y. Lu, W. Zhao, J. Xie, X. Li, Femtosecond Bessel-beam-assisted high-aspect-ratio microgroove fabrication in fused silica, Chin. Opt. Lett. 13 (2015) 041405.

[9] X. Long, J. Bai, W. Zhao, R. Stoian, R. Hui, G. Cheng, Stressed waveguides with tubular depressed-cladding inscribed in phosphate glasses by femtosecond hollow laser beams, Opt. Lett. 37 (2012) 3138.

[10] B. Wetzel, C. Xie, P.-A. Lacourt, J. M. Dudley, F. Courvoisier, Femtosecond laser fabrication of micro and nano-disks in single layer graphene using vortex Bessel beams, Appl. Phys. Lett. 103 (2013) 241111.

[11] W. Cheng, P. Polynkin, Micromachining of borosilicate glass surfaces using femtosecond higher-order Bessel beams, J. Opt. Soc. Am. B 31 (2014) C48.

[12] R. Sahin, T. Ersoy, S. Akturk, Ablation of metal thin films using femtosecond laser Bessel vortex beams, Appl. Phys. A 118 (2014) 125.

[13] B. Yalizay, T. Ersoy, B. Soylu, S. Akturk, Fabrication of nanometer-size structures in metal thin films using femtosecond laser Bessel beams, Appl. Phys. Lett. 100 (2012) 031104.

[14] B. Bhuian, R.J. Winfield, S. O'Brien, G.M. Crean, Pattern generation using axicon lens beam shaping in two-photon polymerisation, Appl. Surf. Sci. 254 (2007) 841.

[15] M. Duocastella, C.B. Arnold, Bessel and annular beams for materials processing, Laser Photon. Rev. 6 (2012) 607.

[16] T. Čižmár, V. Kollárová, X. Tsampoula, F. Gunn-Moore, W. Sibbett, Z. Bouchal, K. Dholakia, Generation of multiple Bessel beams for a biophotonics workstation, Opt. Express 16 (2008) 14024.

[17] B.-C. Chen, W. R. Legant, K. Wang, L. Shao, D. E. Milkie, M. W. Davidson, C. Janetopoulos, X. S. Wu, J. A. Hammer 3rd, Z. Liu, B. P. English, Y. Mimori-Kiyosue, D. P. Romero, A. T. Ritter, J. Lippincott-Schwartz, L. Fritz-Laylin, R. D. Mullins, D. M. Mitchell, J. N. Bembenek, A. C. Reymann, R. Böhme, S. W. Grill, J. T. Wang, G. Seydoux, U. S. Tulu, D. P. Kiehart, E. Betzig, Lattice light-sheet microscopy: Imaging molecules to embryos at high spatiotemporal resolution. Science 346 (2014) 1257998.

[18] J. Békési, J. H. Klein-Wiele, P. Simon, Efficient submicron processing of metals with femtosecond UV pulses, Appl. Phys. A 76 (2003) 355.

[19] X. Yu, J. Ma, S. Lei, Femtosecond laser scribing of Mo thin film on flexible substrate using axicon focused beam, J. Manuf. Process., In press.

[20] J. Durnin, J. J. Miceli, Jr., J. H. Eberly, Diffraction-free beams, Phys. Rev. Lett. 58 (1987) 1499.

[21] R. Vasilyeu, A. Dudley, N. Khilo, A. Forbes, Generating superpositions of higher-order Bessel beams, Opt. Express 17 (2009) 23389.

[22] Nicholas Barbieri, Matthew Weidman, Gregory Katona, Matthieu Baudelet, Zachary Roth, Eric Johnson, Georgios Siviloglou, Demetrios Christodoulides, Martin Richardson, Double helical laser beams based on interfering first-order Bessel beams, J. Opt. Soc. Am. A 28 (2011) 1462-1469.

[23] D. McGloin, V. Garcés-Chávez, K. Dholakia, Interfering Bessel beams for optical micromanipulation, Opt. Lett. 28 (2003) 657.

[24] J. Fan, E. Parra, I. Alexeev, K. Y. Kim, H. M. Milchberg, L. Ya. Margolin, L. N. Pyatnitskii, Tubular plasma generation with a high-power hollow Bessel beam, Phys. Rev. E 62 (2000) R7603.

[25] N. Matsumoto, T. Ando, T. Inoue, Y. Ohtake, N. Fukuchi, T. Hara, Generation of high-quality higher-order Laguerre-Gaussian beams using liquid-crystal-on-silicon spatial light modulators, J. Opt. Soc. Am. A 25 (2008) 1642.

[26] V. Jarutis, R. Paškauskas, A. Stabinis, Focusing of Laguerre–Gaussian beams by axicon, Opt. Commun. 184 (2000) 105.

[27] J. Arlt, K. Dholakia, Generation of high-order Bessel beams by use of an axicon, Opt. Commun. 177 (2000) 297.

[28] D. G. Voelz, Computational fourier optics: a MATLAB tutorial, SPIE Press, Washington, 2011.

Chapter 4 - Near-Infrared Femtosecond Laser Machining Initiated by Ultraviolet Multiphoton Ionization

The feasibility of UV-IR machining with reduced UV damage threshold is demonstrated in this chapter. This work was published in the paper "Near-infrared femtosecond laser machining initiated by ultraviolet multiphoton ionization", X. Yu, Q. Bian, B. Zhao, Z. Chang, P.B. Corkum, and S. Lei, Applied Physics Letters **102**, 101111 (2013).

Abstract

We report on the experimental study of microstructures fabricated on the surface of fused silica by two femtosecond laser pulses, a tightly focused 266 nm beam followed by a loosely focused 800 nm beam. By setting the fluence of each pulse below the damage threshold, visible microstructures are fabricated using the combined beams. Our results suggest that the ultraviolet pulse generates seed electrons through multiphoton absorption and the near-infrared pulse utilizes these electrons to cause damage by avalanche ionization.

1. Introduction

Femtosecond laser micromachining has been widely studied for various applications because of its unique advantages such as reduced thermal effect [1-3]. Due to the high nonlinearity of the interaction between femtosecond laser and transparent materials, e.g., fused silica, damage features are localized within focal volumes [4, 5], and nanoscale features can be achieved by pulse energy control [6], use of near-field scanning microscopes [7], self-focusing [8], etc. Fundamentally, the minimum feature size is determined by the diffraction limit on the order of λ/NA, where λ is laser wavelength and NA is the numerical aperture of focusing optics. Using high NA objectives, small holes with diameters of 200 nm are fabricated [9]. Alternatively, using

extreme ultraviolet (XUV) pulses of tens of nanometers wavelength generated through high harmonic generation (HHG) [10, 11], feature size can be controlled at the nanometer level. However, due to the low conversion efficiency of HHG, direct machining of dielectrics using HHG is a challenge. Furthermore, for mass production purposes, separation of laser beams to form several foci can increase production speed, so a machining technique requiring lower pulse energy, even below damage threshold, is desired.

Since laser pulses with a shorter wavelength have a larger cross section to excite free electrons from the valance band to the conduction band by photoionization [11], it is possible to use a short wavelength pulse to generate seed electrons and a long wavelength pulse to cause an electron avalanche [12]. With the help of the long wavelength pulse, the energy of the short wavelength pulse might be kept below its damage threshold, and damage can only form within the seeding volume defined by the short wavelength pulse. This provides a possible route to XUV (or even shorter wavelength) [13, 14] laser nanomachining with energy below damage threshold.

Several studies have been carried out to investigate the effects of combining two femtosecond pulses or two-color nanosecond pulses on machining of different materials, and their main concern was ablation enhancement and threshold reduction [13, 15-19]. This paper focuses on the multiphoton and avalanche processes by an ultraviolet-near-infrared (UV-NIR) pulse train to reveal the mechanism of damage formation and the control of damage size defined by the short wavelength pulse. We choose UV light as seeding pulses instead of XUV because no vacuum devices are needed. The results discussed in this paper are universal and can be applied to an XUV-NIR setup for nanoscale machining.

2. Experimental

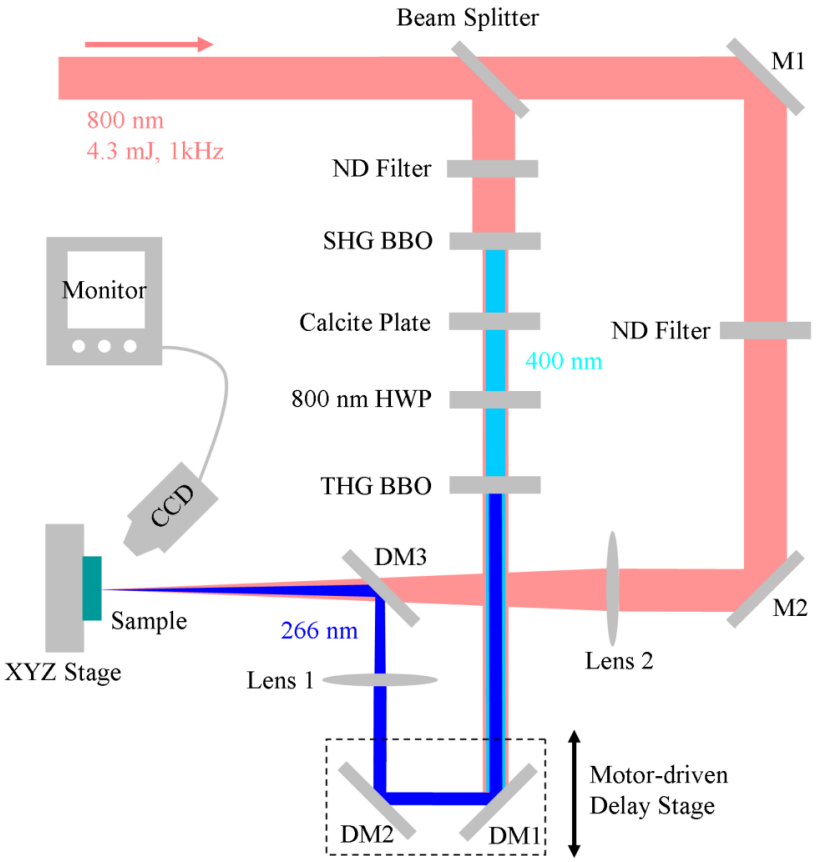

Figure 4.1 Experimental setup

Figure 4.1 shows the experimental setup. A femtosecond (fs) laser system delivers 60 fs (full width at half maximum, FWHM) laser pulses at the center wavelength of 800 nm with the maximum pulse energy of 4.3 mJ and repetition rate of 1 kHz. The beam is split into two arms (UV and NIR arm) after a beam splitter. 90% of the beam is reflected (UV arm) and directed through a third harmonic generation (THG) module (Eksma Optics). The barium borate (BBO) crystal generates the second harmonic (400 nm) of the fundamental (NIR) beam. A calcite plate is used to compensate for the group velocity delay between the second harmonic and the NIR pulses. A zero-order wave-plate (half-wave at 800 nm and full-wave at 400 nm) makes the 400 and the 800 nm polarize in the same direction so that the 266 nm (UV) pulses is generated in another BBO

crystal through sum frequency generation. The pulse duration of the UV pulses is estimated to be 70 fs. The maximum UV pulse energy is 20 μJ, resulting in a conversion efficiency of 0.5%. The energy is adjusted by a neutral-density (ND) filter before the first BBO. After the THG module, only the UV beam is efficiently reflected by two dichroic mirrors (DM1 and DM2, Layertec) mounted on a motor-driven delay stage. Then the UV beam is focused by a lens (50 mm focal length). The 800 nm beam in the NIR arm is focused by another lens (200 mm focal length), and its energy is controlled by an ND filter.

The focused UV and NIR beams are combined with another dichroic mirror (DM3) and both foci are carefully aligned on the sample surface. The focal spot size ($2w_0$) for the UV and NIR measured by the knife-edge method is 9.2 μm and 25.4 μm, respectively, where w_0 is the $1/e^2$ radius. The samples are square fused silica plates of 25.4 mm wide and 2 mm thick (Corning 7980). The samples are mounted on a motor-driven three-axis stage. To temporally overlap the UV and NIR beams, a 200 μm thick BBO crystal is inserted after DM3 and the difference frequency generation of 400 nm from the UV and NIR is observed. Zero delay is defined when the generated 400 nm light is the strongest, with an accuracy of ~30 fs.

In the experiments, both the UV and NIR energy fluence are kept below their respective damage threshold (0.87 J/cm^2 for UV and 2.17 J/cm^2 for NIR), so that no visible damage is observed with a charge-coupled device (CCD) camera when only one beam is applied. At a fixed NIR fluence and a relative delay to the UV pulse, UV energy is carefully adjusted (still kept below its damage threshold) to a level that visible damages are starting to appear. By this method, the damage threshold energy range can be narrowed down to an acceptable level. It should be noted that different methods have been used in determining damage threshold, such as direct observation,

plasma emission, light transmission, etc [12, 17, 20]. Our method is similar to the one used in ref. [20].

3. Results and discussion

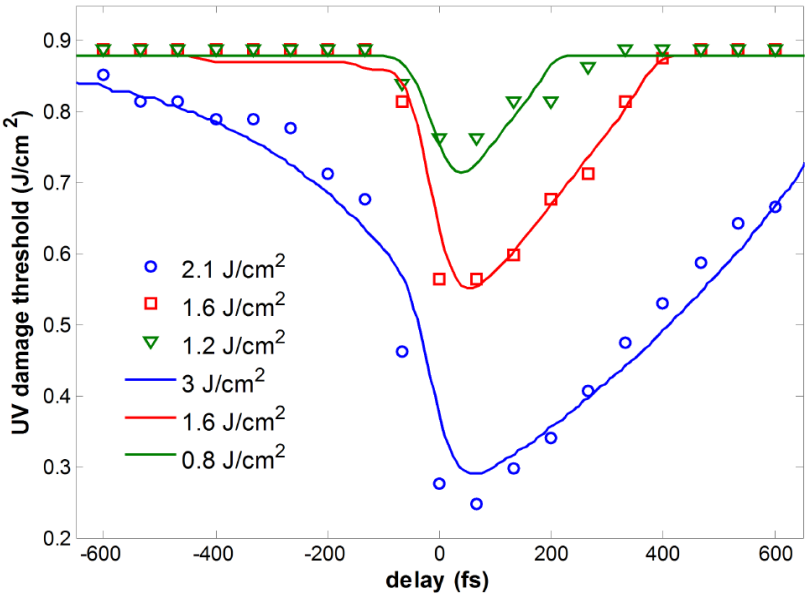

Figure 4.2 Dependence of UV damage threshold on the time delay at different NIR fluences. Dots: experimental data. Curves: simulation data. α_{UV}=2 cm^2/J, α_{NIR}=0.9 cm^2/J, $t_{p,UV}$=70 fs, $t_{p,NIR}$=60 fs, τ=250 fs, n_{critical}=1.7×10^{21} /cm^3

Figure 4.2 shows the dependence of the UV damage threshold on time delay between the UV and NIR pulses for different NIR fluences. Positive values in delay means UV pulses are irradiated on sample surfaces before NIR pulses. At the highest NIR fluence, the UV damage threshold reaches a minimum of 0.25 J/cm^2 at 60 fs delay, which is 71% lower than that in the normal case (damage threshold by UV alone). Actually, it is found that if NIR fluence is kept 2% below its damage threshold, the lowest fluence needed at zero delay for UV is 88% lower than that in the normal case. Away from this "optimal" delay, UV damage threshold increases, however, in an asymmetric manner: It returns to the normal value faster from the negative delay side than from

the positive delay side. With NIR fluence decreasing, more UV energy is required to damage the sample, i.e., the "effective" damage threshold increases.

In ultrafast laser ablation of dielectric materials, it is well known that multiphoton and avalanche ionization play a key role. In multiphoton ionization, UV pulses are more efficient in generating free electrons than NIR pulses. Specifically, for fused silica (with a bandgap of 9 eV), only 2 photons are needed for 266 nm (UV) light to generate an electron from valance band to conduction band, while for 800 nm (NIR) light, this number is 6, resulting a much higher cross section for UV. After this ionization process, these free electrons will be self-trapped to form excitons (STEs) in ~150 fs, which have a life time of 30-300 ps [12, 17]. It is suggested that these STEs generated by a pre-pulse can be again excited to become free electrons [12]. Damage forms when free electron density reaches the critical density value (~10^{21} /cm^3).

In Figure 4.2, for every NIR fluence, the UV threshold reaches a minimum value at ~60 fs and increases faster in the negative delay direction than in the positive delay direction. The number of free electron density reaches the maximum at the end of the 60 fs UV pulse because the lifetime of the electrons are much longer than the laser pulse duration, therefore the minimum UV fluence is required at the 60 fs delay. Because UV is more sufficient in generating seed electrons, the asymmetric shape is seen at each NIR fluence. It is noted that UV damage threshold is higher at zero delay. This is probably because the free electrons need some time to build up, and the maximum number is reached after the UV pulse. Another feature seen from this figure is the dependence of UV threshold on NIR fluence. A higher NIR fluence provides more avalanche ionization and can re-excite more free electrons from STEs [12], and therefore, a lower UV threshold is observed. It is found that with a high NIR fluence (2.1 J/cm^2), the UV damage

threshold returns to its normal value at ~27.3 ps, which is similar to the lifetime of STEs in accordance with ref. [12].

A simple rate equation describing the evolution of free electron density is used to testify our assumption discussed above,

$$\frac{dn}{dt} = W_{PI}(I_{UV}) + \alpha_{UV} I_{UV} n + W_{PI}(I_{NIR}) + \alpha_{NIR} I_{NIR} n - \frac{n}{\tau}, \qquad (4.1)$$

where n is the free electron density, W_{PI} the multiphoton ionization rate calculated from the Keldysh theory [11], α_{UV} and α_{NIR} the avalanche ionization rates for UV and NIR pulses, τ the electron recombination time, and I_{UV} and I_{NIR} the intensity for UV and NIR pulses:

$$I = I_0 \exp(-4\ln 2 \frac{(t-t_d)^2}{t_p^2}), \qquad (4.2)$$

where I_0 is the peak intensity, t_d the delay between UV and NIR pulses, and t_p the pulse duration (FWHM). I_0 can be calculated from fluence and pulse duration, i.e., $I_0 = F/t_p$. This model has been widely used to investigate the interaction between femtosecond lasers and dielectrics [17, 20, 21]. The damage threshold is determined when the free electron density reaches the critical density (1.7×10^{21} /cm^3) [20, 22]. The simulation results are shown in Figure 4.2, which fits well to the experimental data. The difference of NIR fluence between experimental data and simulation is probably due to the Gaussian shape of the beam, which is not considered in the simulation. It should be noted that in this model, only multiphoton and avalanche ionization are considered, and the ionization term is found to be essential for a good fitting. This indicates that avalanche ionization plays a key role.

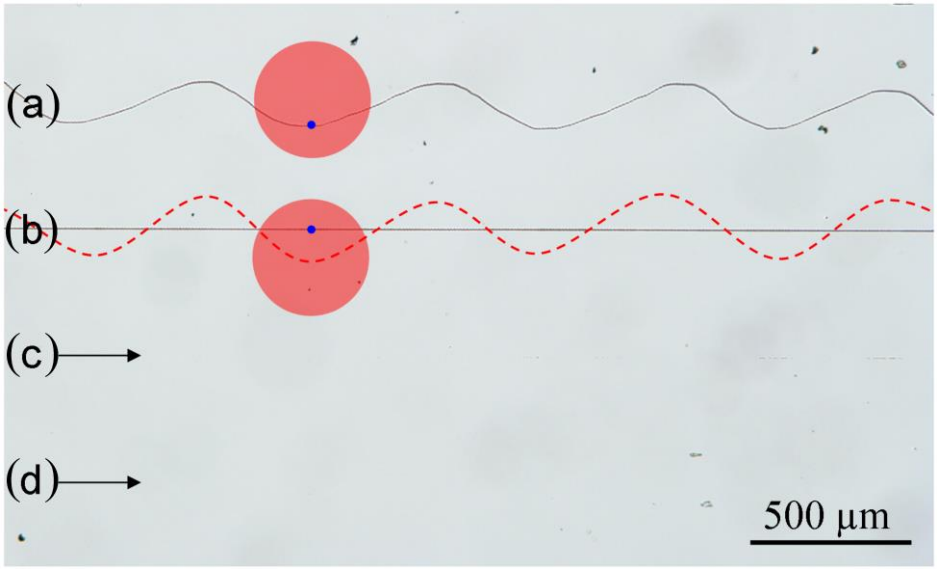

Figure 4.3 Optical images of different structures fabricated by a combination of UV and NIR pulses. (a) Moving UV spot while keeping NIR spot fixed. (b) Moving NIR spot while keeping UV spot fixed. No structure can be seen using either (c) UV or (d) NIR beam individually to write straight lines.

Since damage forms as a combined effect of UV and NIR pulses, the damage size is determined by the size of the area where the two beam overlap. In Figure 4.3(a), the NIR spot size is deliberately enlarged by moving its focus forward by 8.2 mm, resulting in a 330 µm diameter spot on the fused silica surface. The UV focus is fixed on the surface and in the central portion of the NIR spot. The sample moves towards left at a constant speed of 0.5 mm/s, and while moving, DM3 is tilted vertically back and forth while the NIR spot is kept fixed, and thus a wavy structure is written on the sample surface. On the contrary, in Figure 4.3(b), while keeping the UV spot fixed and tilting M2, the NIR spot is shifting vertically, and in contrast a straight line is written. The temporal delay difference by tilting those mirrors is calculated to be less than 1 fs. Since the seeding beam such as the UV or XUV can be focused to a spot much smaller than that of NIR, this paved way for machining features on scales that cannot be achieved with NIR beam alone.

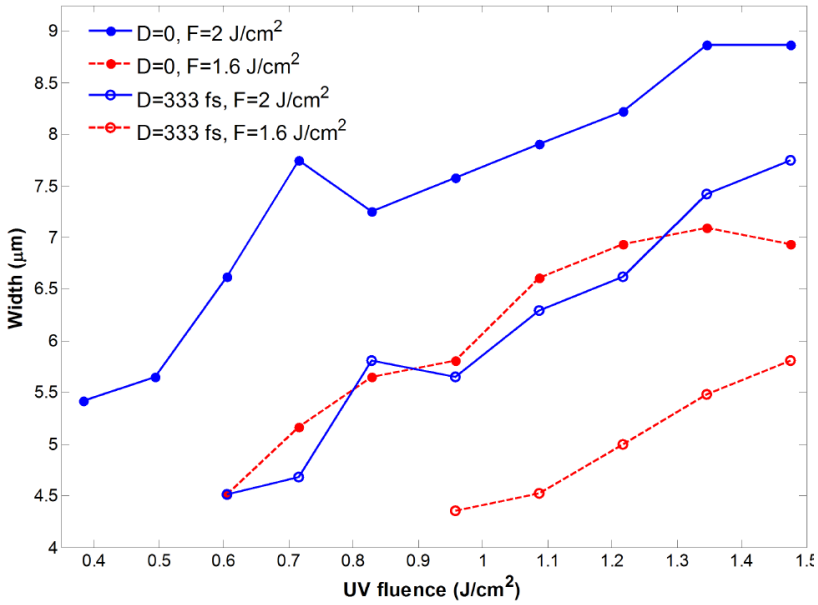

Figure 4.4 Relationship between linewidth and UV fluence at different delays (D) and NIR fluences (F).

Figure 4.4 shows the relationship between the average linewidth and UV fluence at different delays and NIR fluences. It can be seen that at each NIR fluence, the linewidth increases as UV fluence increases. This is due to the Gaussian shape of the focal spot. At each UV fluence, the linewidth is larger at zero delay and higher NIR fluence, and is smaller at 333 fs delay and lower NIR fluence. It is also noted that similar linewidth may be achieved with either zero delay and low NIR fluence, or 333 fs delay and high NIR fluence. The narrowest, continuous linewidth we can achieve from a single UV beam is 4.7 μm, which is similar to the narrowest linewidth with the two-pulse configuration.

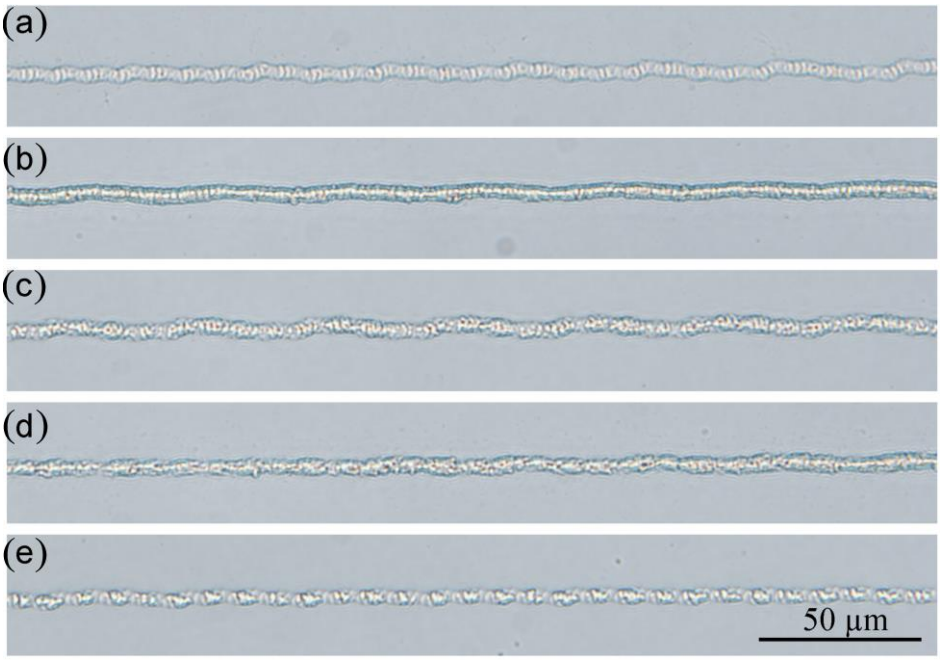

Figure 4.5 Optical images of lines with similar widths written by (a) UV beam only, (b) UV with 2 J/cm^2 NIR at zero delay, (c) UV with 1.6 J/cm^2 NIR at zero delay, (d) UV with 2 J/cm^2 NIR at 333 fs delay, and (e) UV with 1.6 J/cm^2 NIR at 333 fs delay. UV fluence: (a) 1.6 J/cm^2, (b) 0.33 J/cm^2, (c, d) 0.61 J/cm^2, and (e) 1.2 J/cm^2.

The fact that similar linewidth can be achieved by controlling the multiphoton and avalanche ionization is manifested in Figure 4.5. Linewidth close to that by UV only (Figure 4.5 (a)) is demonstrated under four sets of different conditions when UV and NIR pulses are combined. Another interesting feature is that, with the combination of UV and NIR pulses at different delays, line quality differs. Figure 4.5(a) shows a line written by a single UV beam with an average width of 4.7 µm. Due to the motion error of the XYZ stage and fluctuation of laser power, rough edges and small vertical grooves with an interval of 2 µm can be seen. These grooves are caused by successive pulses with the repetition rate of 1 kHz on a moving sample with the speed of 2 mm/s. With the combination of UV and high fluence NIR pulses at zero delay (Figure 4.5(b)), the edges become smoother and those vertical grooves disappear. The mechanism of these smooth lines is

unknown. One possible reason is the re-modification by the NIR beam, especially when the NIR fluence is high.

4. Conclusion

In summary, we have studied experimentally the micromachining of fused silica by a combination of UV and NIR pulses. With the help of NIR pulses at the fluence close to its damage threshold, the damage threshold of UV pulses can be lowered by 88% at ~60 fs delay. Moving away from this optimal delay, UV damage threshold approaches its single beam threshold. It is demonstrated that the damage caused by this two-beam configuration has similar feature size as that produced by a single UV beam, and the line quality can be controlled by the degree of seed injection by UV multiphoton absorption and the subsequent NIR avalanche ionization. Using this approach, nanoscale machining is possible by replacing the UV beam with XUV beams generated by HHG with the fluence well below its single beam damage threshold.

Acknowledgements

This work is funded by the Army Research Office.

References

[1] B.N. Chichkov, C. Momma, S. Nolte, F. von Alvensleben, and A. Tünnermann, Femtosecond, picosecond and nanosecond laser ablation of solids, Appl Phys A 63, 109 (1996).

[2] R.R. Gattass and E. Mazur, Femtosecond laser micromachining in transparent materials, Nature Photon. 2, 219 (2008).

[3] F. He, Y. Cheng, Z.Z. Xu, Y. Liao, J. Xu, H.Y. Sun, C. Wang, Z.H. Zhou, K. Sugioka, K. Midorikawa, Y.H. Xu, and X.F. Chen, Direct fabrication of homogeneous microfluidic channels embedded in fused silica using a femtosecond laser, Opt. Lett. 35, 282 (2010).

[4] C.B. Schaffer, A. Brodeur, J.F. Garcia, and E. Mazur, Micromachining bulk glass by use of femtosecond laser pulses with nanojoule energy, Opt. Lett. 26, 93 (2001).

[5] H. Varel, D. Ashkenasi, A. Rosenfeld, M. Wahmer, and E.E.B. Campbell, Micromachining of quartz with ultrashort laser pulses, Appl Phys A 65, 367 (1997).

[6] A. Joglekar, H. Liu, E. Meyhofer, G. Mourou, and A. Hunt, Optics at critical intensity: Applications to nanomorphing, Proc. Natl. Acad. Sci. USA 101, 5856 (2004).

[7] S. Nolte, B.N. Chichkov, H. Welling, Y. Shani, K. Lieberman, and H. Terkel, Nanostructuring with spatially localized femtosecond laser pulses, Opt. Lett. 24, 914 (1999).

[8] S.I. Kudryashov, G. Mourou, A. Joglekar, J.F. Herbstman, and A.J. Hunt, Nanochannels fabricated by high-intensity femtosecond laser pulses on dielectric surfaces, Appl. Phys. Lett. 91, 141111 (2007).

[9] Y.V. White, X. Li, Z. Sikorski, L.M. Davis, and W. Hofmeister, Single-pulse ultrafast-laser machining of high aspect nano-holes at the surface of SiO2, Opt. Express 16, 14411 (2008).

[10] P.B. Corkum, Plasma perspective on strong field multiphoton ionization, Phys. Rev. Lett. 71, 1994 (1993).

[11] L.V. Keldysh, Ionization in field of a strong electromagnetic wave, Sov. Phys. JETP 20, 1307 (1965).

[12] D. Grojo, M. Gertsvolf, S. Lei, T. Barillot, D.M. Rayner, and P.B. Corkum, Exciton-seeded multiphoton ionization in bulk SiO(2), Phys. Rev. B 81, 212301 (2010).

[13] T. Mocek, J. Polan, P. Homer, K. Jakubczak, B. Rus, I.J. Kim, C.M. Kim, G.H. Lee, C.H. Nam, V. Hajkova, J. Chalupsky, and L. Juha, Surface modification of organic polymer by dual action of extreme ultraviolet/visible-near infrared ultrashort pulses, J. Appl. Phys. 105, 026105 (2009).

[14] J.J. Rocca, V. Shlyaptsev, F.G. Tomasel, O.D. Cortazar, D. Hartshorn, and J.L.A. Chilla, Demonstration of a discharge pumped table-top soft-x-ray laser, Phys. Rev. Lett. 73, 2192 (1994).

[15] T.Y. Choi, D.J. Hwang, and C.P. Grigoropoulos, Femtosecond laser induced ablation of crystalline silicon upon double beam irradiation, Appl. Surf. Sci. 197–198, 720 (2002).

[16] I.H. Chowdhury, X. Xu, and A.M. Weiner, Ultrafast two-color ablation of fused silica, Appl Phys A 83, 49 (2006).

[17] M. Li, S. Menon, J.P. Nibarger, and G.N. Gibson, Ultrafast Electron Dynamics in Femtosecond Optical Breakdown of Dielectrics, Phys. Rev. Lett. 82, 2394 (1999).

[18] K. Sugioka, S. Wada, H. Tashiro, K. Toyoda, Y. Ohnuma, and A. Nakamura, Multiwavelength excitation by vacuum-ultraviolet beams coupled with fourth harmonics of a Q-switched Nd:YAG laser for high-quality ablation of fused quartz, Appl. Phys. Lett. 67, 2789 (1995).

[19] K. Obata, K. Sugioka, T. Akane, N. Aoki, K. Toyoda, and K. Midorikawa, Influence of laser fluence and irradiation timing of F2 laser on ablation properties of fused silica in F2-KrF excimer laser multi-wavelength excitation process, Appl. Phys. A 73, 755 (2001).

[20] B.C. Stuart, M.D. Feit, S. Herman, A.M. Rubenchik, B.W. Shore, and M.D. Perry, Nanosecond-to-femtosecond laser-induced breakdown in dielectrics, Phys. Rev. B 53, 1749 (1996).

[21] M. Lenzner, Kr, uuml, J. ger, S. Sartania, Z. Cheng, C. Spielmann, G. Mourou, W. Kautek, and F. Krausz, Femtosecond Optical Breakdown in Dielectrics, Phys. Rev. Lett. 80, 4076 (1998).

[22] L. Jiang and H. Tsai, Energy transport and material removal in wide bandgap materials by a femtosecond laser pulse, Int. J. Heat Mass Transfer 48, 487 (2005).

Chapter 5 - Femtosecond Laser Nanomachining Initiated by Ultraviolet Multiphoton Ionization

In this chapter we apply the UV-IR machining method to fabricate nano-scale features. This work was published in the paper "Femtosecond laser nanomachining initiated by ultraviolet multiphoton ionization", X. Yu, Q. Bian, Z. Chang, P.B. Corkum, and S. Lei, Opt. Express **21**, 24185 (2013).

Abstract

We report on the experimental results of 300 nm features generated on fused silica using a near-infrared (IR) femtosecond laser pulse initiated by an ultraviolet (UV) pulse. With both pulses at a short (~60 fs) delay, the damage threshold of the UV pulse is only 10% of its normal value. Considerable reduction of UV damage threshold is observed when two pulses are at ±1.3 ps delay. The damage feature size of the combined pulses is similar to that of a single UV pulse. A modified rate equation model with the consideration of defect states is used to help explain these results. This concept can be applied to shorter wavelengths, e.g. XUV and X-ray, with the required fluence below their normal threshold.

1. Introduction

Direct fabrication of nanoscale structures in at least one dimension is of significant importance for miniaturization and integration. Although photolithography is commonly used in industry and structures of several tens of nanometers can be achieved, single-step nanomachining methods are still desired. Ultrafast lasers are a promising tool for nanomachining due to the unique properties such as reduced thermal effects and the potential for direct 3-dimensional fabrication

[1-3]. Waveguides, microfluidic devices, opto-electronic systems have been successfully fabricated using femtosecond lasers [4].

Generally speaking, there are two approaches to direct laser nanomachining. One is to use a single laser beam and focus it down to sub-micrometer scale using high numerical aperture focusing optics. Due to the nonlinear interaction between ultrafast laser pulses and wide bandgap dielectric materials, further reduction of damage size is possible by setting the pulse energy such that only the center part of the focused beam is above the damage threshold. By this means, small features with dimension of ~40 nm are achieved with 800 nm wavelength pulses [5,6]. However, this method requires a very high degree of laser power stability and thus is not practical for industrial applications. Due to diffraction limit of all focused laser beams, the minimal focal spot size is of the order of λ/NA, where λ is laser wavelength and NA is the numerical aperture of focusing optics. One way to reduce focal size is using high NA microscope objectives. By using high NA objectives, structures with the size of ~130 nm and 200 nm are achieved on the surface of fused silica [7] and PMMA [8], respectively. Alternatively, by using short wavelength laser beams, such as UV lasers with wavelength of 200-400 nm and proper focusing, structures of 250 nm on fused silica [9] and 600 nm on stainless steel foils [10] are achieved.

The other approach is to use multiple laser beams and usually the interference between these beams are utilized, e.g., laser-induced periodic surface structures (LIPSS) [11], which is beyond the scope of our research.

As mentioned above, one effective way to reduce focal spot size is to use short wavelength beams, such as XUV and X-ray, generated from high harmonic generation (HHG). However, due to the low conversion efficiency of HHG, direct machining of dielectrics using HHG remains a challenge. Our recent results show that with the help of a long wavelength IR beam, the damage

threshold of 267 nm beam is lowed by 88% [12]. This provides a pathway to XUV or even shorter wavelength laser nanomachining with energy below the damage threshold.

In this paper, we present a novel approach for laser direct fabrication of nanostructures in which 267 nm femtosecond laser pulses are used to produce seed electrons with subsequent damage induced by IR pulses. The significance of this approach is its potential downward scalability in feature size with shorter and shorter wavelengths down to sub 10 nm.

2. Experimental

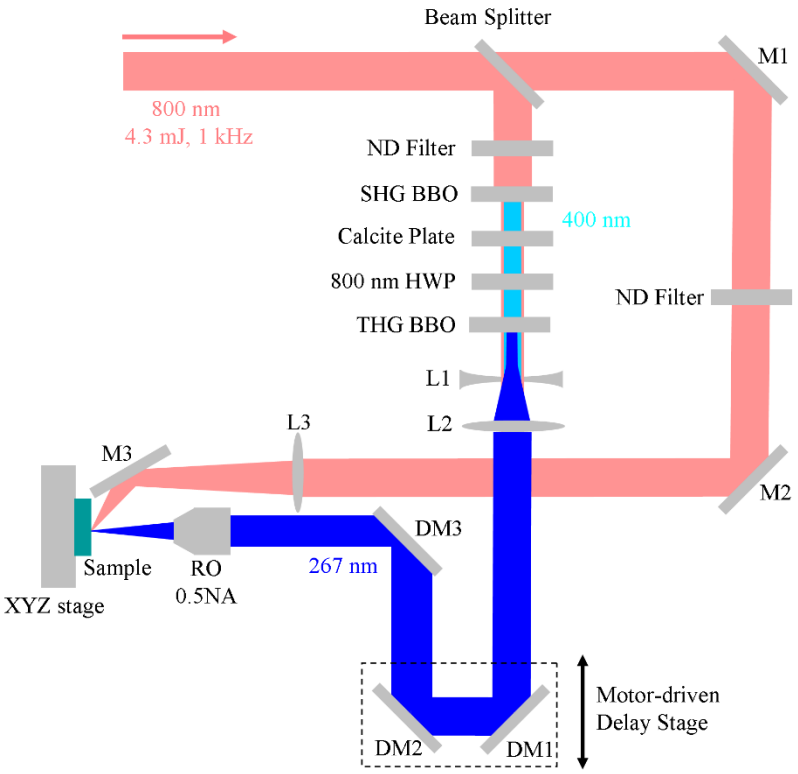

Figure 5.1 Experiment setup. ND: neutral density. SHG: second harmonic generation. BBO: barium borate. HWP: half-wave plate. THG: third harmonic generation. Focal length: L1=-25 mm, L2=100 mm, L3=200 mm. M1-M3: 800 nm dielectric mirrors. DM1-DM3: dichroic mirrors. RO: reflecting objective.

The experimental setup is shown in Figure 5.1. A Ti:Sapphire femtosecond (fs) laser system delivers ~60 fs (full-width-at-half-maximum, FWHM) pulses at the center wavelength of 800 nm with repetition rate of 1 kHz and maximum pulse energy of 4.3 mJ. This fundamental beam is split into two arms. The beam in one arm (UV arm) propagates through a third harmonic generation (THG) module (Eksma Optics) and third harmonic pulses at the center wavelength of 267 nm and pulse energy of 20 μJ are generated. The pulse duration (FWHM) is estimated to be 70 fs [12]. This beam is expanded by a 4× reversed telescope (consisting of L1 and L2) and then focused on the front surface of fused silica glass (Corning 7980) with a reflective objective lens (Edmund) with a numerical aperture (NA) of 0.5. Three dichroic mirrors (DM1-3) are used to selectively reflect only the 267 nm pulses. The other arm (IR) is focused by a plano-convex lens with the focal length of 200 mm, and is overlapped with the UV focal spot with an angle of 60º. The focal spot of the IR arm is deliberately placed after the sample to increase the spot size on the sample, and the focal spot size of IR beam at the silica surface is ~10 μm. These two arms are spatially overlapped by monitoring the two beam spots on the front surface of the sample using a CCD camera. For temporal overlapping, it is based on the results in the previous study [12], where with fixed IR fluence, the lowest UV threshold is found to correspond to a ~60 fs delay between the UV and IR pulse. Due to experimental limitation, zero delay is not determined experimentally in this study. Therefore, UV damage threshold is measured at different time delays with fixed IR fluence, and the minimum UV damage threshold thus determined is assigned a 60 fs delay based on Ref. [12]. It should be noted that an uncertainty of about ± 100 fs exists because of the step resolution of the translation stage, which however does not affect the conclusions of this work. The XYZ stage is moving at a constant speed of 50 mm/s, resulting in a 50 μm separation between the laser shots. This ensures that each pulse irradiates at a fresh site on the sample.

3. Results and discussion

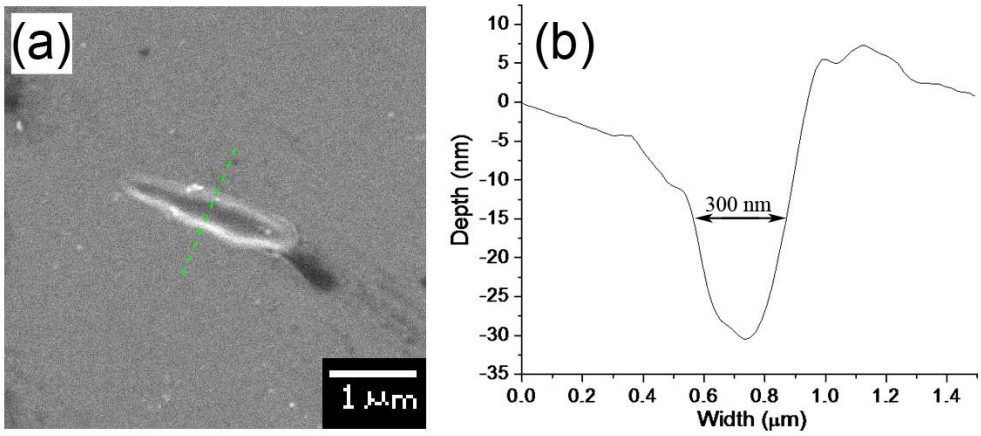

Figure 5.2 (a) SEM image of a damage spot caused by single UV beam. (b) Cross section along the dashed line in (a). The pulse energy is 64 nJ.

First we examine the damage caused by a single UV beam. Figure 5.2 shows a damage spot caused by the single UV beam with pulse energy of 64 nJ. The damage is a line shape instead of a round one, which is attributed to the following two factors. First, the beam quality is not good enough, especially the outer portion of the beam that the reflecting objective lens uses to focus. This has been experimentally verified with a separate experiment (results not shown here). Second, the beam profile of the THG beam is not round. Right after the THG BBO, the beam size ($1/e^2$) is 2.9 mm (horizontal) and 3.9 mm (vertical) measured by the knife-edge method assuming a Gaussian profile. Due to the nonlinearity of the interaction between the laser pulse and the sample, the resulting damage becomes more elliptical. To obtain a 300 nm circular damage spot, we suggest to use a UV transmitting objective to fully utilize the central portion of the beam. In addition, a pair of cylindrical lenses (a concave and a convex lens) can be inserted after the THG BBO to correct the asymmetric profile, and spatial filtering can also be used to improve the beam quality. The cross section along the narrow direction of Figure 5.2(a) is shown in Figure 5.2(b). The FWHM width is measured to be 300 nm. To the best of our knowledge, it's the first time

features of 300 nm resolution have been directly written on the surface of a dielectric, although periodic structures with period of 250 nm has been reported [9].

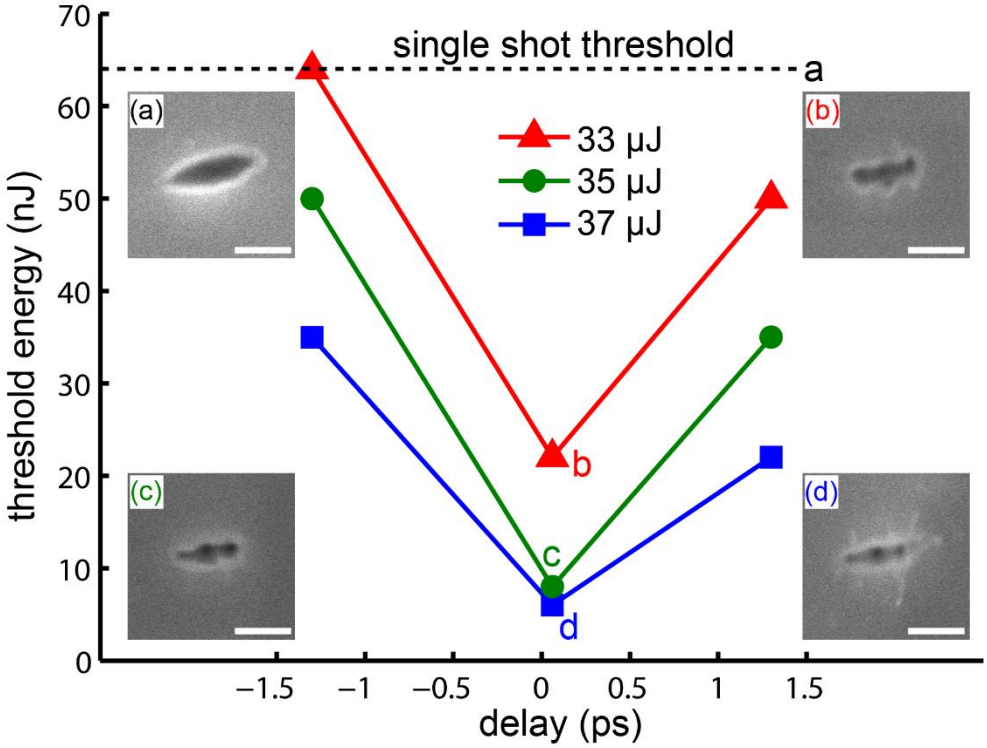

Figure 5.3 Relationship between threshold energy and delay of UV and IR pulses. Insets: SEM images of each point indicated by a, b, c and d. Scale bars are 1 μm. Black dashed line indicates UV single beam threshold. The solid lines are guides to the eye.

With the combination of UV and IR beams, the damage threshold of UV beam can be lowered by ~90%, as shown in Figure 5.3. Three IR energy levels (33 μJ, 35 μJ, 37 μJ) and three delays (-1.3 ps, 60 fs, 1.3 ps) are used. Positive delays are defined as when the UV pulse reaches the sample before the IR pulse. In the experiments, different UV energy is used and the damage threshold is determined as the lowest energy with which nanoscale damage is observed using SEM. No damage is seen using only the IR beam. As can be seen in Figure 5.3, at 60 fs delay and 37 μJ IR energy, UV damage threshold is ~10% of the normal value, and it increases with longer delays and with lower IR energy. This feature is observed in our recent experiments [12]. In contrast to

the multiple shot threshold, this time we used single shot threshold measurement to avoid incubation effects. It should be noted that at 60 fs delay, the damage threshold using IR energy of 37 μJ and 35 μJ is similar. This is because 6 nJ is the lowest energy level that can be measured accurately due to background noise. Therefore, the actual damage threshold using IR energy of 37 μJ may be lower than 6 nJ. The insets show SEM images of the points indicated by the corresponding letters. As can be seen, the feature size is similar for different cases, which suggests that this technique can be used for nanomachining with an XUV (or shorter wavelength) beam combined with a longer wavelength beam, and the resulting feature size is only determined by the XUV beam. It should be noted that with the combination of two beams, there is an increase of edge roughness in morphology (Figure 5.3(b)-(d)) compared to the damage caused by single UV beam (Figure 5.3(a)), which may be caused by the energy fluctuation of the UV beam, especially when the pulse energy is low.

A simple rate equation has been popularly used to model the electron density in order to get the damage threshold [13-15]. It calculates the evolution of free electron density with respect to time, and it is assumed that damage occurs when the electron density reaches a critical value. It is found that the lifetime of these generated electrons is 60~150 fs [14,16,17]. In our experiments, however, we observe significant reduction (~50%) of the damage threshold at long delays (±1.3 ps), which suggests that the free electrons generated by the UV pulse are trapped in defect states and then are re-ionized easily by the IR pulse, and these defect states have a lifetime on the order of 1 ps [18].

The modified rate equation model with consideration of defect states is:

$$\frac{dn_e}{dt} = W_{MPI}(I) + \alpha I n_e + \sigma_j I^j n_d - \frac{n_e}{\tau_e}$$
$$\frac{dn_d}{dt} = \frac{n_e}{\tau_e} - \sigma_j I^j n_d - \frac{n_d}{\tau_d} \qquad (5.1)$$

where n_e is free electron density, W_{MPI} is the Keldysh multi-photon ionization rate, I is laser intensity, α and σ are the ionization cross section of avalanche electrons and defect states, respectively, τ_e and τ_d are decay time of free electrons and defect states, respectively, and n_d is defect state density. We use j=1 and 2 for UV and IR beams respectively [15]. Both UV and IR pulses have a Gaussian shape in time and the pulse duration (FWHM) is 70 fs and 60 fs, respectively. In our model, free electrons are first generated by photo-ionization (calculated by the Keldysh theory) and the electron density is further increased by avalanche ionization within the pulse duration. The decay time of these electrons is 150 fs and all of them are assumed to decay into defect states which have a bandgap of 3.2 eV. It should be noted that in this model the defect states have a single band lying in between the conduction band and exciton band [15]. The second pulse re-ionizes the defect states to free electrons, and both photo and avalanche ionization are also considered. Damage occurs when free electron density reaches 1.7×10^{21} cm^{-3} (critical density at 800 nm wavelength).

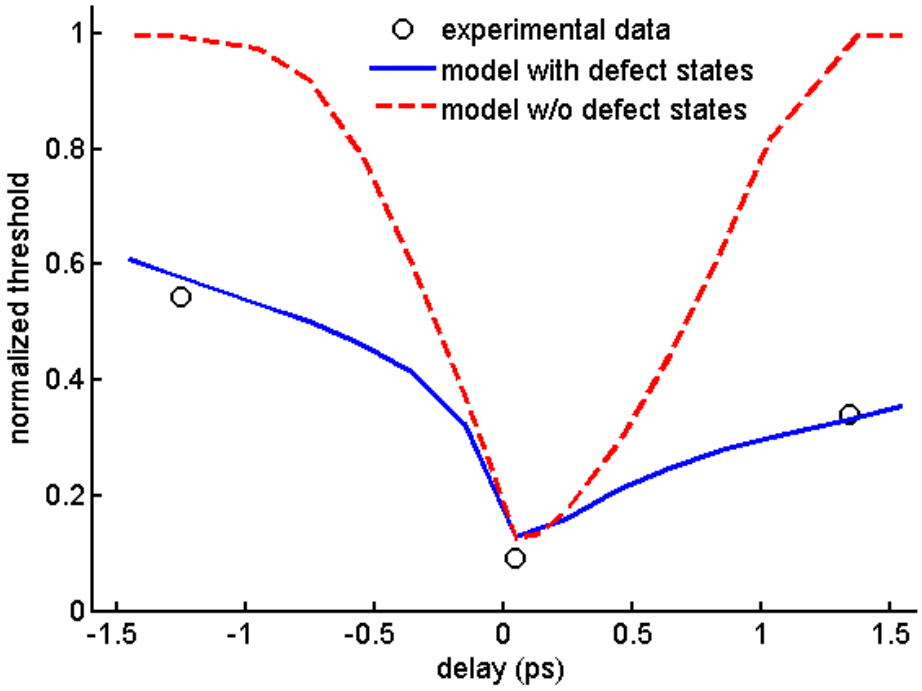

Figure 5.4 Comparison of numerical calculation of damage threshold with and without defect states at different delays. Dots are experimental results from Figure 5.3 (37 μJ). α_2= 20 cm^2/J, α_6= 4 cm^2/J, σ_1=2×10^{-3} (W/m^2)s^{-1}, σ_2=1.1×10^{-21} (W/m^2)^{2}s^{-1}, τ_e=150 fs, τ_d=1 ps, pulse duration (FWHM): 70 fs for UV and 60 fs for IR.

The modeling results and experimental data (37 μJ, Figure 5.3) are shown in Figure 5.4, and for comparison, modeling results using the same parameters without the defect states term is also shown. As can be seen, our model agrees with the experimental data well with the defect states term considered, and the lifetime of defect states is found to be ~ 1 ps, which is similar to recent results [18]. Without defect states, the damage threshold will return to its normal value at much shorter delays because the electrons have a shorter lifetime.

4. Conclusion

Using a high NA objective to focus a UV femtosecond laser beam, nanostructures with dimension of 300 nm are fabricated on the surface of fused silica. The damage threshold of the UV beam can be reduced by ~ 90% with the combination of an IR beam at short (~60 fs) delay.

The required seeding pulse energy can already be reached in the XUV wavelength range by high harmonic generation [19]. Significant UV threshold reduction at ±1.3 ps indicates that defect states, which have a longer lifetime compared to free electrons, should be taken into account. Our modified rate equation model confirms the role of defect states.

Acknowledgments

Xiaoming Yu, Qiumei Bian and Shuting Lei acknowledge the support from the National Science Foundation.

Zenghu Chang acknowledges the support from the US Army Research Office.

References

[1] B.N. Chichkov, C. Momma, S. Nolte, F. von Alvensleben, and A. Tünnermann, Femtosecond, picosecond and nanosecond laser ablation of solids, Appl Phys A 63, 109 (1996).

[2] R.R. Gattass and E. Mazur, Femtosecond laser micromachining in transparent materials, Nature Photon. 2, 219 (2008).

[3] M. Ali, T. Wagner, M. Shakoor, and P.A. Molian, Review of laser nanomachining, J. Laser Appl. 20, 169-184 (2008).

[4] R. Osellame, H.J.W.M. Hoekstra, G. Cerullo, and M. Pollnau, Femtosecond laser microstructuring: an enabling tool for optofluidic lab-on-chips, Laser Photon. Rev. 5, 442-463 (2011).

[5] A. Joglekar, H. Liu, E. Meyhofer, G. Mourou, and A. Hunt, Optics at critical intensity: Applications to nanomorphing, Proc. Natl. Acad. Sci. USA 101, 5856 (2004).

[6] Y. Liao, Y. Shen, L. Qiao, D. Chen, Y. Cheng, K. Sugioka, and K. Midorikawa, Femtosecond laser nanostructuring in porous glass with sub-50 nm feature sizes, Opt. Lett. 38, 187-189 (2013).

[7] S.I. Kudryashov, G. Mourou, A. Joglekar, J.F. Herbstman, and A.J. Hunt, Nanochannels fabricated by high-intensity femtosecond laser pulses on dielectric surfaces, Appl. Phys. Lett. 91, 141111 (2007).

[8] J.M. Fernández-Pradas, C. Florian, F. Caballero-Lucas, J.L. Morenza, and P. Serra, Femtosecond laser ablation of polymethyl-methacrylate with high focusing control, Applied Surface Science.

[9] D.N. Nikogosyan, M. Dubov, H. Schmitz, V. Mezentsev, I. Bennion, P. Bolger, and A.V. Zayats, Point-by-point inscription of 250-nm-period structure in bulk fused silica by tightly-focused femtosecond UV pulses: experiment and numerical modeling, Central European Journal of Physics 8, 169-177 (2009).

[10] J. Békési, J.H. Klein-Wiele, and P. Simon, Efficient submicron processing of metals with femtosecond UV pulses, Applied Physics A 76, 355-357 (2003).

[11] J. Bonse, J. Kruger, S. Hohm, and A. Rosenfeld, Femtosecond laser-induced periodic surface structures, J. Laser Appl. 24, (2012).

[12] X. Yu, Q. Bian, B. Zhao, Z. Chang, P.B. Corkum, and S. Lei, Near-infrared femtosecond laser machining initiated by ultraviolet multiphoton ionization, Applied Physics Letters 102, 101111-101114 (2013).

[13] B.C. Stuart, M.D. Feit, S. Herman, A.M. Rubenchik, B.W. Shore, and M.D. Perry, Nanosecond-to-femtosecond laser-induced breakdown in dielectrics, Physical Review B 53, 1749 (1996).

[14] M. Li, S. Menon, J.P. Nibarger, and G.N. Gibson, Ultrafast Electron Dynamics in Femtosecond Optical Breakdown of Dielectrics, Phys. Rev. Lett., 2394 (1999).

[15] D. Grojo, M. Gertsvolf, S. Lei, T. Barillot, D.M. Rayner, and P.B. Corkum, Exciton-seeded multiphoton ionization in bulk SiO(2), Phys. Rev. B 81, 212301 (2010).

[16] P. Martin, S. Guizard, P. Daguzan, G. Petite, P. D'Oliveira, P. Meynadier, and M. Perdrix, Subpicosecond study of carrier trapping dynamics in wide-band-gap crystals, Physical Review B 55, 5799-5810 (1997).

[17] G.M. Petrov and J. Davis, Interaction of intense ultra-short laser pulses with dielectrics, Journal of Physics B: Atomic, Molecular and Optical Physics 41, 025601 (2008).

[18] J. Peng, D. Grojo, D.M. Rayner, and P.B. Corkum, Control of energy deposition in femtosecond laser dielectric interactions, Applied Physics Letters 102, 161105-161103 (2013).

[19] Y. Wu, E. Cunningham, H. Zang, J. Li, M. Chini, X. Wang, Y. Wang, K. Zhao, and Z. Chang, Generation of high-flux attosecond extreme ultraviolet continuum with a 10 TW laser, Applied Physics Letters 102, 201104-201104 (2013).

Chapter 6 - Fabricating Nanostructures on Fused Silica Using Femtosecond Infrared Pulses Combining with Sub-Nanojoule Ultraviolet Pulses

In this chapter damage shape is improved with a spatial filter, and with the assistance of the IR pulse, 500-nm craters are fabricated with UV pulse energy as low as 0.8 nJ. This work was published in "Fabricating nanostructures on fused silica using femtosecond infrared pulses combining with sub-nanojoule ultraviolet pulses", X. Yu, Z. Chang, P.B. Corkum, and S. Lei, Opt. Lett. **39**, 5638 (2014).

Abstract

Circular craters with diameters of 500 nm are fabricated on the surface of fused silica by femtosecond ultraviolet-infrared (UV-IR) pulse trains with 0.8 nJ UV pulse energy. UV damage thresholds at different IR energies and UV-IR delays are measured. Diameters and depths of the ablated craters can be modified by adding the IR pulse and varying the UV-IR delays. These results demonstrate the feasibility of nanomachining using short wavelength lasers with pulse energy far below normal damage thresholds.

1. Introduction

Femtosecond lasers have been used to fabricate various types of microstructures such as waveguides, microfluidic networks, and three-dimensional (3D) data storage devices [1–3]. However, with conventional femtosecond systems operating at infrared wavelengths, fabricating these structures at nanometer scales requires high numerical aperture (NA) optics [4,5], precise control of pulse energy [6], or additional material processing steps [7]. Alternatively, by focusing short wavelength beams, such as ultraviolet (UV) and soft x-ray beams, features with sizes ranging

from 80 to 600 nm have been fabricated [8–10]. While increasing energy output is still an ongoing research in generating short wavelength laser pulses, and indeed XUV pulses with 100 nJ have been reported [11], a machining technique requiring low pulse energies is still desired for practical applications, especially due to the low conversion efficiency in obtaining these beams. Our previous results show that by a combination of UV and IR beams, nano-scale features can be fabricated on fused silica with the UV pulse energy at only 10% of its normal value [12]. However, only line-shaped damage is achieved due to imperfect UV beam quality.

In this Letter, we apply a home-built spatial filter to improve the UV beam quality, and fabricate circular craters with diameters of 500 nm on the surface of fused silica, with the minimal UV pulse energy of 0.8 nJ using a UV-IR pulse train. These results demonstrate the feasibility of nanomachining using short wavelength lasers, even with their pulse energy far below normal damage thresholds.

2. Experimental

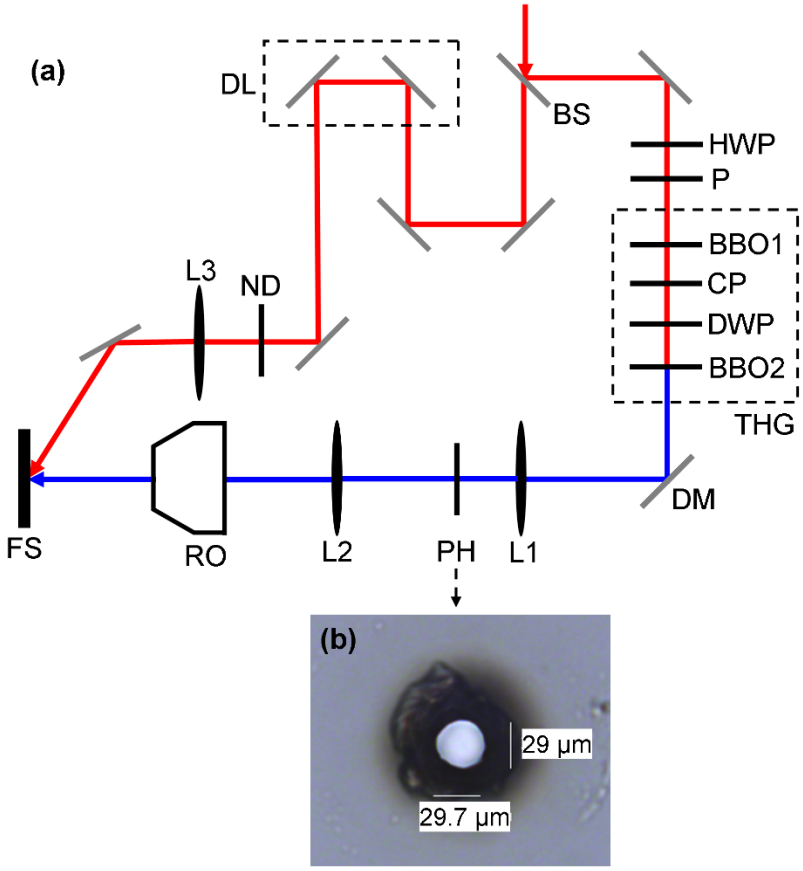

Figure 6.1 (a) Experimental setup. BS: beamsplitter. HWP: half-wave plate. P: polarizer. BBO: β-Barium borate. CP: calcite plate. DWP: 400/800 nm dual wave plate. THG: third harmonic generate kit. DM: dichroic mirror. L1-L3: plano-convex lenses. PH: pinhole. RO: reflecting objective. FS: fused silica sample. DL: delay line. ND: neutral density filter. (b) Optical image of a pinhole used in the experiments.

Figure 6.1 shows the experimental setup. Synchronized femtosecond UV (266 nm) and IR (800 nm) pulses are generated from the same Ti:Sapphire laser that operates at a repetition rate of 1 kHz and delivers 60 fs (full width at half maximum, FWHM) IR pulses. The UV beam (estimated pulse duration 70 fs FWHM), generated from third harmonic generation (THG) [13], first goes through a spatial filter which consists of two thin lenses (L1, f=500 mm and L2, f=1m), and a pinhole drilled through a borosilicate microscope cover glass (thickness 150 μm) by another IR

beam. The estimated UV pulse duration after L2 is 85 fs, due to dispersion of the two lenses. The diameter of the pinhole matches the calculated focal spot size of L1. Lenses L1 and L2 also form a 2× beam expander so that the filtered UV beam with a smooth Gaussian profile overfills the input aperture of the reflecting objective (RO, Edmund, 0.5 NA, working distance 23.2 mm). The UV beam is then focused by RO perpendicularly onto a fused silica sample (Corning 7980), with an estimated focal spot diameter of 0.64 μm. The sample is mounted on a motorized three-axis stage. The IR beam (60 fs FWHM) goes through a mechanical delay line and then is focused by L3 (f=200 mm) to the sample at a ~45º incidence angle. The IR spot size (observed from a CCD camera) is 20×15 μm^2 due to the oblique angle. The CCD camera monitoring the sample surface ensures that the UV spot remains at the center of the IR spot. The energy of the UV beam is controlled by a half-wave plate and a polarizer placed before the THG crystals, while the energy of the IR beam is controlled by a rotating neutral density (ND) filter. Both UV and IR energies are measured in front of the sample. The energy fluctuations of the UV and IR beams are within 5% and 1%, respectively. For temporal overlapping, multiple-shot UV damage threshold is measured at different delays (temporal step 60 fs) at a fixed IR pulse energy below its damage threshold and a slow sample moving speed of 0.4 mm/s, and the optimal delay (~60 fs) is determined when the lowest UV damage threshold is observed [13]. In the following single-shot measurements, the sample moves at a speed of 20 mm/s, ensuring that each UV-IR pulse pair irradiates at a fresh site. In all the cases no visual damage is seen with the IR beam alone.

3. Results and discussion

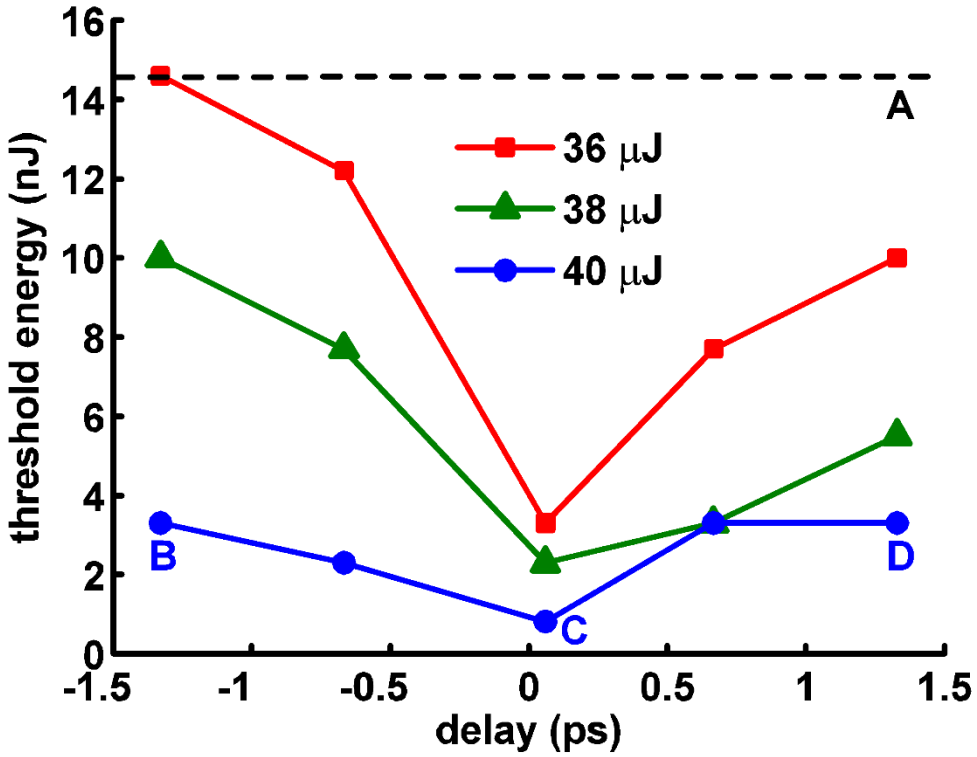

Figure 6.2 UV damage threshold energy measured at different IR energies and delays. The black dashed line (A) indicates UV only threshold. SEM images corresponding to conditions A-D are shown in Figure 6.3(a-d), respectively. Square, triangle and circular dots are experimental data. Solid lines are a guide to the eye.

At a certain delay and IR pulse energy, the single-shot UV damage threshold is determined as the lowest UV energy with which damage is observed using a scanning electron microscope (SEM). Twelve UV energies ranging from 0.4 to 19 nJ are used, and the results with five delays and three IR energies are shown in Figure 6.2. The UV pulses arrive at the sample surface before and after the IR pulses at positive and negative delays, respectively. Similar curves have been reported, and can be explained in terms of free electron generation and defect states formation [12]. Theoretically, in ultrafast laser ablation of dielectrics, damage is formed when free electron density reaches a critical density. At positive delays, free electrons are first generated by the UV

pulse through multiphoton ionization. These electrons either absorb energy from the following IR pulse at short delays (<300 fs) or first decay into self-trapped excitons and then are re-ionized by the IR pulse at long delays (>1 ps) [14]. The result in both cases is a rapid increase in free electron density due to avalanche ionization during the IR pulse duration, and eventually this density reaches the critical density, and damage is formed. With the help of the IR pulse, only a small number of free electrons (generated by the UV pulse) are needed to act as "seed electrons", and therefore the UV damage threshold is reduced. At negative delays, a similar process occurs except that the UV and IR pulses switch their roles.

The major difference of the results shown in Figure 6.2 from our previous results is reduced UV threshold energies, for both the UV only and the pulse train case. Specifically, the UV only threshold is reduced from 64 nJ to 14.6 nJ, and the lowest UV threshold when combined with an IR pulse is reduced from 6 nJ to 0.8 nJ. This reduction in threshold energy is attributed to the smaller focal spot and therefore smaller ablation area (shown below). Special attention is given to the case with 40 μJ IR energy, with which the UV damage threshold is reduced to 0.8 nJ, only 5.5% of the normal threshold value. To the best of our knowledge, it is the first time that such low energy is used in femtosecond ablation of dielectrics. It should be noted that, even with the improved UV beam, the damage threshold energy (14.6 nJ) is still ~5 times higher than estimated (2.8 nJ) for a focal diameter of 0.64 μm [15], perhaps due to a Bessel-like instead of a Gaussian profile of the UV focus (shown below in Figure 6.3) [16]. Therefore, nano-ablation with even lower pulse energy is possible by replacing the reflecting objective with a transmitting objective, which generates an Airy pattern with more energy concentrated in the central spot compared to the Bessel-like pattern. It is worth noting that, although Figure 6.2 emphasizes on the reduction of UV damage threshold, these data can also be interpreted as reduction of IR threshold with the help of

UV pulses. For example, Point B in Figure 6.2 indicates that, with 3.5 nJ UV pulse energy and -1.3 ps delay, the IR threshold is reduced from 42 μJ (IR only threshold) to 40 μJ.

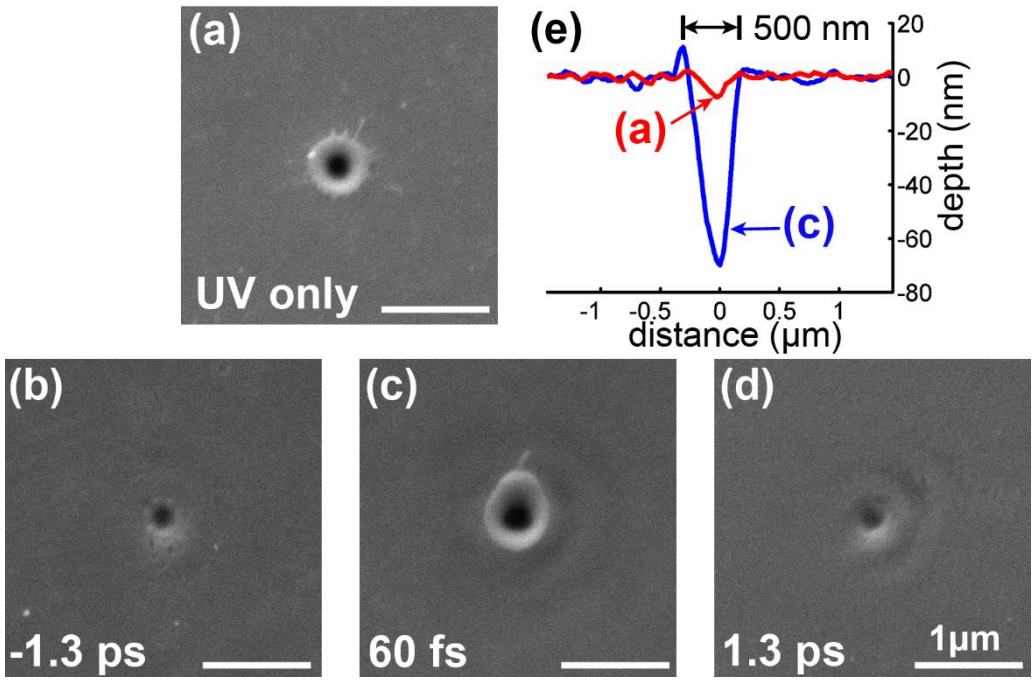

Figure 6.3 (a-d) SEM images of the damage spots with UV beam only, UV-IR pulse train at -1.3 ps, 60 fs, and 1.3 ps delay, respectively. (a-d) correspond to the conditions labeled A-D in Figure 6.2, respectively. (e) Typical cross-sections of the damage in (a) and (c) measured with an atomic force microscope (AFM).

Figure 6.3(a-d) shows SEM images of the damage spots corresponding to A-D in Figure 6.2, respectively, and typical cross-sections for Figure 6.3(a) and (c) are shown in Figure 6.3(e). Craters with circular shapes are achieved with the aforementioned beam-shaping technique for both UV only [Figure 6.3(a)] and the pulse train case [Figure 6.3(b-d)]. An increase in crater depth is observed: from 7 nm with the UV beam alone [Figure 6.3(a)] to 70 nm with the UV-IR pulse train at a 60 fs delay [Figure 6.3(c)], while the damage size on the surface remains similar. Besides, Figure 6.3(b) and (d) also show that craters fabricated with a pulse train tend to be smaller at longer delays. Although these two effects, namely the increase in ablation depth with pulse trains and the

reduction in feature size at long delays, have been reported [17,18], to the best of our knowledge, it is the first time to show these effects in nanomachining, and thus it indicates the possibility of controlling the size of fabricated nanostructures through pulse delays. The ripple structures adjacent to the central craters in Figure 6.3(c) and (d) are attributed to the Bessel-like profile of the UV focus [16]. Combining with the IR beam enhances ablation effects and therefore reveals the otherwise unseen structures with the UV beam only [Figure 6.3(a)]. These structures can be removed when a transmitting objective lens is used (see the paragraph above).

4. Conclusion

In summary, through the fabricated 500 nm features on fused silica by UV-IR pulse trains with 0.8 nJ UV pulse energy, we demonstrate the feasibility of nanomachining using even shorter wavelength (XUV, X-ray) lasers with pulse energies far below the normal damage threshold. The addition of long wavelength pulses can improve ablation rates, and resultant damage shapes can be further controlled by changing the delays of the pulse trains.

Acknowledgements

The authors thank Prof. Daniel A. Higgins, Prof. Jun Li, Hao Xu and Yiqun Yang for their assistance in AFM imaging. This material is based on work supported by the Army Research Office and the National Science Foundation under Grant Number CMMI 1131627.

References

[1] R.R. Gattass and E. Mazur, "Femtosecond laser micromachining in transparent materials," Nat. Photonics **2**, 219 (2008).

[2] K. Sugioka and Y. Cheng, "Ultrafast lasers—reliable tools for advanced materials processing," Light Sci. Appl. **3**, e149 (2014).

[3] M.H. Hong, B. Luk'yanchuk, S.M. Huang, T.S. Ong, L.H. Van, and T.C. Chong, "Femtosecond laser application for high capacity optical data storage," Appl. Phys. A **79**, 791 (2004).

[4] S.I. Kudryashov, G. Mourou, A. Joglekar, J.F. Herbstman, and A.J. Hunt, "Nanochannels fabricated by high-intensity femtosecond laser pulses on dielectric surfaces," Appl. Phys. Lett. **91**, 141111 (2007).

[5] J.M. Fernández-Pradas, C. Florian, F. Caballero-Lucas, J.L. Morenza, and P. Serra, "Femtosecond laser ablation of polymethyl-methacrylate with high focusing control," Appl. Surf. Sci. **278**, 185 (2013).

[6] A.P. Joglekar, H.-H. Liu, E. Meyhöfer, G. Mourou, and A.J. Hunt, "Optics at critical intensity: Applications to nanomorphing," Proc. Natl. Acad. Sci. U.S.A. **101**, 5856 (2004).

[7] Y. Liao, Y. Shen, L. Qiao, D. Chen, Y. Cheng, K. Sugioka, and K. Midorikawa, "Femtosecond laser nanostructuring in porous glass with sub-50 nm feature sizes," Opt. Lett. **38**, 187 (2013).

[8] J. Békési, J.-H. Klein-Wiele, and P. Simon, "Efficient submicron processing of metals with femtosecond UV pulses," Appl. Phys. A **76**, 355 (2003).

[9] G. Vaschenko, A.G. Etxarri, C.S. Menoni, J.J. Rocca, O. Hemberg, S. Bloom, W. Chao, E.H. Anderson, D.T. Attwood, Y. Lu, and B. Parkinson, "Nanometer-scale ablation with a table-top soft x-ray laser," Opt. Lett. **31**, 3615 (2006).

[10] M. Dubov, I. Bennion, D.N. Nikogosyan, P. Bolger, and A. V Zayats, "Point-by-point inscription of 250 nm period structure in bulk fused silica by tightly focused femtosecond UV pulses," J. Opt. A **10**, 025305 (2008).

[11] Y. Wu, E. Cunningham, H. Zang, J. Li, M. Chini, X. Wang, Y. Wang, K. Zhao, and Z. Chang, "Generation of high-flux attosecond extreme ultraviolet continuum with a 10 TW laser," Appl. Phys. Lett. **102**, 201104 (2013).

[12] X. Yu, Q. Bian, Z. Chang, P.B. Corkum, and S. Lei, "Femtosecond laser nanomachining initiated by ultraviolet multiphoton ionization," Opt. Express **21**, 24185 (2013).

[13] X. Yu, Q. Bian, B. Zhao, Z. Chang, P.B. Corkum, and S. Lei, "Near-infrared femtosecond laser machining initiated by ultraviolet multiphoton ionization," Appl. Phys. Lett. **102**, 101111 (2013).

[14] D. Grojo, M. Gertsvolf, S. Lei, T. Barillot, D. M. Rayner, and P. B. Corkum, "Exciton-seeded multiphoton ionization in bulk SiO_2," Phys. Rev. B **81**, 212301 (2010).

[15] T.Q. Jia, H.X. Chen, M. Huang, F.L. Zhao, X.X. Li, S.Z. Xu, H.Y. Sun, D.H. Feng, C.B. Li, X.F. Wang, R.X. Li, Z.Z. Xu, X.K. He, and H. Kuroda, "Ultraviolet-infrared femtosecond laser-induced damage in fused silica and CaF_2 crystals," Phys. Rev. B **73**, 054105 (2006).

[16] R.M. Herman and T.A. Wiggins, "Production and uses of diffractionless beams," J. Opt. Soc. Am. A **8**, 932 (1991).

[17] I.H. Chowdhury, X. Xu, and A.M. Weiner, “Ultrafast two-color ablation of fused silica,” Appl. Phys. A **83**, 49 (2006).

[18] S. Zoppel, R. Merz, J. Zehetner, and G.A. Reider, “Enhancement of laser ablation yield by two color excitation,” Appl. Phys. A **81**, 847 (2005).

Chapter 7 - Three-Dimensional Modification in Silicon with Infrared Nanosecond Laser

This work was published in "Three-dimensional modification in silicon with infrared nanosecond laser," X. Yu, C. A. Trallero-Herrero, D. Grojo, and S. Lei, Proceedings of the ASME 2016 International Manufacturing Science and Engineering Conference (MSEC2016).

Abstract

Motivated by previous work on three-dimensional (3D) fabrication inside dielectrics, we report experimental results of 3D modification inside intrinsic silicon wafers using laser pulses with 1.55 μm wavelength and 3.5 ns pulse duration. Permanent modification in the form of lines is generated inside silicon by tightly focusing and continuously scanning the laser beam inside samples, without introducing surface damage. Cross sections of these lines are observed after cleaving the samples, and are further analyzed after mechanical polishing followed by chemical etching. With the objective lens corrected for spherical aberration, tight focusing inside silicon is achieved and the optimal focal depth is identified. The laser-induced modification has a triangular shape and appears only in regions before the geometrical focus, suggesting significant absorption in those regions and resulting in reduced energy density. The morphology of modified regions is found to be dependent on the laser polarization.

1. Introduction

The ability to directly generate three-dimensional (3D) structures inside materials distinguishes laser-based materials processing from other planar lithographic methods, and has been extensively studied for large-bandgap materials [1]. Potential applications with this 3D technique include the fabrication of optical waveguides [2], microfluidic network [3,4], electronic

circuits [5], etc., and the integration of these components to realize lab-on-a-chip [6]. Fabrication in 3D is realized by concentrating large amount of laser energy within a small volume inside materials, and is usually initiated through nonlinear processes such as multiphoton and avalanche ionization [7,8]. Due to their large bandgaps, dielectric materials can be processed with laser wavelengths as short as in the ultraviolet range [9]. Formation of voids [10] and nano-channels [11] inside dielectrics has been reported.

Semiconductors (such as silicon) form the basis of modern electronics. Current manufacturing processes, notably photolithography, are inherently planar methods, and 3D structures are achieved in a layer-by-layer fashion, which involves multiple steps and therefore increases defect rate and reduces yield. Laser-based 3D fabrication provides a one-step manufacturing solution and has the potential to reduce processing time and cost. The reader can refer to Ref. [12] for a short review on internal modification of silicon. Recent advances include internal modification for wafer dicing [12], double-femtosecond-laser-pulse induced modification [13], machining on the back surface of silicon [14], and attempt to fabricate micro-channels inside silicon [15].

A wealth of knowledge about internal modification inside dielectrics has been gained in recent years, and would be invaluable for applying this technique to other materials. However, 3D processing of semiconductors is a relatively new topic, and some critical issues related specifically to it need to be addressed. First, due to the large difference of refractive indices between air (n=1) and silicon (n=3.5), more severe spherical aberration (SA) is expected for focusing in silicon than in glass (n~1.5), especially with high numerical aperture (NA) optics. SA should be corrected in order to achieve diffraction-limited focusing. Second, direct observation of internal structures inside semiconductors requires infrared optical microscopy, which is less commonly-used than its

visible-light counterpart and typically has lower resolution due to the use of longer-wavelength light. A commonly-used destructive analysis method is cleaving samples and then observing cross sections with visible-light or scanning electron microscopy. For this method to be accurate, it is necessary to distinguish between modification/damage induced solely by the laser and that introduced by the cleaving procedure, as has been pointed out by others [12]. Third, the order of multiphoton ionization (m) for dielectrics and near-infrared lasers is usually large (m=6 for fused silica and 800 nm laser wavelength), and therefore absorption can be confined in a small volume around the geometrical focus. For silicon (with a bandgap of 1.1 eV) and lasers with wavelengths in the telecommunication range (around 1.5 μm, photon energy 0.8 eV), m is only 2, resulting in weaker confinement and larger absorption volume. It is therefore necessary to investigate the maximum energy density achieved at the focus, a key parameter determining whether or not significant damage can be generated [10].

In this paper, we attempt to address these issues by investigating the formation of modification inside intrinsic silicon wafers using a fiber laser with 1.55 μm wavelength and 3.5 ns pulse duration. By tightly focusing the laser beam with SA correction, we write continuous lines inside the samples and analyze their cross sections. The absorption is found to occur before the laser beam reaches its geometrical focus, resulting in energy density orders-of-magnitude lower than that required to initiate significant damage. The morphology of modified region is found to be dependent on the polarization of the writing beam, similar to nano-gratings formed in transparent materials after femtosecond laser irradiation. This work expands the on-going research on 3D fabrication of dielectrics to semiconductors, with the objective aimed at realizing direct 3D processing of semiconductors using optimally-designed laser beams.

2. Experimental details

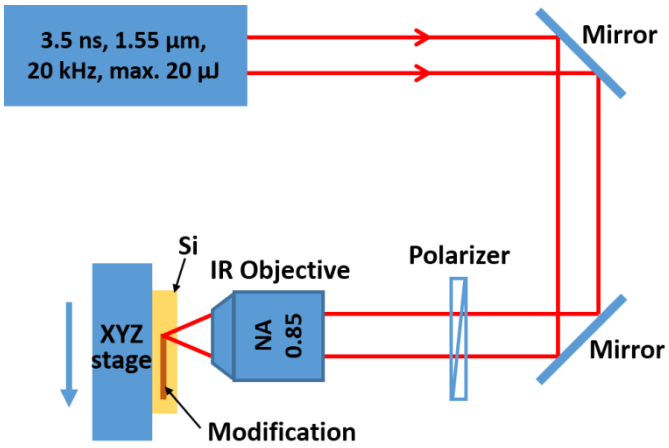

Figure 7.1 Experimental setup.

The experimental setup is sketched in Figure 7.1. The laser is a fiber MOPA (master oscillator power amplifier) laser (MWTechnologies, Model PFL-1550) delivering laser pulses at 1.55 µm center wavelength and 3.5 ns FWHM (full-width-at-half-maximum) pulse duration. The repetition rate is tunable from 20 to 150 kHz, and is fixed at 20 kHz in this study. The maximum pulse energy is 20 µJ. The output beam is collimated and has a $1/e^2$ diameter of 6 mm. Two metallic mirrors are used to route the beam. It should be noted that the polarization of the output beam is not determined by the manufacturer. The power measured at the laser output shows an angular dependence similar to that for an elliptical polarization. A Glan-Taylor polarizer is used in the latter part of this study (Figure 7.8) to allow only one polarization to pass through. The beam is focused by a 0.85 NA infrared objective lens (Olympus, Model LCPLN100XIR), which has SA correction for silicon thickness of 0-1 mm. The input aperture size of the objective is 3.5 mm, resulting in ~50% energy loss due to clipping. The estimated focal spot diameter and confocal length inside silicon are 1.5 µm and 8 µm, respectively (shown below). The samples are (100)-orientated, 4 inch in diameter, 1 mm thick, intrinsic silicon wafers with front and back

surfaces polished (Sil'tronix Silicon Technologies). The resistivity is >200 Ω·cm, ensuring negligible linear absorption for 1.55 μm light [16]. The wafers are cleaved into small pieces of about 20×20 mm^2, which are mounted on a motorized XYZ stage (Newport, Model ILS100PP). The focal depth is controlled by moving the sample along the laser beam's axial direction, and modification is induced by scanning the sample transversely at a constant speed of 1 mm/s. The focus overlapping is > 97% at this speed. To ensure that the focal depth is constant during scanning, the orientation of the sample is carefully adjusted so that within the area of interest (typically 5×5 mm^2), the difference in focal depth is < 50 μm. The focus on the front surface is determined when white light (plasma) from surface damage is observed, and the desired depth (d) is reached by moving the sample towards the objective by d/n, where n=3.5 is the refractive index of silicon at 1.55 μm. The sample after laser writing is cleaved perpendicularly to the scanning direction and the cross sections (in the (110)-plane) are observed with a visible-light microscope. The cleaved surface is then gently polished and examined with the microscope again (no modification is observed, shown below). The polished surface is etched in a 50% wt KOH solution for 5 minutes (in an ultrasonic bath) to reveal the modified regions and observed with the microscope. In this study, damage is not observed on either front or back surface of the silicon samples. In this study, the term "modification" refers to any permanent change in the sample after laser treatment, and "damage" refers to significant modification, such as cracks and voids.

3. Results and discussion

3.1 Optimal focal depth with spherical aberration (SA) correction

Due to the large difference of refractive indices between air and silicon, spherical aberration is expected to be significant and needs to be compensated. The objective lens used in this study has a correction collar and can compensate aberration in silicon with thickness up to 1

mm, which is also the thickness of our samples. To facilitate later characterization of induced modification, we choose to generate modification in the middle of the samples, and therefore the correction collar is set at 0.5 mm throughout the experiments. It should be noted that setting the correction at 0.5 mm does not guarantee optimal focusing at this depth (shown below), since the lens might be designed around a wavelength different from our laser wavelength. To get this optimal focusing depth, we write continuous lines at various depths with 50 µm increments, at a constant speed of 1 mm/s. The samples are then cleaved perpendicularly to the writing direction, and the cross sections are examined with a visible-light microscope. The results for three pulse energies are shown in Figure 7.2. The polarizer is not used in obtaining Figure 7.2. Regions in black color and aligned vertically are laser-induced modification, and the structures seen outside these regions are caused by the cleaving procedure. For a high pulse energy of 2.5 µJ, modification is observed within a wider depth range, from 350 to 550 µm. This range reduces for a lower energy of 1.5 µJ, and only two modification at 400 and 460 µm can be observed. No modification is seen when the pulse energy is reduced to 1 µJ.

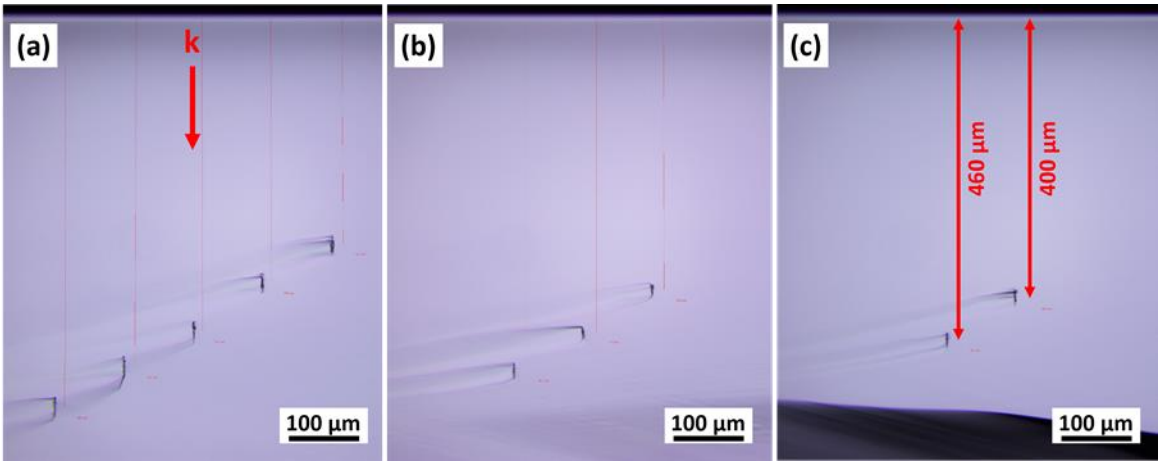

Figure 7.2 Cross sections of modification lines in silicon at various depths with pulse energy of (a) 2.5 µJ, (b) 2 µJ, and (c) 1.5 µJ. Regions in black color and aligned vertically are laser-induced modification. Narrow vertical lines in red color are depth measurements.

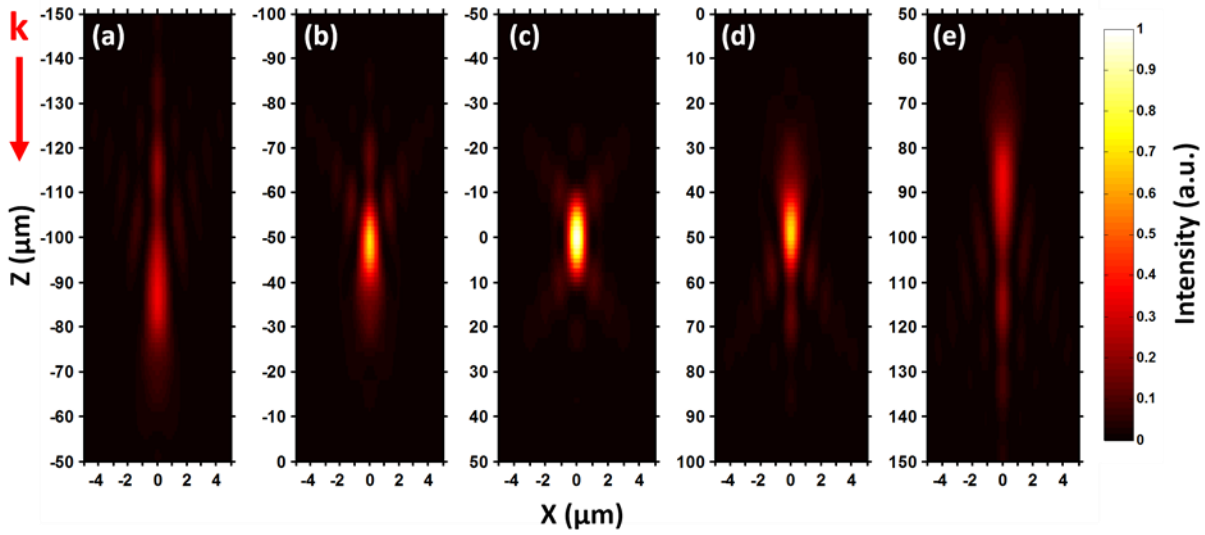

Figure 7.3 Calculated focal intensities at various depths inside silicon with the consideration of refractive index mismatch. Z=0 corresponds to a depth of 430 μm. The intended focal depths are Z=-100, -50, 0, 50 and 100 μm for (a)-(e), respectively. Intensities in all the images are normalized to the peak intensity in (c).

The results in Figure 7.2 can be easily understood by calculating the focal shape at various depths, with the consideration of refractive index mismatch. To show this, we use the PSF Lab software [17] to obtain focal intensity profiles. The objective lens is assumed to be perfectly corrected for 430 μm thick silicon, and intensities at various depths are calculated, as shown in Figure 7.3. We can see that at the depth corresponding to the correction depth (430 μm), the focus is a diffraction-limited spot with size consistent with estimation (Figure 7.3(c)). When the foci are shifted by about 50 μm ((b) and (d)), the foci are elongated and the peak intensities drop to about 70% of the peak intensity in (c). Further shifting the depth causes even longer foci and lower (35%) peak intensities. This shows that a shift in depth as small as 50 μm can cause reduction of peak intensities and as a consequence disappearance of laser-induced modification, in consistence with the experimental results shown in Figure 7.2. In the following experiments, the laser focus is positioned in the optimal depth range of 400 to 460 μm.

3.2 Observation of modification after polishing and KOH etching

Modification inside silicon can be observed nondestructively with infrared microscopy, which has been used by others [12–14]. In this study, we choose to observe the modification by cleaving the sample. This destructive method, however, induces undesired alteration to the samples (Figure 7.2) that might be indistinguishable from the modification caused solely by the laser. To avoid confusion, we apply the polishing-and-etching method that is commonly used in the study for dielectrics [18] and has also been used for silicon recently [14]. The sample from the previous experiment (Figure 7.2(b), also shown in Figure 7.4(a)) is mechanically polished and the polished surface is examined under a visible-light microscope. Interestingly, the modified regions completely disappear after polishing, as shown in Figure 7.4(b). A similar behavior is also reported for femtosecond laser writing [13]. We verify that modification caused by the highest pulse energy (20 μJ) and a much slower scanning speed (0.01 mm/s) also disappears after polishing (results not shown here). These findings suggest that the laser-induced modification in this study might merely be local change of density [13], not significant damage such as cracks and voids, because otherwise one would expect to see some type of irregularities on the polished surface. The change of density manifests itself after the disturbance during the sample cleaving procedure, and therefore modified regions can be observed in Figure 7.4(a).

To reveal the regions modified solely by the laser, the polished sample is etched by 50 wt.% KOH solution for 5 minutes. The etching is facilitated in an ultrasonic bath. The same surface after etching is shown in Figure 7.4(c), and the laser-modified regions reappear. Meanwhile, the alteration caused by cleaving is absent. The etching selectivity may arise from mechanisms similar to those in dielectrics [6].

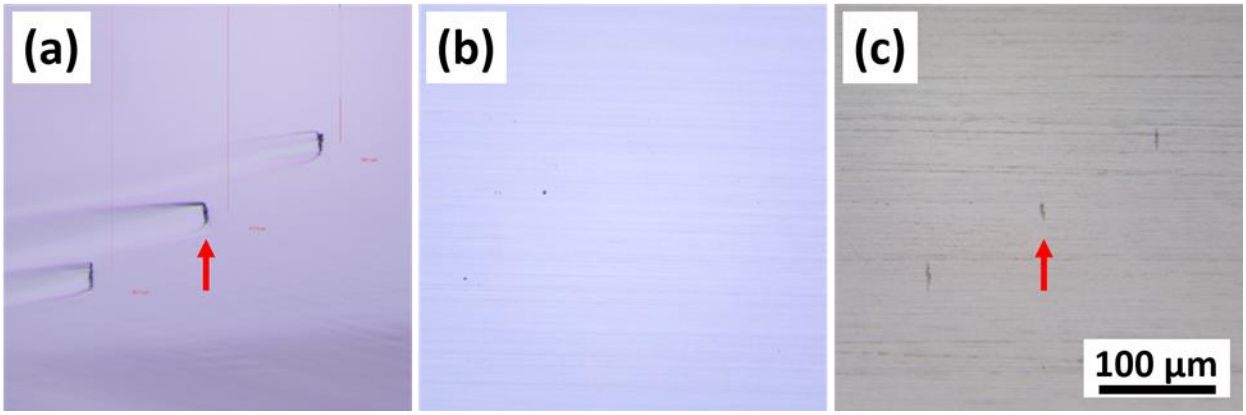

Figure 7.4 Cross sections of laser-modified regions after (a) cleaving, (b) polishing, and (c) chemical etching. Two cross sections pointed by arrows are magnified in Figure 7.5.

Two cross sections pointed by the arrows in Figure 7.4 are magnified and shown in Figure 7.5(a) and (b), and calculated focus profile is shown in Figure 7.5(c) for comparison. The absence of cleaving-induced alteration is clearly seen by comparing Figure 7.5(a) and (b). While the length of modification is similar to the simulation results, the width of modification is about 5 µm, more than three times of the calculated focus size (1.5 µm). If we assume that the modification is initiated by two-photon absorption, the estimated length and width of absorption region should be further reduced by a factor of 2 and $\sqrt{2}$, respectively. As will be shown below, the increased modification size is perhaps due to the fact that the absorption occurs before the laser beam reaches its focus. Another factor is electron diffusion, which expands the absorption volume. An estimation based on the diffusion coefficient shows that the diffusion length is about 3.6 µm (for 3.5 ns pulse duration) [19], comparable to the dimension of modified regions.

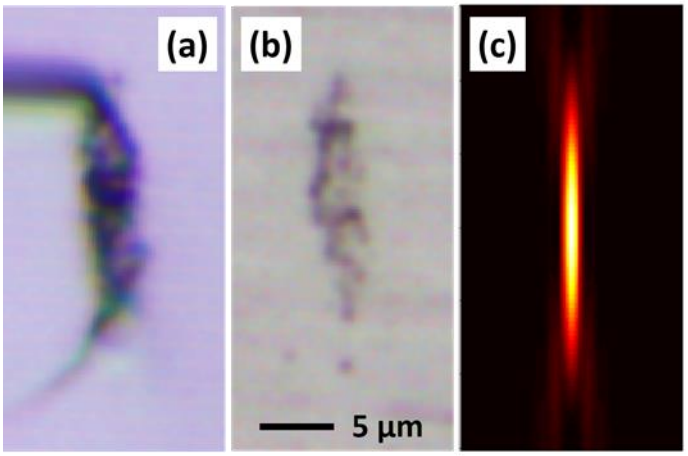

Figure 7.5 The cross sections pointed by arrows in Figure 7.4 are magnified and shown in (a) and (b). Calculated focal intensity (Figure 7.3(c)) is resized and shown in (c). All images have the same spatial scale.

3.3 Modification at the same depth and with increasing pulse energy

As mentioned above, absorption of 1.55 µm wavelength light in silicon is perhaps initiated by two-photon absorption, rather than the 6-photon process for 800 nm wavelength and fused silica. Therefore, the volume of absorbed energy is expected to be less confined than the latter case. The nature of absorption is further complicated by the small difference between the photon energy (0.8 eV) and the bandgap (1.1 eV), as it has been noted that the heating of silicon by the laser may cause the bandgap to shrink, leading to linear absorption [12]. It is therefore necessary to quantify the size and volume of absorption regions.

To this end, we focus the beam at a fixed depth of 400 µm and write lines with increasing pulse energy. The cross sections treated after the polishing-etching procedure are shown in Figure 7.6. The horizontal dashed line marks the intended focal depth of 400 µm. Although it is difficult to determine its exact depth, the focus should reside within or in the vicinity of the modification induced by the lowest pulse energy (2 µJ). The same focal depth is maintained throughout this sample with an accuracy better than 20 µm. Larger modified regions are seen with increasing pulse

energy, as would be expected. However, these regions enlarge asymmetrically, towards only the laser beam incoming direction. The modification from high pulse energies shows an inverse-triangle shape. These results suggest that the energy is absorbed in the regions before the geometric focus (on the plane marked by the dashed line), due to nonlinear and/or linear absorption. Since the maximum peak power delivered inside silicon is 2 kW, an order of magnitude below the critical power for self-focusing [12], collapse of the laser beam is not responsible for the increase of modification towards the laser beam.

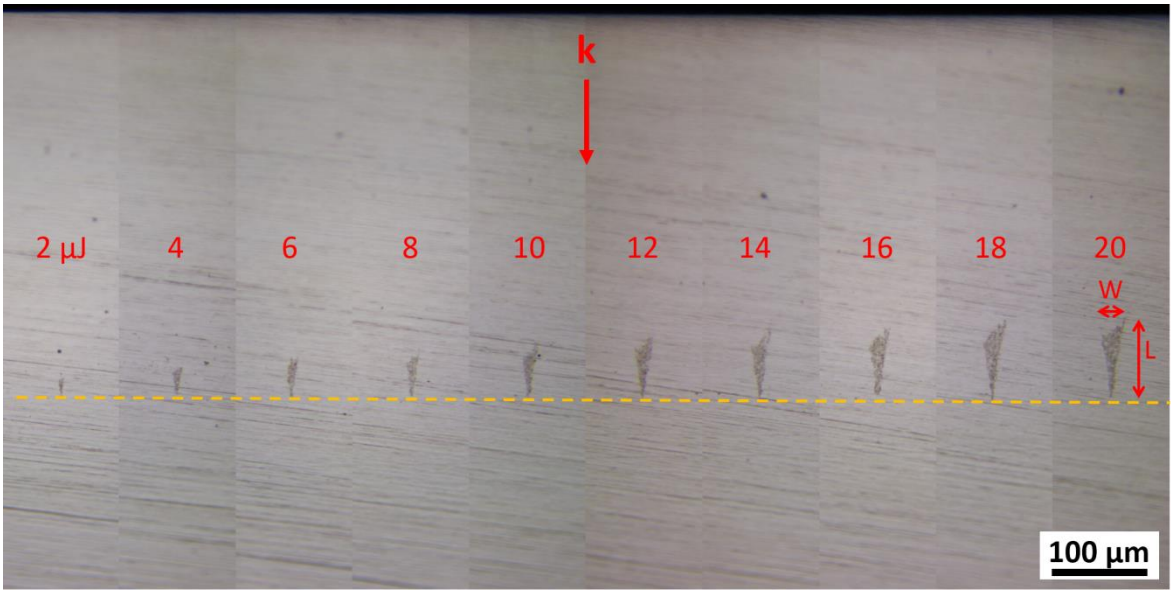

Figure 7.6 Laser-induced modification at the same depth (400 µm) and with increasing pulse energy. The horizontal dashed line marks the focusing depth. Polarizer is not used. Width (W) and length (L) of modified region are measured as depicted. Numbers above modified regions represent pulse energy in µJ.

The width (W) and length (L) of modified regions are measured and plotted in Figure 7.7 at various pulse energies. Modified volumes, $V = \pi(\frac{W}{2})^2 L/3$, are modelled as cones with base diameter W and height L, and energy density is calculated as $T_1 T_2 E/V$, where E is the pulse energy measured before the objective lens, T_1=50% is the transmission at the objective lens aperture, and T_2=69% is the transmission at the air-silicon interface. In this estimation, it is assumed that all the

laser energy delivered is absorbed within this volume. The estimated energy densities are also shown in Figure 7.7. We observe nearly linear increase of width and length with increasing pulse energy. However, the energy density drops significantly from 4.6 to 0.5 kJ/cm^3 as pulse energy increases, due to increased modification volume. The drop is more significant at lower energies, where the increase of size (ΔW and ΔL) is comparable to the values of W and L. The maximum energy density (4.6 kJ/cm^3) is orders-of-magnitude below the typical value (MJ/cm^3 in glass [10]) for significant damage (cracks and voids) to appear. It is obvious from Figure 7.7 that simply applying more pulse energy will not help increase energy density, because modified regions increase as well. For comparison, if all the input energy (20 μJ) could be confined in a cylindrical volume with 1.1 μm base radius (corresponding to the estimated focal radius) and 17 μm height (corresponding to the confocal length), the energy density would reach 100 kJ/cm^3 (with the consideration of energy loss), still lower than MJ/cm^3 but more significant modification could be generated at this value. It should be noted that in this study the beam overlapping is high (> 97%). The large modification size might also arise from the incubation effect, which causes a buildup of damage originating from initial, small damage sites [20].

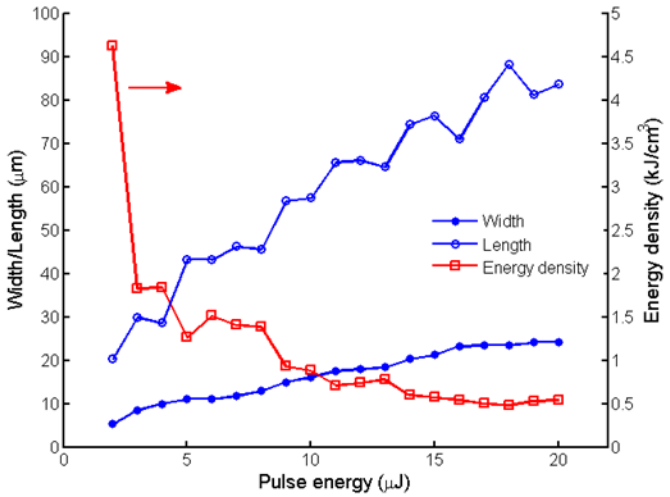

Figure 7.7 Width and length of modified regions measured from Figure 7.6, and estimated energy density at various pulse energies (measured before the objective lens). In estimating the energy density, energy loss due to the objective lens aperture and reflection from air-silicon interface has been taken into account.

Besides energy density, another important parameter in laser machining is peak intensity and fluence. Assuming that all the energy is focused into a diffraction-limited focal spot with radius of 1.1 μm, we estimate the highest intensity and fluence achieved with 20 μJ pulse energy are 112 GW/cm^2 and 387 J/cm^2, respectively. These values are very high, especially for the fluence. However, as shown in Figure 7.6, the absorption occurs in regions much larger than the geometrical focus. A useful measure is the intensity (fluence) at which nonlinear absorption starts (at a distance L before the geometrical focus). This can be calculated as $T_1T_2E/[\tau\pi(\frac{W}{2})^2]$ ($T_1T_2E/[\pi(\frac{W}{2})^2]$ for fluence), where τ = 3.5 ns is the pulse duration. The highest values are 0.9 GW/cm^2 and 3.1 J/cm^2 for intensity and fluence, respectively, and similarly to energy density, the highest values are achieved at the lowest pulse energy (2 μJ), due to smaller width (W). The intensity is significantly lower than that required for multiphoton absorption in dielectrics (>

TW/cm^2) for femtosecond lasers, and also lowered than the recently reported threshold for silicon (10 GW/cm^2) [21].

3.4 Effect of laser polarization

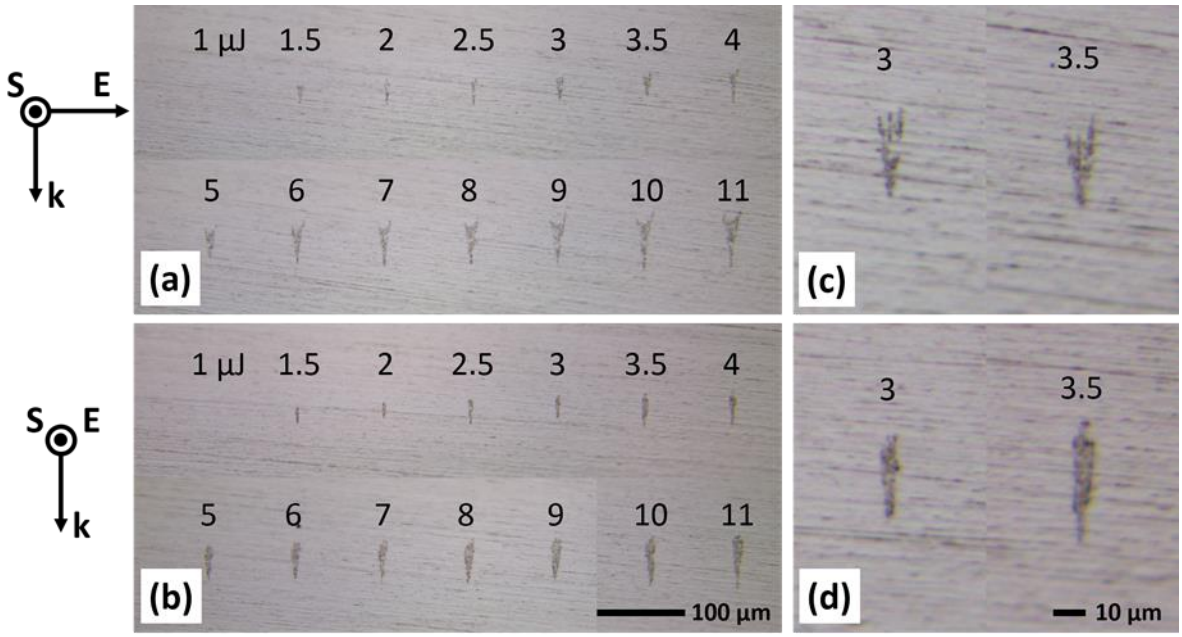

Figure 7.8 Cross sections of modified regions by two polarizations. Laser beam (k-vector) is from top to bottom. E is electric field, and S is scanning direction. (c) and (d) are magnified images for 3 and 3.5 µJ pulse energy in (a) and (b), respectively. Numbers above modified regions represent pulse energy in µJ.

The internal modification reported so far is generated without using the polarizer. Polarization-dependent modification is extensively studied in dielectrics [18,22] and has promising applications in, e.g., nano-fluidics [11]. In this section we investigate the effect of laser polarization on the morphology of modified regions. The polarizer is placed in the beam path to allow only one polarization state to pass through. The polarization direction (E) is chosen to be either perpendicular or parallel to the laser scanning direction (S), as depicted on the left in Figure 7.8. The maximum pulse energy after the polarizer is about one half of the value without using it, since only one polarization is selected. Lines of modification are written with these two

polarizations, and their cross sections (after etching) are shown in Figure 7.8. In Figure 7.8(a) and (c), the electric field (E) is perpendicular to the scanning direction (S), and in (b) and (d) is parallel to S. Other parameters (focusing depth, pulse energy, scanning speed, etc.) are kept the same. We observe different morphologies from these two polarizations. For E⊥S (Figure 7.8(a)), at high energies (>5 μJ), sharp structures can be seen extruding from the top part of modified regions, and at low energies (Figure 7.8(c)), distinct line-shaped structures are observed within the regions. These lines are most apparent at low energies. For E∥S, modified regions show smooth contours without any distinct line-structures. Although the mechanism responsible for these different morphologies is not clear yet, this observation resembles the formation of nano-gratings inside transparent materials from femtosecond laser irradiation [18,22]. However, the distance between these distinct lines (as large as several micrometers) is much larger than the period of nano-gratings (typically a fraction of laser wavelength).

4. Conclusion

In conclusion, we use a fiber laser with 1.55 μm wavelength and 3.5 ns pulse duration to generate permanent modification inside intrinsic silicon wafers. Spherical aberration is found to be important and needs to be corrected for tight focusing at desired depth. While laser-induced modification can be clearly observed after cleaving the samples and exposing the cross sections, this modification disappears after mechanical polishing, suggesting the absence of severe damage such as cracks and voids. Increasing pulse energy causes the modified region to expand asymmetrically towards the incoming beam, and therefore reduces energy density deposit near the focal volume. The morphology of modification is found to be dependent on the polarization direction. Distinct line-shaped structures, resembling those in dielectrics after femtosecond laser irradiation, are observed. While we are not able to generate cracks or voids in this study, these

results could be helpful for future work to achieve direct laser fabrication in the bulk of semiconductors.

References

[1] Gattass, R., and Mazur, E., "Femtosecond laser micromachining in transparent materials," Nat. Photonics **2**, 219 (2008).

[2] Davis, K. M., Miura, K., Sugimoto, N., and Hirao, K., "Writing waveguides in glass with a femtosecond laser," Opt. Lett. **21**, 1729 (1996).

[3] Sugioka, K., Hanada, Y., and Midorikawa, K., "Three-dimensional femtosecond laser micromachining of photosensitive glass for biomicrochips," Laser Photon. Rev. **4**, 386 (2010).

[4] Liao, Y., Song, J., Li, E., Luo, Y., Shen, Y., Chen, D., Cheng, Y., Xu, Z., Sugioka, K., and Midorikawa, K., "Rapid prototyping of three-dimensional microfluidic mixers in glass by femtosecond laser direct writing.," Lab Chip **12**, 746 (2012).

[5] Xu, J., Liao, Y., Zeng, H., Zhou, Z., Sun, H., Song, J., Wang, X., Cheng, Y., Xu, Z., Sugioka, K., and Midorikawa, K., "Selective metallization on insulator surfaces with femtosecond laser pulses," Opt. Express **15**, 12743 (2007).

[6] Osellame, R., Hoekstra, H. J. W. M., Cerullo, G., and Pollnau, M., 2011, "Femtosecond laser microstructuring: an enabling tool for optofluidic lab-on-chips," Laser Photon. Rev. **5**, 442 (2011).

[7] Gamaly, E. G., and Rode, A. V, "Physics of ultra-short laser interaction with matter: From phonon excitation to ultimate transformations," Prog. Quantum Electron. **37**, 215 (2013).

[8] Balling, P., and Schou, J., "Femtosecond-laser ablation dynamics of dielectrics: basics and applications for thin films," Reports Prog. Phys. **76**, 036502 (2013).

[9] Yu, X., Bian, Q., Zhao, B., Chang, Z., Corkum, P. B., and Lei, S., "Near-infrared femtosecond laser machining initiated by ultraviolet multiphoton ionization," Appl. Phys. Lett. **102**, 101111 (2013).

[10] Gamaly, E. G., Juodkazis, S., Nishimura, K., Misawa, H., and Luther Davies, B., "Laser-matter interaction in the bulk of a transparent solid: Confined microexplosion and void formation," Phys. Rev. B **73**, 214101 (2006).

[11] Liao, Y., Shen, Y., Qiao, L., Chen, D., Cheng, Y., Sugioka, K., and Midorikawa, K., "Femtosecond laser nanostructuring in porous glass with sub-50 nm feature sizes," Opt. Lett. **38**, 187 (2013).

[12] Verburg, P. C., Römer, G. R. B. E., and Huis in 't Veld, A. J., "Two-photon–induced internal modification of silicon by erbium-doped fiber laser," Opt. Express **22**, 21958 (2014).

[13] Mori, M., Shimotsuma, Y., Sei, T., Sakakura, M., Miura, K., and Udono, H., "Tailoring thermoelectric properties of nanostructured crystal silicon fabricated by infrared femtosecond laser direct writing," Phys. Status Solidi **7**, 1 (2015).

[14] Ito, Y., Sakashita, H., Suzuki, R., Uewada, M., Luong, K. P., and Tanabe, R., "Modification and machining on back surface of a silicon substrate by femtosecond laser pulses at 1552 nm," J. Laser Micro Nanoeng., **9**, 98 (2014).

[15] Grojo, D., Mouskeftaras, A., Delaporte, P., and Lei, S., "Limitations to laser machining of silicon using femtosecond micro-Bessel beams in the infrared," J. Appl. Phys. **117**, 153105 (2015).

[16] Leyder, S., Grojo, D., Delaporte, P., Marine, W., Sentis, M., and Utéza, O., "Non-linear absorption of focused femtosecond laser pulses at 1.3μm inside silicon: Independence on doping concentration," Appl. Surf. Sci. **278**, 13 (2013).

[17] Nasse, M. J., and Woehl, J. C., 2010, "Realistic modeling of the illumination point spread function in confocal scanning optical microscopy," J. Opt. Soc. Am. A **27**, 295 (2010).

[18] Yu, X., Liao, Y., He, F., Zeng, B., Cheng, Y., Xu, Z., Sugioka, K., and Midorikawa, K., "Tuning etch selectivity of fused silica irradiated by femtosecond laser pulses by controlling polarization of the writing pulses," J. Appl. Phys. **109**, 053114 (2011).

[19] Mouskeftaras, A., Rode, A. V., Clady, R., Sentis, M., Utéza, O., and Grojo, D., "Self-limited underdense microplasmas in bulk silicon induced by ultrashort laser pulses," Appl. Phys. Lett. **105**, 191103 (2014).

[20] Mannion, P. T., Magee, J., Coyne, E., O'Connor, G. M., and Glynn, T. J., "The effect of damage accumulation behaviour on ablation thresholds and damage morphology in ultrafast laser micro-machining of common metals in air," Appl. Surf. Sci. **233**, 275 (2004).

[21] Grojo, D., Leyder, S., Delaporte, P., Marine, W., Sentis, M., and Utéza, O., "Long-wavelength multiphoton ionization inside band-gap solids," Phys. Rev. B **88**, 195135 (2013).

[22] Bhardwaj, V. R., Simova, E., Rajeev, P. P., Hnatovsky, C., Taylor, R. S., Rayner, D. M., and Corkum, P. B., "Optically Produced Arrays of Planar Nanostructures inside Fused Silica," Phys. Rev. Lett. **96**, 057404 (2006).

Chapter 8 - Summary and Outlook

This dissertation tries to answer the question about how to use lasers as a manufacturing tool more effectively. Spatial, temporal and spectral domain approaches are demonstrated to address important issues such as machining resolution, processing speed, and system robustness. It is shown that a better understanding of laser-matter interaction can lead to novel laser processing strategies.

To summarize the major achievements, this dissertation:

- Demonstrates the extension of focal range by nearly three orders of magnitude with the use of Bessel beam for micromachining of thin film solar cell, greatly improving laser processing tolerance to surface height variance and positioning error;
- Presents a method of generating superpositions of high-order Bessel beam with >50% energy efficiency, and shows that the 1+(-1) beam can greatly suppress collateral damage from the zero-order Bessel beam;
- Develops a double-color femtosecond laser machining approach, with which the control of multiphoton and avalanche ionization is realized, the nanomachining capability is demonstrated, and the required UV threshold pulse energy can be reduced to sub-nJ level;
- Explores the possibility of 3D laser processing in semiconductors with short-wavelength infrared laser, and addresses key issues such as spherical aberration compensation and examination methods.

Recommendations for future work:

- The potential of spatial beam shaping for material processing needs to be further explored. For instance, identifying the optimal beam shape for various types of processing (e.g., cutting, drilling, trepanning) would be highly rewarding.
- Having been extensively engaging with gaseous targets, attosecond science is currently expanding to the study of condensed matter. Revolutionary laser processing technology could be developed based on a better understanding of light-solid interaction on the attosecond to few-cycle time scale.
- Direct laser 3D processing is still challenging, for dielectrics and more so for semiconductors. Critical to this topic is how to concentrate large amount of energy in small volume. Spatial, temporal and spectral domain techniques could be combined to achieve this goal.

Laser processing has become an integral, and sometimes indispensable, part of manufacturing systems. Nonetheless, laser is a relatively new tool for manufacturing, and it suffices to say that we have explored only a fraction of what laser can offer. Taking advantage of the tremendous advancement in recent years in laser design and manufacturing, and the ever-expanding frontier of light-matter interaction, we expect to see that new laser-based manufacturing technologies emerge, and that laser might become a tool as essential to our lives as mechanical tools.

Appendix A - List of Publications

Journal Papers

1.* Xiaoming Yu, Carlos A. Trallero-Herrero, and Shuting Lei, "Materials processing with superposed Bessel beams", Applied Surface Science, 360, 833 (2016).

2. Kedong Zhang, Jianxin Deng, Rong Meng, Shuting Lei, and Xiaoming Yu, "Influence of laser substrate pretreatment on anti-adhesive wear properties of WC/Co-based TiAlN coatings against AISI 316 stainless steel", International Journal of Refractory Metals and Hard Materials, 57, 101 (2016).

3. Kedong Zhang, Jianxin Deng, Shuting Lei, and Xiaoming Yu, "Effect of micro/nano-textures and burnished MoS_2 addition on the tribological properties of PVD TiAlN coatings against AISI 316 stainless steel", Surface and Coatings Technology, 291, 382 (2016).

4.* Xiaoming Yu, Jianfeng Ma, and Shuting Lei, "Femtosecond laser scribing of Mo thin film on flexible substrate using axicon focused beam", Journal of Manufacturing Processes, 20, 349 (2015).

5.* Xiaoming Yu, Zenghu Chang, P. B. Corkum, and Shuting Lei, "Fabricating nanostructures on fused silica using femtosecond infrared pulses combined with subnanojoule ultraviolet pulses", Optics Letters, 39, 5638 (2014).

6. Xiaoxu Song, Xiaoming Yu, Meng Zhang, ZJ Pei, and Donghai Wang, "A physics based temperature model for ultrasonic vibration-assisted pelleting of cellulosic biomass", Ultrasonics, 54, 2042 (2014).

7.* Xiaoming Yu, Qiumei Bian, Zenghu Chang, P. B. Corkum, and Shuting Lei, "Femtosecond laser nanomachining initiated by ultraviolet multiphoton ionization", Optics Express, 21, 24185 (2013).

8.* Xiaoming Yu, Qiumei Bian, Baozhen Zhao, Zenghu Chang, P. B. Corkum, and Shuting Lei, "Near-infrared femtosecond laser machining initiated by ultraviolet multiphoton ionization", Applied Physics Letters, 102, 101111 (2013).

9. Qiumei Bian, Xiaoming Yu, Baozhen Zhao, Zenghu Chang, and Shuting Lei, "Femtosecond laser ablation of indium tin-oxide narrow grooves for thin film solar cells", Optics & Laser Technology, 45, 395 (2013).

10. Yunsong Lian, Jianxin Deng, Youqiang Xing, Shuting Lei, and Xiaoming Yu, "Periodic and uniform nanogratings formed on cemented carbide by femtosecond laser scanning", Applied Surface Science, 282, 518 (2013).

Conference Presentations

1.* Xiaoming Yu, Carlos A. Trallero-Herrero, David Grojo, and Shuting Lei, "Three-dimensional modification in silicon with infrared nanosecond laser", Proceedings of the ASME 2016 International Manufacturing Science and Engineering Conference (MSEC2016), 2016, Blacksburg, Virginia, United States.

2. Naveenkumar Shanmugam, Xiaoming Yu, Hazem Alkotami, Garrick Devin, and Shuting Lei, "Machining of transparent brittle material assisted by laser-induced seed cracks", Proceedings of the ASME 2016 International Manufacturing Science and Engineering Conference (MSEC2016), 2016, Blacksburg, Virginia, United States.

3. Shuting Lei, David Grojo, Jianfeng Ma, Xiaoming Yu, and Han Wu, "Femtosecond laser backside ablation of gold film on silicon substrate", Proceedings of the 44rd SME NAMRC Conference, 2016, Blacksburg, Virginia, United States.

4. Haiyang He, Yayue Pan, Jie Xu, and Xiaoming Yu, "Effect of surface texturing on separation force in projection stereolithography", 11th International Conference on Micro Manufacturing, 2016, Irvine, California, United States.

5. Xiaoming Yu, Jianfeng Ma, and Shuting Lei, "Femtosecond laser scribing of Mo thin film on flexible substrate using axicon focused beam", Proceedings of the 43rd SME NAMRC Conference, 2015, Charlotte, North Carolina, United States. Nominated for Best Paper Award.

6. Xiaoming Yu, Zenghu Chang, P. B. Corkum, and Shuting Lei, "Damage formation on fused silica illuminated with ultraviolet-infrared femtosecond pulse pairs", SPIE Optics + Optoelectronics, 2015, Prague, Czech Republic.

7. Xiaoming Yu, Qiumei Bian, Zenghu Chang, P. B. Corkum, and Shuting Lei, "Control of multiphoton and avalanche ionization using an ultraviolet-infrared pulse train in femtosecond laser micro-/nano-machining of fused silica", Proc. SPIE 8968, Laser-based Micro- and Nanoprocessing VIII, 89680G, PhotonicsWest, 2014, San Francisco, California, United States.

8. Qiumei Bian, Xiaoming Yu, Baozhen Zhao, Zenghu Chang, and Shuting Lei, "Femtosecond laser ablation of Al and Mo thin film on flexible substrate for fabrication of thin film solar cells", 30th International Congress on Applications of Lasers and Electro-Optics, ICALEO, 2011, Orlando, Florida, United States.

* Included in this dissertation.